Scientific and Technological Alliance for Guaranteeing the European Excellence in Concentrating Solar Thermal Energy

STAGE
TE
EERA

Project Deliverable 12.6:

Report on heliostat performance and on control system and calibration system performance

WP12 – Task 12.1.2, Task 12.1.3 and Task 12.1.4	Deliverable 12.6
Due date:	January/2017
Submitted	February/2017
Partner responsible	**Coordination** IK4-TEKNIKER & CENER **Chapter 1 & 2:** IK4-TEKNIKER, CENER, CyI, ENEA, UNAM, CIEMAT, CSIRO **Chapter 3:** CNRS **Chapter 4:** CNRS, IK4-TEKNIKER, CENER, ENEA **Chapter 5:** CRANFIELD UNIV
Person responsible	**Cristóbal Villasante, Amaia Mutuberria, Marcelino Sanchez**
MAIN Author(s):	**Cristóbal Villasante, David Olasolo, Michael Burisch, Mathieu Coquand, Carmine Cancro, Camilo A. Arancibia, Paul Kirby, Iñigo Les**
Document version:	**3**
Reviewed/supervised by:	**Cristóbal Villasante (IK4-TEKNIKER), Iñigo Les (CENER)**
Dissemination Level	**PU**

Table of contents

Executive Summary

The main objective of WP12 is to support the advance of the technology for next generation Concentrating Solar Power (CSP), especially in solar tower plants technology. With the objective defined, the work focuses in two systems with greatest need in the CSTP:

■ Development of low cost heliostat fields by reducing the cost using small heliostats (below 10m2) that could be manufactured, installed, and commissioned for less than 100€/m2 and ad-hoc control and fast calibration systems. Mainly addressed inside T12.1

■ Development of improved high concentration optical systems and enhanced receiver concepts in order to resolve current adverse effects and minimizing optical and thermal losses and costs. Mainly addressed inside T12.2

Deliverable 12.6 is concerned with the first objective (T12.1) and in particular, it summarizes the main achievements reached in subtask 12.1.2, subtask 12.1.3 and subtask 12.1.4 as a result of the RTD activities developed.

■ Regarding subtask 12.1.2: the objectives defined in the DOW have been clearly surpassed (the additional effort has been covered by the partners on their own). Three main achievements have been reached:
  - A Cost Analysis tool was developed finalising the work in T12.1.1 (D12.1).
  - A common procedure to test the heliostats was defined (see Chapter 1).
  - 5 heliostat designs have been developed and four of them have been tested (see Chapter 2) taking advantage of the facilities available at different partner's premises (see Section 1.3), exceeding the only 1 heliostat development proposed in the DOW.

During the T12.1.2 additional partners[1] (CyI, ENEA, UNAM, CSIRO, DLR) joined the original ones (IK4-TEKNIKER, CENER, CIEMAT, TORRESOL) while other partners with minimum PM allocations focused on other subtasks (CNRS, EVORA, CRAN). Each partner focuses his design on a different low-cost strategy, which leads to generate interesting knowledge and developments.

IK4-TEKNIKER+CENER heliostat is reducing tracking requirements and cost by developing an innovative calibration system based on Patent Number P201531419 (see Section 4.2). Moreover, this heliostat is based on low-cost cable drives with a high potential for cost reduction as well as a high accuracy as showed the tests performed at PSA-CIEMAT.

On the other hand, CyI works with CSIRO on the latter's heliostat design to make the

---

[1] CSIRO and DLR with a minimum PM allocation supported the group on different analysis and tasks while CyI, ENEA, UNAM were more deeply engaged by developing and/or testing their own designs.

heliostats more robust and suitable for coastal applications (for example when CSP+Desalination activities are required). Tracking error evaluation has been also performed and shared.

ENEA is working on a deep cost-analysis considering different sizes and different commercial components in order to define the cheapest heliostat design. Moreover ENEA is developing a new feedback sensor (see Subsection 4.2.3) for solar tower plants that should allow to reduce the accuracy required to the tracker and consequently its costsdown.

Finally, UNAM and DLR collaborated in the definition of the testing protocol and UNAM shared part of the testing results on their prototypes.

■ <u>Regarding subtask 12.1.3</u>: the manpower allocation was very limited and no equipment or software budget was included. Accordingly, the work has been focused on a theoretical analysis based on the State of the Art and the shared though, suggestions and advises provided by the partners involved in T12.1. Due to IP issues, limited contributions from the industrial partners could be got. This work has been performed by CRANFIELD UNIV. and summarized at Chapter 5. Emphasis has been put on wired and wireless systems and the consequences of either for costings, control systems, calibration, etc.

■ <u>Regarding subtask 12.1.4</u>: The work has been performed according to the schedule and scope. Main achievements reached:
  • Deep review of methods suitable for optical verification (report on 09/11/15) and for heliostat tracking control (report on 18/12/15).
  • Development and validation of new calibration methods that leaded to two new patents.
  • Development of a closed loop sensor that could avoid heliostat calibration.

CNRS has gathered all this information from the partners and state of the art and have summarized it in Chapter 3 (optical characterization) and Chapter 4 (heliostats calibration). Developments have been especially focused on this last field, leading to new patents and sensors.

The main progress concerning to these methods is detailed at Chapter 4 but more details can be found in the papers presented by IK4-TEKNIKER, CENER and CNRS in the last SOLARPACES conferences in 2015 and 2016. Detailed information on the patents content is still classified since the patents are not published jet (IK4-TEKNIKER/CENER "Calibration method for heliostats" and CNRS "Backward-gazing method").

ENEA's approach is different and aims to develop a sensor that enables for closed-loop control thus avoiding the need for heliostat calibration (see Subsection 4.2.3).

1 Heliostat prototype testing

Concentrating solar power uses mirrors or lenses to redirect large areas of sunlight onto a target, where it is converted into heat, which is then used for various purposes, such as electricity generation through a heat engine. The efficiency of the latter is broadly governed by Carnot efficiency, in other words the higher the temperature, the larger the efficiency. One technology for concentrating solar radiation is the heliostat, a device made of mirrors that tracks the apparent motion of the sun and redirects its radiation onto a fixed target.

The scope of this work is to develop a methodology for testing and evaluation of heliostat performance. The present work identifies and defines the main parameters that influence heliostat performance, followed by methodologies and desired accuracy of measurements.

The proposed tests focus on small sized heliostats according to the tasks.

1.1 Operation conditions

Heliostats are required to operate under various environmental conditions. Of these, wind loads are particularly important as they influence the overall cost of the heliostat by influencing the amount of material used in the heliostat support structure and heliostat foundation, as well as the optical characteristics of the heliostat, since wind can induce vibrations in the heliostat structure. The principles of evaluating wind loads on heliostats are outlined in a report by Peterka and Derickson [10].

The definition of operating wind loads (e.g. definition of wind speed at a particular height above ground) for various conditions are summarized in Table 1, adapted from [20] as per the needs of the present report, and indicative mean wind speeds are given for each condition. Note that the gust speed may be evaluated according to ground morphology and interval of interest as in the guidelines of the [19].

Table 1 Wind load conditions for heliostat structural design

Wind Level	Condition	Wind Speed at 10m
W1.1	Fully operational performance requirements (beam accuracy 3 mrad)	5-8 m/s Mean
W1.2	Reduced accuracy operational requirements (beam accuracy 5 mrad)	10-14 m/s Mean
W2	Stowage limit (heliostat moving from an operating mode to either normal stow or high wind stop position)	10-22 m/s Mean
W3	Survival in any orientation	14-22 m/s Mean
W4	Survival in high-wind stop orientation	25-40 m/s Mean

The given range of wind speeds are intended as guidelines and not absolute design numbers. For instance speeds for conditions W3 and W4should be determined by local civil engineering codes, whereas conditions W1.1 and 1.2 relate to field balancing and annual energy production. Such considerations are discussed elsewhere in the literature [5][12][20].

Further, we note that defining an in situ test for heliostat wind loading is extremely difficult, due to the measuring accuracies and variability of wind (e.g. forces and direction).

1.2 Heliostat parameters & testing methodology

The following list of parameters for full characterization of heliostat prototypes has been identified. The parameters, along with their explanation and desired accuracy are listed. Methodologies for parameter evaluation are broadly outlined, with specific tests proposed in Section 1.4. Parameters are grouped into optical, mechanical, electrical and control system.

1.2.1 Optical

1.2.1.1 Facet Reflectivity

Reflectivity is defined as the fraction of incident electromagnetic radiation that is reflected at an interface between two materials with different refractive index. It is a directional property that is a function of incident direction, reflected direction and radiation wavelength. For solar energy applications, the spectrum of interest is in the wavelength range of 300-2500 nm [16].

The reflectivity is affected by the cleanliness of the facet, characterized by the soiling factor. The soiling factor is site-specific and depends on local weather conditions and heliostat cleaning cycles [3].

An extensive guideline for reflectivity measurements been published by SolarPACES [16], with findings from this report briefly summarized herein.

Prior to measurements, the mirror surface should be cleaned according to manufacturer specifications or with soft tissue and deionized water.

Measurements are performed as a function of wavelength in the range $280 < \lambda < 2500$ nm. Avoiding the UV region and starting the measurements at $\lambda = 300$ nm can significantly reduce equipment cost without impacting the final value of the average reflectivity.

The first objective is to measure hemispherical reflectance (ρh) over the whole relevant solar spectrum, typically done using an integrating sphere. This should be done as a function of incidence angle (θ), since incidence angles as large as 50° can be encountered in CSP applications. As a minimum requirement, hemispherical reflection should be measured at near normal conditions, e.g. $\theta < 15°$.

In CSP applications, only the energy reflected near the specular direction is useful for conversion, therefore reflectance as a function of specular angle (φ) must also be ascertained. As a minimum requirement, specular reflectance (ρs) should be measured at near normal incidence angles and for at least three specular angles in the range $0 < \varphi < 20$ mrad.

The solar-weighted reflectance (ρ_{sw}) is of interest, representing the convolution of the spectral reflectance function (either ρ_h or ρ_s) with the solar irradiance function $E(\lambda)$. The function $E(\lambda)$ is known discreetly and is tabulated in standard ASTM G173 for direct+circumsolar irradiance and for the appropriate Air Mass (AM = 1.5 for Europe and USA). The solar-weighted reflectance is calculated as

$$\rho_{sw} = \sum_{\iota=280}^{2500} \rho(\lambda_i)F(\lambda_i)$$

where $F(\lambda i)$ is a weighting factor, tabulated in the SolarPACES reference for intervals of $\Delta\lambda =$ 5 nm, or can be calculated as

$$F(\lambda) = \left. \frac{E_\lambda(\lambda_i)\Delta\lambda_\iota}{\sum_{\iota=0}^{2500} E_\lambda(\lambda_i)\Delta\lambda_\iota} \right.$$

Although the facet reflectivity provides a measure of the amount of energy a heliostat can redirect to the target, it is a parameter that is defined with the selection of the reflecting surface. For the purposes of the present report, the reflecting surface is considered an off-the-shelf item, and therefore experimentally measuring reflectivity will not be pursued in the heliostat testing discussed herein, rather the above discussion is included for completeness in discussing terms affecting heliostat performance.

1.2.1.2 *Facet Shape*

The facet optical quality encompasses imperfections on the reflector surface that cause the image to diverge from that predicted using ideal optics. It can be separated into surface slope error and surface roughness.

The reflecting surface slope error is a measure of the standard deviation of the slope of the real surface (e.g. real normal vector) from its ideal shape (e.g. ideal normal vector) [9]. It is typically measured in milliradians (mrad). The effect of slope error is a deviation of the angle of reflection as compared to that of the case of specular reflection.

The definition of the slope error is based on a comparison to the ideal mathematical shape of the surface. Facets are typically curved in a parabolic or spherical shape, with a given radius of curvature or focal length, to achieve further concentration. Therefore, we need to distinguish between the slope error calculated with respect to the ideal surface at design focal length, and that with respect to the ideal surface at the best-fit focal length.

Surface roughness error is the deviation in the direction of the normal vector of a real surface from its ideal form. It is typically measured in milliradians (mrad). The effect of roughness error is a broadening of the reflected image due to scattering.

The appropriate metrics for evaluation of the shape compliance relating to the slope and canting errors are the slope and focus deviation [7][9][17]. The local slope error is the angle between the real and ideal surface normal vectors at a given location, or

$$sd = acos\left(\frac{\vec{n}_{real} \cdot \vec{n}_{ideal}}{\|\vec{n}_{real}\| \|\vec{n}_{ideal}\|}\right)$$

To obtain a slope deviation error for the whole mirror, an area-weighted root mean square (RMS) value is evaluated as

$$SD = \sqrt{\sum\left(sd_i^2 \frac{a_i}{A_{tot}}\right)}$$

where a_i is the surface area representing the local slope error projected into the aperture plane and A_{tot} is the total aperture plane area [9][Meiser 2013].

Similarly, the focus deviation represents the deviation of the reflected light beam from the focal point. This may be evaluated from the slope deviation as

$$FD = 2\, d_m\, SD$$

where d_m is the focal distance, which is multiplied by two because of the reflection.

The above definitions have been generalized from definitions for parabolic trough mirrors. These definitions can be applied to perpendicular directions, resulting in x- and y-components of the slope and focus deviation, thus giving information on the astigmatic behavior of the mirrors.

The main methods for surface analysis typically used in solar applications rely either on direct measurement of the surface itself or on estimation of the surface through observation of the reflected image. These techniques are summarized below.

1.2.1.3   Direct surface measurement techniques

The photogrammetry technique has been applied to solar collectors in order to measure surface shape [11][14][15]. The technique employs information from digital images of an object taken from different positions. The object is market with retroreflective targets, which are used to accurately determine their relative position between the series of images. The accuracy of the technique has been estimated to be 0.5-1.0 mrad [8].

Optical profilometers, such as laser trackers, may also be used for solar reflector surface characterization. Such trackers have high accuracy, however measure only a single point at a time and are thus very time consuming. Some limitations, e.g. the use of prisms in contact with the surface to be measured, are surpassed by technological developments in the metrology field, with new devices – termed laser-radars – not requiring physical contact.

1.2.1.4   Imaging surface measurement techniques

The VSHOT a laser ray-tracing system designed to characterize optical surfaces for solar concentrators. A laser scans the surface in a predefined pattern and at each point the laser beam is reflected back to the target with its position recorded using a camera [2]. The surface

slope is calculated by knowing the laser output angle and the return spot. The accuracy of this technique was estimated at ±0.2 mrad [6].

Other techniques rely on reflections from continuous images, such as the deflectometry or fringe reflection techniques [1][17][18]. As such, these techniques have the added advantage of high resolution and higher accuracy. Although the principle of operation is similar to the VSHOT system, the whole reflector is imaged simultaneously so that each camera pixel imaging a specific location of the mirror can be mapped to the according location on the target.

1.2.1.5 Canting

Canting is the orientation of a mirror facet within an individual heliostat. The deviation of the facet normal to the ideal facet normal is the canting error. It is typically measured in milliradians (mrad).

1.2.2   Mechanical

1.2.2.1   Structure

As with any structure, the heliostat structure encounters a combination of several types of loads over its lifespan of being deployed in the field, such as wind loads, ice loads, loads from materials of construction, etc. Of these, perhaps the most important are the wind loads, and so the subsequent discussion will focus on these.

The heliostat structure must provide the necessary rigidity to precisely reflect solar radiation onto the target under various operating conditions, as defined in Section 1.1. A schematic of the various wind-induced loads is presented in Figure 1 [10]. The heliostat structure must be designed to successfully withstand the various loads it will encounter over the duration of its lifespan, while minimizing the construction materials so as to reduce the overall cost.
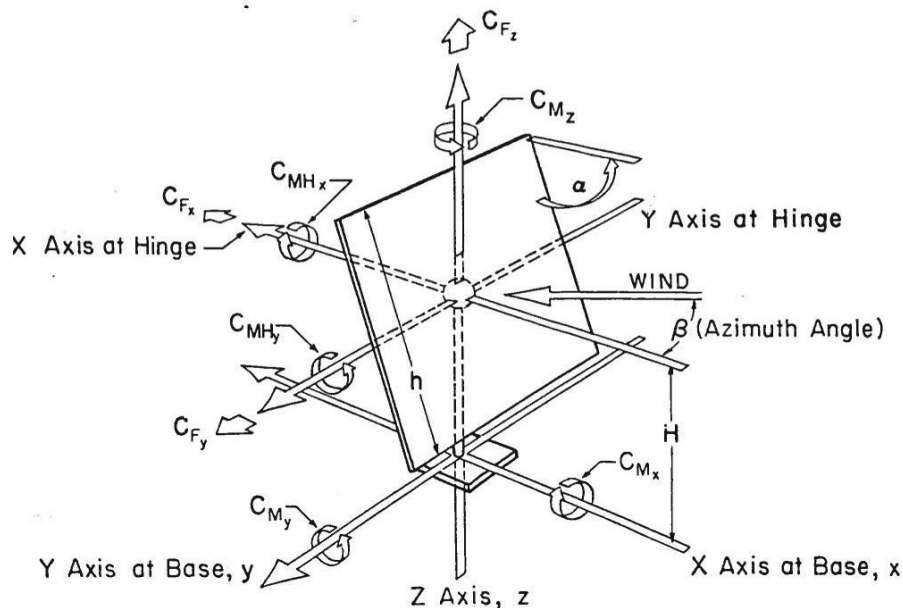

Figure 1. Wind induced structural loads on heliostat [10].

1.2.2.2 Reflector Durability

Optical durability of mirrors implies the maintenance of the reflectivity and specular reflection characteristics throughout the expected lifetime of the mirror in the outdoor environment [4]. Aging characteristics are encompassed herein.

Mechanical durability implies the resistance of the reflecting surface to corrosion induced by exposure to environmental conditions and resistance to mechanical stresses induced through gravitational, wind and other loads.

1.2.2.3 Drive System

The heliostat drives are sized to be able to move a given load. As the load on the heliostat varies due to varying wind intensity, a verification of the tracking ability of the heliostat under windy conditions must be performed. This involves verification of motors and actuators under the increased loading due to wind, verification of tracking precision, and verification of structural integrity. The ability of mechanical components within the drive system to withstand loads equal to their design load without failure should be verified.

1.2.3 Electrical consumption

The electrical power consumption of the heliostat should be characterized while the heliostat is tracking and while it is in standby. This is especially interesting for using autonomous power supplies and batteries.

The heliostat power consumption may be calculated by a power meter connected to the heliostat, as well as a data logger to record actuator positions.

1.2.4 Operation

1.2.4.1 Tracking Accuracy and Precision

Tracking error is defined as the standard deviation of a normal probability distribution describing the angular deviations of the central ray reflected from the heliostat surface with regards to an ideal aiming point direction. It is typically measured in milliradians (mrad).

The system tracking error should be measured accounting for operation under full load of normal operation, high-load of emergency operation and system backlash. The ability of the heliostat to track a given point in space independent of its starting position should be verified.

A methodology for analyzing intensity images from heliostat images is outlined below, following [13]. The methodology may be applied for determining the evolution of the image centroid as a function of time, however is more general and can be used to determine other statistics such as image radius (in primary and secondary direction), image ellipticity and ellipticity direction.

The heliostat image is characterized mathematically by its moments, evaluated as

$$M_{p,q} = \sum_x \sum_y x^p y^q f(x,y),$$

where f(x,y) gives the spatial distribution of intensity (or any other property of interest). The moments are used to evaluate the intensity-weighted center of the image as:

$$\bar{x} = \frac{M_{10}}{M_{00}} \text{ and } \bar{y} = \frac{M_{01}}{M_{00}}.$$

Given the information on center of mass, the central moments may be evaluated as

$$\mu_{p,q} = \sum_x \sum_y (x - \bar{x})^p (y - \bar{y})^q f(x,y).$$

Of particular interest are the 2nd order central moments μ_{20} and μ_{02}, as they can be used to define the image standard deviations in the x- and y- directions, respectively, as

$$\mu_x = \sqrt{\frac{\mu_{20}}{M_{00}}} \text{ and } \mu_y = \sqrt{\frac{\mu_{02}}{M_{00}}}.$$

Further, using the 1st order central moment μ_{11}, the covariance is defined as

$$covar(x,y) = \frac{M_{11}}{M_{00}}$$

which allows for the covariance matrix to be defined as

$$C(x,y) = \begin{bmatrix} \mu_x{}^2 & covar(x,y) \\ covar(x,y) & \mu_y{}^2 \end{bmatrix}.$$

From the covariance matrix, it's eigenvalues $\{\lambda_u, \lambda_v\}$ and eigenvectors $\{\mathbf{e}_u, \mathbf{e}_v\}$ may be directly computed.

Information about the image elongation is obtained from the ellipticity parameter, defined as

$$e = \sqrt{\frac{\lambda_u}{\lambda_v}}$$

as well as the direction of the ellipse (e.g. angle between target x-direction and ellipse u-direction), defined as

$$\alpha = \langle \vec{e}, \vec{x} \rangle$$

1.2.4.2 *Normal and Emergency Procedures*

The heliostat control must be able to perform certain routine operations, but also handle emergency procedures. A verification that the control system can handle certain orientations and emergency procedures [20] should be carried out.

- **Stow position** the position the heliostat moves in for overnight stow.
- **Maintenance position:** position of the heliostat during maintenance operations.

- **Cleaning position:** position of the heliostat for washing
- **Standby position:** the heliostat is tracking a designated point in space other than the target.
- **Tracking:** the heliostat is tracking the designated receiver aim point.
- **Beam characterization system:** the heliostat is periodically given instructions to track a secondary target for beam characterization purposes.
- **Initialization:** an initialization task executed automatically during heliostat startup.
- **Reset position:** a position of the heliostat for calibrating the relative position signals of the motor encoders.

Emergency procedures:

- **Local control to stow position:** if communications with the main control system are interrupted, the local controller must have the ability to move the heliostat to the stow position.
- **High wind stow:** in the event of high-winds the heliostats should move to a safe stow position, typically face-up or parallel to the ground.
- **Emergency defocus:** in the event of receiver overheating the heliostats must move away from the receiver aiming point.
- **Emergency stop:** in certain events it might be necessary for a heliostat to stop in place, e.g. to not track or return to stow position.

1.2.5 Mirror cleaning

For accurate evaluation of optical parameters relating to heliostats, (e.g. for tests in Sections 1.2.1.1, 1.2.4.1 etc.), the heliostat reflecting surfaces must be sufficiently clean. The objective, therefore, of this section is to give guidelines for cleaning procedures prior to heliostat testing.

The mirror's front surface should be cleaned carefully by rinsing with deionized water and soft lens tissue. If sufficient cleaning is not possible due to excessive soiling, then more aggressive scrubbing methods should be employed. Again, use of deionized water is recommended, whereas isopropanol is not advised as it sometimes results in smearing on mirror surface. If detergent is to be used, it should be biodegradable and diluted in deionized water, followed by rinsing with deionized water.

1.3 Testing facilities

In the present section, of summary of the testing facilities and capabilities of the various partners within the STAGE-STE consortium is outlined.

1.3.1   CENER

1.3.1.1   Optical Characterization Tests

Several aspects can influence the real concentrated flux distribution obtained by a heliostat with respect to the theoretical concentrated flux distribution that can be expected. The difference between the theoretical and the real sunspot obtained when focusing the sun towards a target determines the optical accuracy of the heliostat. The theoretical sunspot will be generated by CENER using a ray tracer.

In these tests, the sunspot generated by each of the facet in the heliostat, as well as the heliostat as a whole, will be analysed and evaluated. Additionally, as sunspot shapes vary during the day and different optical qualities could be obtained for different daytimes, the evolution of the optical accuracy during the day will also be analysed. An example of this analysis is given in Figure 2.
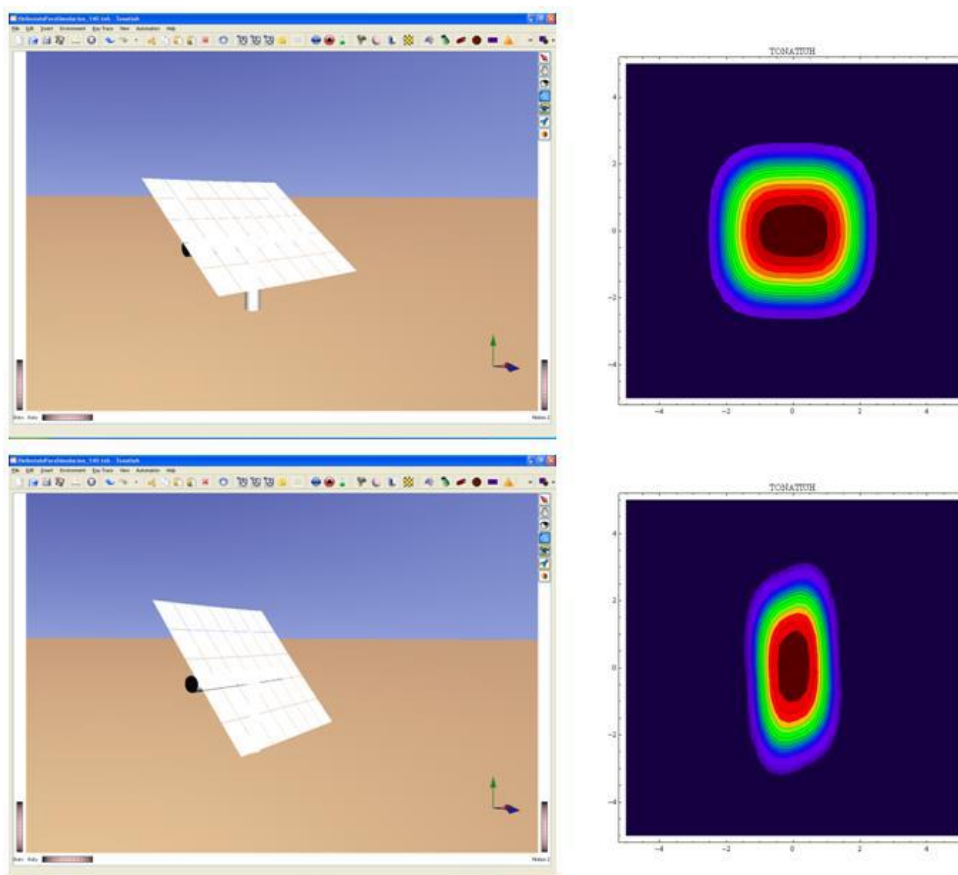

Figure 2. Simulation of the sunspot generated by a heliostat at two different positions (corresponding to different moments of the day or of the year).

Figure 3. Camera set for the characterization of a heliostat at Themis.

This system comprises the following equipment:

- Camera JAI AD-081 GE – 2 CCD High dynamic range (lenses 16 mm, f/1.4 and 12 mm, f/1.4).
- Open-source software Tonatiuh (Ray-Tracer).
- Camera IR FLIR (Model SC7000 Series, spectral range 3 - 5 µm or 8 - 12 µm / optional 1.5 - 5 µm)).Camera IR FLIR (SC655, spectral range 7.5–14 µm).

1.3.1.2 Geometry Characterization

The heliostats will be characterized in order to determine the real geometry of mirrors mirror shape accuracy, using the photogrammetry methodology. The technique uses a high resolution camera, some targets and a specialized post-processing specific software for the analysis of the data acquired. An image of a heliostat being analysed with the photogrammetry technique is shown in Figure 4.

The geometric characterization could be performed considering different positions of heliostats and wind conditions in order to infer the errors produced by the different loads: gravity and wind.

This system comprises the following equipment:

- Camera Canon EOS 5d Mark II (lenses Canon EF 24 mm , f/1.4L II USM and Canon EF 100-400 mm, f/4.5-5.6L IS USM).
- Software PhotoModeler 2015 (64 bit).

An alternative procedure to characterize solar concentrator's geometry is the use of night light. This type of characterization has several advantages respect to currently used methodologies:

- Taking measures during the night avoids plant production interruption.
- It allows direct visualization of the field from the focal point because the reflected light is much smaller than the reflected sun light.

Figure 4. Photogrammetry technique being performed in a heliostat.

It is possible to characterize more than one heliostat, or entire field, at the same time. CENER defined a methodology using a star (point light body) to determine the normal vectors of concentrator's surfaces with images of a number of start reflections sweeps. The technique uses a high resolution camera and a specialized post-processing software for the data acquired.

This system comprises the following equipment:

- Camera Canon EOS 5d Mark II (lenses Canon EF 24 mm , f/1.4L II USM and Canon EF 100-400 mm, f/4.5-5.6L IS USM).
- Specialized post-processing software.

1.3.1.3 Fringe Reflection Test

In collaboration with UNAM, CENER has developed a testing bench for shape characterization of heliostat facets using fringe reflection technique. This characterization technique consists in projecting in a screen sinusoidal fringe patterns and acquiring the images of the reflected images by the heliostat by a digital camera.

This system comprises the following equipment:

- Lambertian screen
- Video projector
- Camera Canon EOS 5d Mark II (lenses Canon EF 24 mm , f/1.4L II USM and Canon EF 100-400 mm, f/4.5-5.6L IS USM)

1.3.1.4 Tracking Accuracy

The tracking error, defined by the difference of the projection of the solar disk captured by the heliostat on a particular point on the target surface and the theoretical target point, will be measured in this test.

The evaluation of the tracking accuracy will be performed considering three criteria:

- Tracking accuracy at solar noon: the tracking accuracy of the heliostat will be evaluated at midday, when having the sun located at the Zenith.
- Tracking repeatability capacity: the tracking accuracy will be performed several times in order to guarantee a good level of repeatability and determine the systematic and non-systematic errors.
- Daily average heliostat tracking error: the tracking accuracy will be evaluated during the whole day, from sunrise to sunset, and an average tracking error will be calculated.

This system comprises the following equipment:

- Camera JAI AD-081 GE – 2 CCD High dynamic range (lenses 16 mm, f/1.4 and 12 mm, f/1.4).
- Digital inclinometer MITUTOYO (resolution ±0.01°)

1.3.2 CIEMAT

The methodology used by CIEMAT goes through the analysis of the sun images that the heliostat reflects and keeps during the day on the 12mx12m target placed in the CESA-1 tower (Figure 5).

| (a) | (b) |
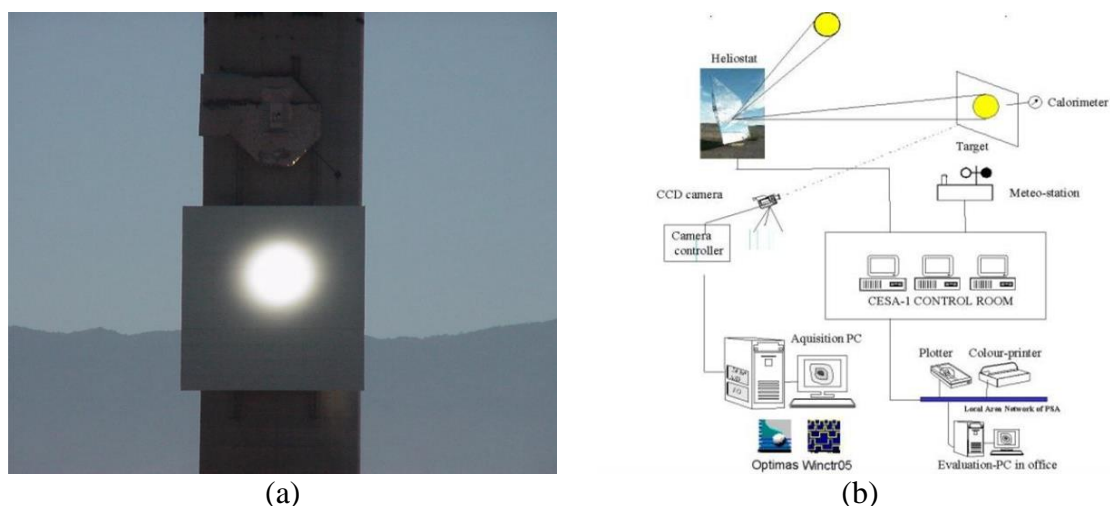
Figure 5. (a) White Lambertian target for picture analysis at PSA and (b) Heliostat measuring system block diagram.

For this purpose, PSA's Staff use the so called ProHERMES 2.A System [21] (Programmable HEliostat and Receiver MEasuring System), which block diagram can be seen in Figure X2. This system is formed by the following elements (Figure 6, Figure 7):

- FUJINON LENS. Model: H14X10.5A-R11. Zoom range: 10,5-147 mm.
- CCD camera: Hamamatsu Photonics. Model: ORCA-II C-4742-98 series.
- Filters: Omega Optical. Type: Neutral Density. Flat response range [400-700] nm.
- Picture acquisition and processing software: ImagePro Plus, 4.1, Media Cybernetics®.
- Solar tracker: Kipp & Zonen, model 2AP belt drive.
- White lambertian target coating: Amercoat 741. Area: 12mx12m.
- CESA-1 Heliostat Field meteo station.

Figure 6. ProHERMES 2 system.

Figure 7. CCD camera ORCA II.

The CCD device takes the sun pictures and its projection onto the target (Figure 8), also called real image.
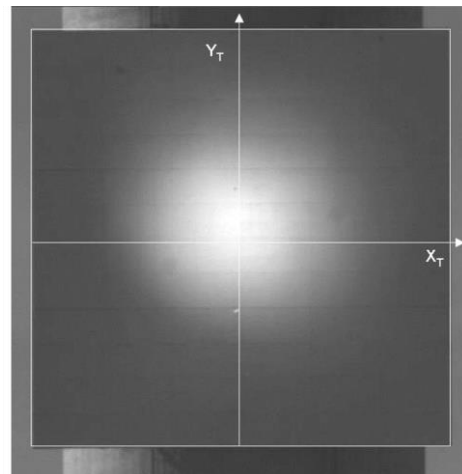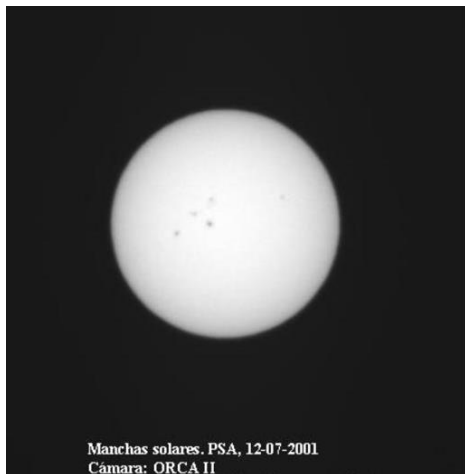
Figure 8. Original Sun Picture and its projection onto 12m x 12m target.

These pictures are subjected to a correction treatment of systematic errors inherent to the system, as well as a segmentation criteria to identify the regions of interest from the general context of the total camera field of view.

Figure 9 shows the picture of the solar shape captured by ProHERMES 2. A CCD camera (left) as well as its mathematical descriptors (right). It is afterward used as input signal to generate by Fiat_Lux [22] code the heliostat reflected image onto the target.
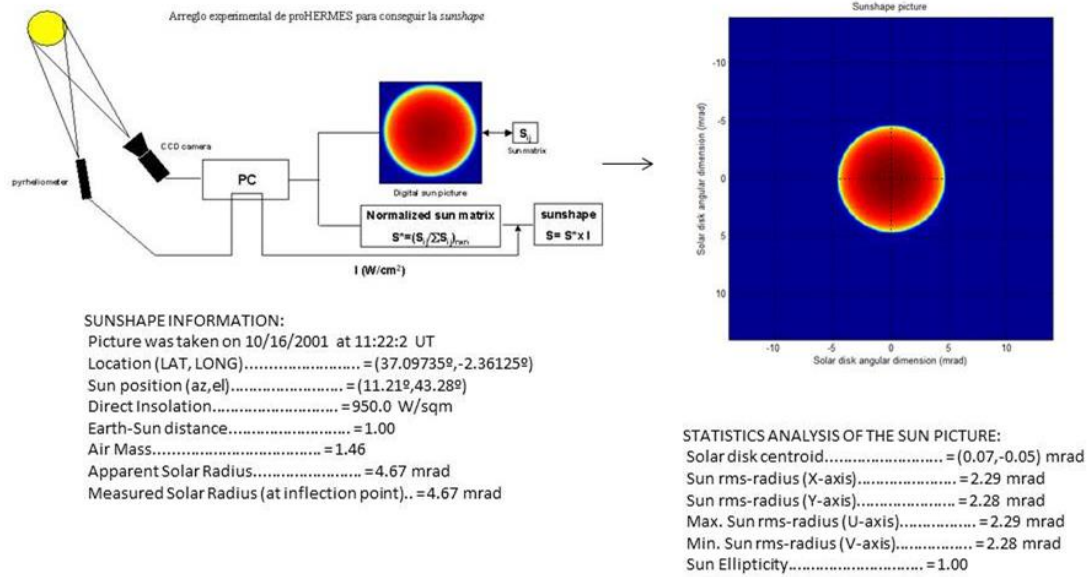
Figure 9. Sunshape information from ProHERMES 2.A System.

In the case of optical quality test, the grayscale digital image is studied as a whole, i.e., based on its statistical properties; on the other hand, the study of the aiming quality only requires the study of the real image maximum value (peak).

This equipment is complemented with two different procedures to measure optical quality of the reflecting surface:

- A Laser-scanner ScanStation P20 from Leica GeoSystems.
- A Photogrammetry procedure equipped with:
  - CANON EOS-5D MarkII camera equipped with one 20mm focal distance lens CANON EF 20mm f/2,8 USM.
  - PhotoModeler Scanner Ver. 2015.1 64bits® photogrammetry software.

1.3.3 CSIRO

1.3.3.1 *Mirror Geometry Characterization*

CSIRO employs a laser tracker to produce a set of points in three-dimensional space that lie on the surface of the glass. This system uses an accurate spherical ball with a corner reflector inside it which can be used with the laser tracker to precisely measure the position of the ball by using a two axis angle measurement to obtain angle and interferometry to obtain distance from the laser tracker. The ball is scanned across the mirror surface, with the laser scanner set to acquire approximately 400 points per square meter.

The point cloud acquired during scanning is interpolated using bicubic spline interpolation to obtain a uniform grid of points with 10 mm spacing, from which a triangular mesh surface is constructed.

The center of mass of the mirror normals is calculated and the normal of each facet is then compared to the ideal normal for the mirror at the design focal length at the facet centroid.

CSIRO has the capability to complete surface scanning at any location where the laser tracker can be setup.

The Leica AT901 laser tracker is used.

1.3.3.2 Image Characterization

Image assessment is performed on site for images up to 3×3 m square as long as the irradiance is higher than ambient light levels.

1.3.3.3 Actuator Characterization

CSIRO manufactures linear actuator control circuit boards and has established a testing procedure for these, including measurements of

- Communications efficiency.
- Current draw (operating and stall).
- Encoder performance.

Tests for linear actuator drives and encoders to predict lifetime and degradation rates are currently being designed.

Heliostat accelerated life tests are performed to determine actuator lifespan when operated at an accelerated rate.

1.3.4 CYI

The CyI uses a 2 x 2 m diffuse target onto which the heliostat image is projected. The target is constructed from 9 equal aluminum squares arranged in a 3x3 array, and painted white with a matte finish so as to increase the diffuse optical characteristics of the surface. Two types of data acquisition processes are planned: thermal and optical.

For the thermal tests, the back surface of the target is instrumented with thermocouples, from which statistics are gathered regarding the thermal centroid of the image and how this point moves during the day. Other information, such as the temperatures achieved on the target, are also recorded. A screenshot of the data acquisition and analysis software is given in Figure 10.
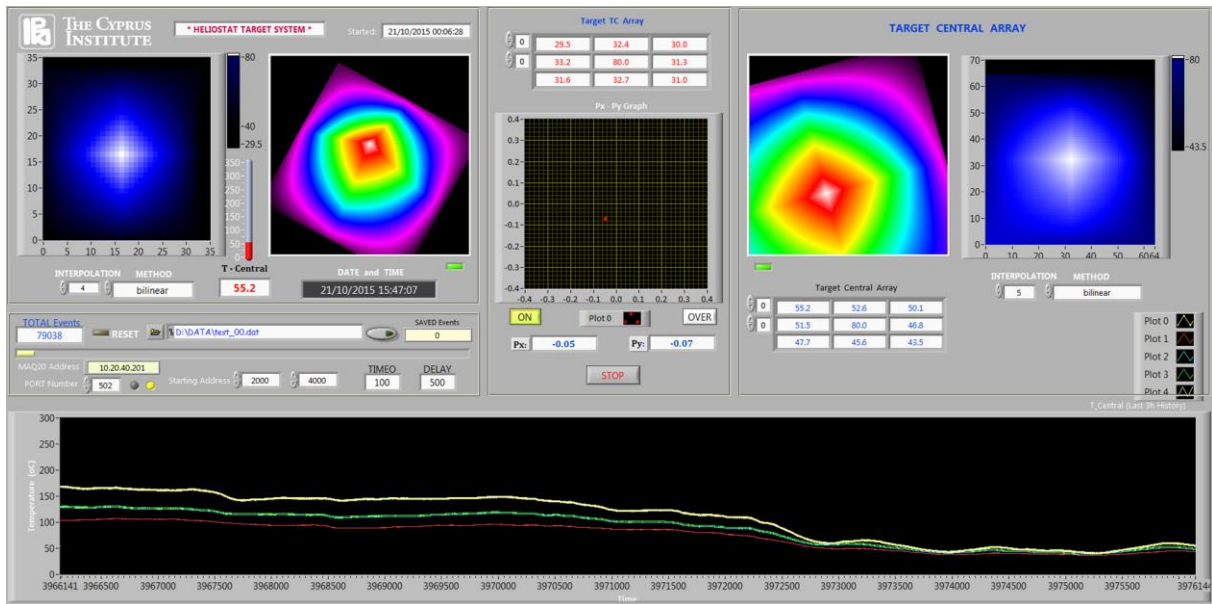
Figure 10. Thermal test software.

For optical tests, pictures of the heliostat image on the target are acquired at a predefined interval, allowing again for the image intensity centroid to be computed and evaluated throughout the day. The optical testing software of CyI is currently being developed.

The system comprises the following equipment

- Two CSIRO designed heliostats with aperture 2.25x2.25 m and focal length 35 m.
- Basler Scout SC1300-gm CCD camera.
- FUJIFILM HF50HA-1B 50 mm focal length lens.
- ND090 neutral density absorptive filter.

A correlation of the images obtained by the camera with those calculated via ray tracing (using Soltrace and Tonatiuh software) is performed to evaluate the deviation of the real image from the calculated one. The differences between the two are accounted for by the various optical errors of the physical mirror, and therefore the method is used to quantify optical errors.

1.3.5 ENEA

This paragraph regards the description of the procedure normally used by ENEA to test the trackers features. In principle we can say that the tracker accuracy depends on the interaction of different factors:

- Mechanical deformation of the structure due to its-own weight.
- Mechanical deformation of the structure due to wind load.
- Mechanical backlash of the actuators.
- Mounting errors.
- Inaccuracy of the electronic control system.

Under operating conditions, it is very complicated to understand the contribution of each of these factors. In particular, measurements on field of deformations due to the structure weight and to wind loads are very difficult and can be affected by not negligible errors. The only factor that can be measured with a good accuracy and consistency is the actuators backlash that depends on the used components.

For these reasons, our approach is to make an overall analysis in order to measure the heliostat total tracking error during a working period and to carry out some additional tests to measure the amount of the inaccuracy due to the actuators backlash.

1.3.5.1 *Measuring of overall tracking error*

ENEA designed and developed an optoelectronic device, shown in Figure 11, which is mounted parallel to the heliostat surface and measures the angular misalignment between the perpendicular to this surface and the incidence direction of the solar beam. It has been conceived for the trackers used for concentrating photovoltaic systems, where the module has to be pointed always orthogonally to the solar beam. However, supposing that heliostat features are independent from the tracking program, this apparatus can be used also to characterize the trackers working in reflection mode (normally used in the tower plants). In fact during the characterization tests they can be driven by software orientating the panel perpendicular to the sun.

The optoelectronic device is composed of the following components:

- A PSD (Position Sensitive Detector) sensor, which is based on lateral effect photodiode technology.
- A high temperature stability and low noise analog amplifier to fit the PSD output signal to the A/D input signal.
- A microcontroller equipped with an internal and additional external memory unit to save the data.
- A display showing the measured values.

Figure 11. The optoelectronic device sensor of ENEA.

The duolateral PSD, schematically shown in Figure 12, consists of N-type silicon substrate with two resistive layers separated by a PN junction: the front side has an ion-implanted P-type resistive layer with ohmic contacts on two sides; and the backside has an ion-implanted N-type resistive layer with two contacts at opposite ends placed orthogonally to the contacts

on the front side. Because the position signal is divided only into two parts, the duolateral PSD has the highest position detecting ability of all the sensor types.

The resistivity of the ion-implanted layers is extremely uniform, so the photocurrent for each electrode pair is inversely proportional to the distance between the incident spot of light and electrodes. The duolateral PSD generates photocurrents proportional to the position and intensity of the centroid of light on the active area.
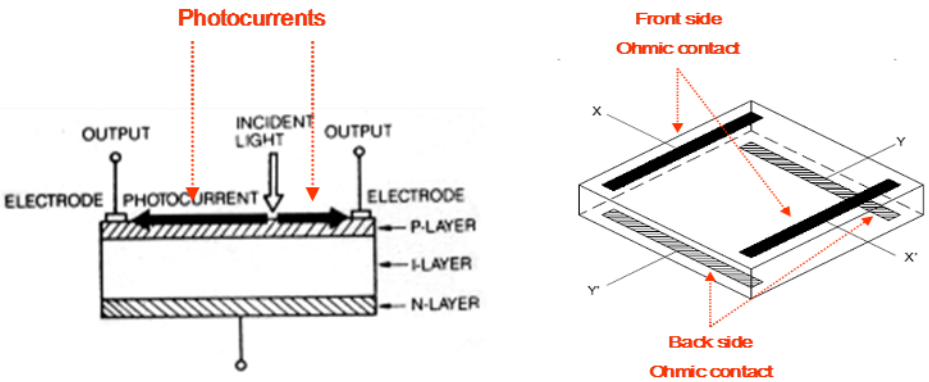
Figure 12. The duo-lateral PSD sensor.

The right position (zero misalignments) is reached when the solar beam hits the center of the PSD sensor (Figure 13 a); on the contrary the PSD sensor monitors a misalignment value proportional to the distance between its center and the solar beam incidence on the PSD (Figure 13 b).
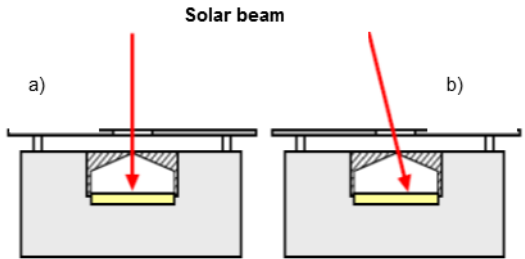
Figure 13. The OED working scheme.

An accurate calibration by means of indoor and outdoor tests has been carried out: it has been necessary to minimize the influence of the following factors: non-linearity of the PSD; structural tolerance of the OED; measurements errors. The main OED features are the following: sensitivity 0.001° and accuracy 0.75% of measured value (in clear sky conditions).
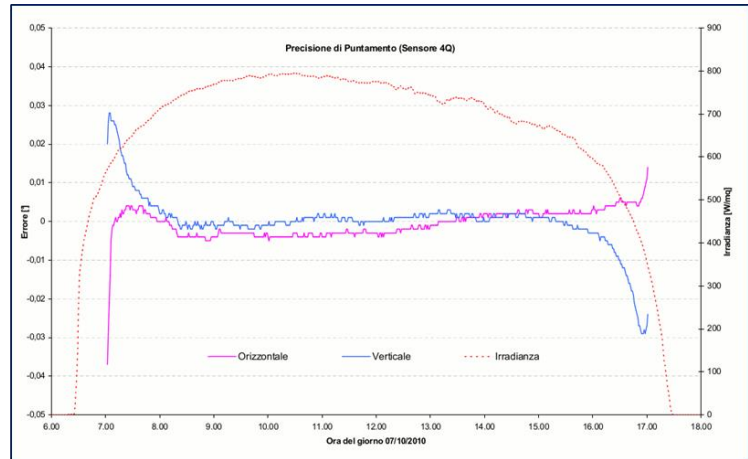
Figure 14. The OED mounted on the heliostat and a typical daily misalignment report.

This device is mounted with the base resting on the tracker surface and it can be left in data acquisition modality during the tracking operation time; it is able to record the average, maximum and minimum value for azimuth and altitude errors. Moreover, by combining azimuth and altitude errors, the overall misalignment angle during the time is calculated by the device software. In the graph of the Figure 14, are reported the direct irradiance values (orange curve), the azimuthal (pink curve) and altitude (blue curve) average misalignments acquired during a whole testing day of our heliostat prototype. The extreme heliostat accuracy can be appreciated together with a very high sensitivity of our equipment. A this regard we proved that the OED can relive also the very low change of the actuators reduction ratio during the day that can be due to very low imperfection of the mechanical components shape.

The detected data can be compared with the wind speed measurements during the same period in order to have an idea of the influence of this factor on the tracker features. In particular, considering different acquisitions carried out with different levels of wind speed, it is possible to define the tracker accuracy as a function of wind speed. It is also suggestable to use at least three OEDs in order to measure the accuracy in different points of the structure (at the center and on the corners).

1.3.5.2 *Actuators backslash measurement*

The procedure used for the measurement of the actuators backslash foresees the use of a laser generator mounted perpendicular to the tracker surface using a mechanical support stiffly connected to the heliostat structure and equipped with an adjustable flange to correctly orient the beam generator. The procedures both for azimuth and elevation motions have to be carried out during days with no wind in order to minimize the influence of wind on the results.

Azimuth motion

1. The panel is oriented perpendicular to the ground so that the laser beam is horizontally oriented.

2. The laser generator is switched on, so that it projects the beam to a vertical surface (a wall or a screen) distant at least 20-30 meter from the heliostat pillar.

3. The panel is rotated clockwise by few degrees to reach a starting position. In this

configuration the laser projection is marked on the wall (point A).

4. From the starting position, the panel is rotated before clockwise and after counterclockwise by the same angle (as example 2°-3°) in order to came back to the starting position. Here the new laser projection is marked on the wall (point A').

5. The azimuth backlash, α, is evaluated by the following formula:

$$2\alpha(rad) = \frac{\overline{AA'}}{d}$$

where AA' is the distance between the laser projections and d is the distance between the laser generator and the wall or screen.

This procedure can be repeated in different starting position of the panel in order to verify if the azimuthal backslash is constant.

Altitude motion

1. The panel is oriented perpendicular to the ground so that the laser beam is horizontally oriented.

2. The laser generator is switched on, so that it projects the beam to a vertical surface (a wall or a screen) distant at least 20-30 meter from the heliostat pillar.

3. The panel is upwards rotated by few degrees to reach a starting position. In this configuration the laser projection is marked on the wall (point B).

4. From the starting position, the panel is rotated before upwards and after downwards by the same angle (as example 2°-3°) in order to came back to the starting position. Here the new laser projection is marked on the wall (point B').

5. The altitude backlash b is evaluated by the following formula:

$$2\beta(rad) = \frac{\overline{BB'}}{d}$$

where BB' is the distance between the laser projections and d is the distance between the laser generator and the wall or screen.

1.3.6 UNAM

The methodologies implemented by UNAM, in collaboration with UNISON, in the Hermosillo solar tower are the following:

1.3.6.1 Heliostat sun tracking test

This test allows analyzing the sun tracking algorithms of the heliostat, as well as the tracking accuracy of the mechanism by operating the heliostat as sun tracker. A camera is mounted in the center of the heliostat supporting structure, which acquires a series of images of the sun

through the day (See Figure 15). If tracking was perfect the image of the sun should stay at the same location in the CCD.
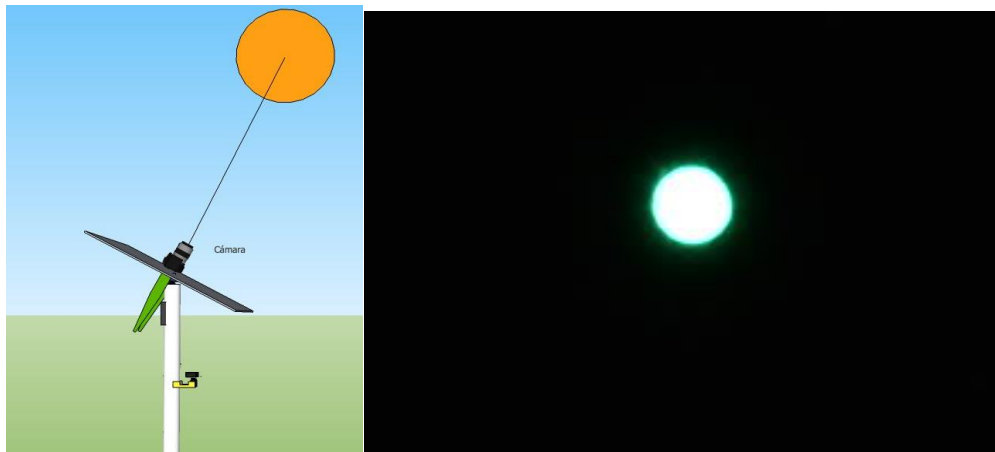
Figure 15. Scheme of the sun tracking test (left), and an image of the sun (right).

The software processes the acquired images and calculates the statistical difference values between the start position and the final at any moment of the day, as shown in Figure 16.
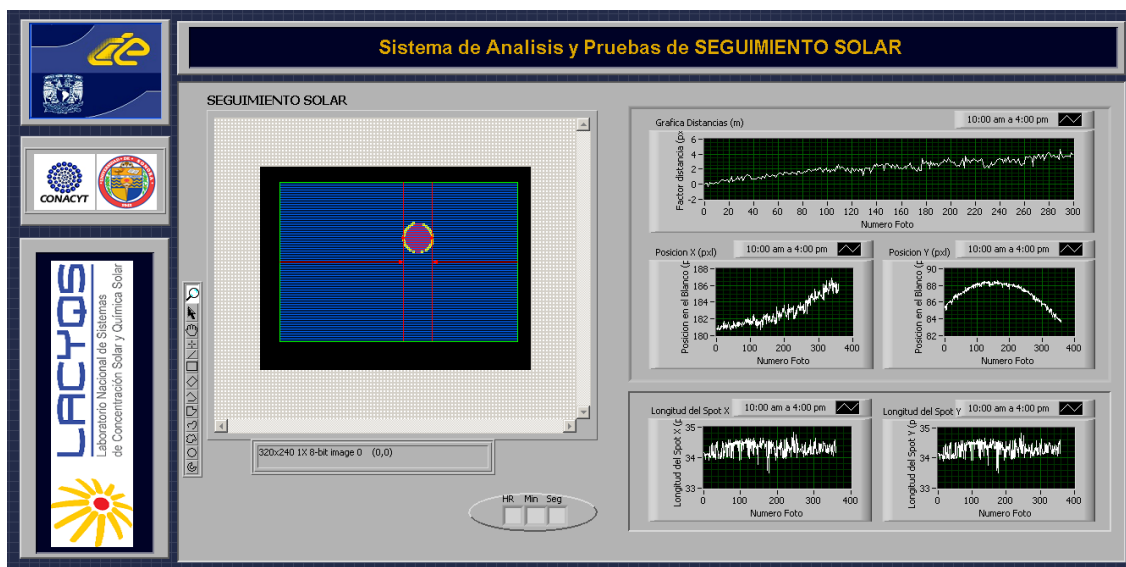
Figure 16. Front end for the Heliostat tracking test.

This system comprises the following equipment:

- Heliostat.
- AVT Pike CCD camera and mounting structure.
- Sun filter.
- Supporting structure.
- Labview programming software.

1.3.6.2 Solar spot test

This test allows studying the form and drift of the solar spot as a function of time. Images of the spot in a well-characterized Lambertian screen are acquired at predefined intervals. The

pictures are then subjected to a series of correction treatments to obtain the centroid of the image as well as the linear dimensions. Figure 17 shows a typical setup test and analysis.

Figure 17. Front end of the solar spot test.

This system comprises the following equipment:

- Lambertian screen (7 m × 8 m). Mounted on the tower with its center at 20 m height.
- AVT Pike CCD camera, located at 70 m from the tower.
- Telephoto lens.
- Labview programming software.

1.3.6.3 Fringe Reflection Test

The fringe reflection test (also known as Deflectometry test) is a qualification technique that falls into the category of structured light reflections techniques, in which a series of sinusoidal fringe patterns are projected on a screen and its reflection with the specular surface is acquired as an image by a digital camera.

As seen from Figure 18 and Figure 19, a video projector is used to project the stripe patterns on the Lambertian target located on top of the tower. The heliostat is then oriented in such a way that a camera located in the tower is able to "see" the reflection of the pattern by the heliostat and acquire an image.
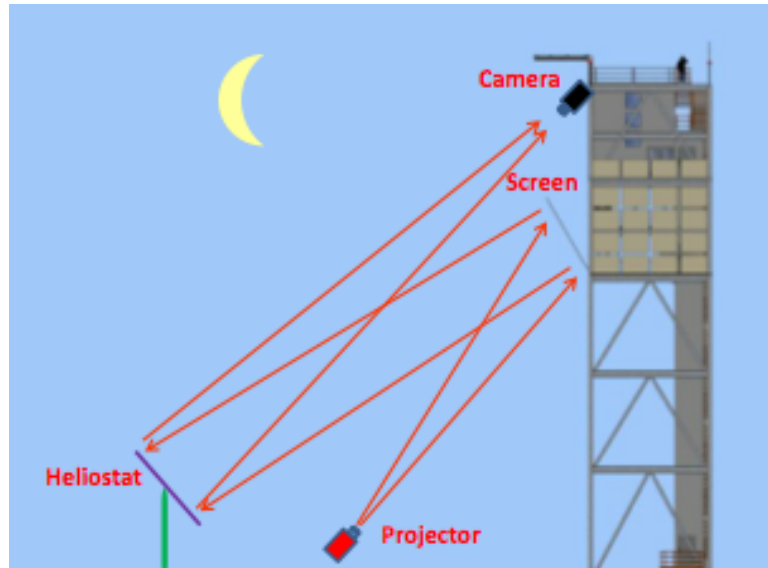
Figure 18. General scheme of the fringe reflection test.
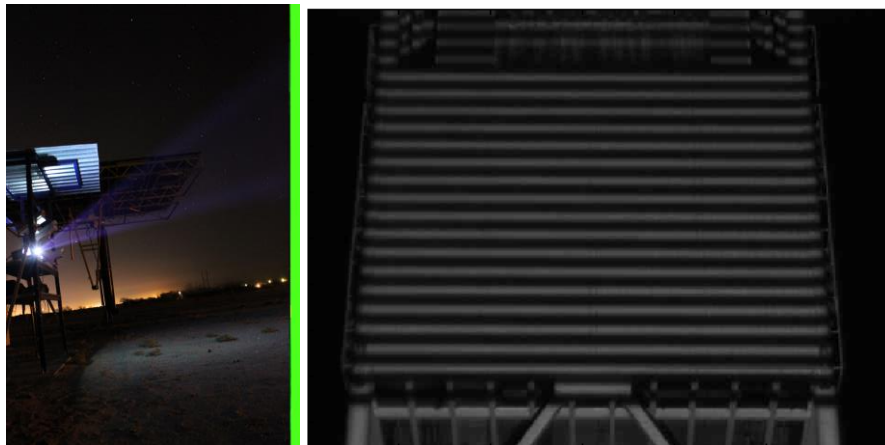
Figure 19. Projector and camera cluster (Left) and stripe pattern on Lambertian target (Right).

Then, the observed distortions in the image can be related directly with deviations of the ideal surface geometry by using a mathematical model to retrieve the slope information and comparing it with the theoretical model (See Figure 20).
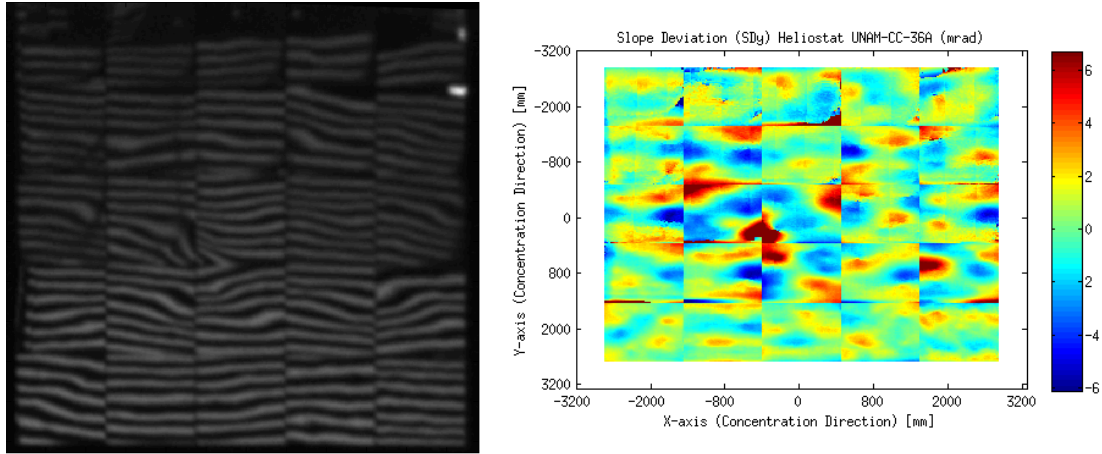
Figure 20. Image of the heliostat under fringe reflection test (left) and slope deviation map in one direction of evaluation (right).

Relevant aspects of the technique are its high spatial resolution (more than a million points per facet), relatively short measurement time and a simple and low cost arrangement. This technique allows obtaining the facet canting information, as well as slope error.

This system comprises the following equipment:

- Lambertian screen (7 m x 8 m).
- Video projector of at least 1100 lumens.
- AVT Pike CCD camera, mounted at 25 m height in the tower.
- Telephoto lens.

1.4   Proposed tests

In the following pages, a series of tests to identify the performance of various parameters identified in Section 1.2 is proposed.

For each heliostat tested, a datasheet containing pertinent information and presented below should be completed.

1.4.1   Sample heliostat datasheet

Heliostat Name/Model		
Manufacturer		
Year of construction/design		
Total Area	Height	
	Width	
Facet	Height	
	Width	

	Thickness	
	Number	
Facet construction		
Glass manufacturer		
Reflectivity		
Optical accuracy		
Drive type		
Controller type		
Tracking accuracy		
Pedestal Type		
Foundation type		
Weight (excl. foundation)		
Wind Speeds	Fully operational	
	Survival	
Heliostat cost breakdown (%)	Mirror	
	Frame	
	Structure	
	Drives	
	Pedestal	
	Control System	
Unit cost		
Heliostat Picture		

Test 1. Local control

Parameter	Local control
Description	Behaviour of local control under different conditions.
Acquired data	Encoder values Visual Inspection
Equipment	PC and control software
Protocol	Send the following commands and verify the correct behaviour according to a visual inspection and the axis encoder values: Reference search Security Defocused tracking Normal tracking Fixed positon (stow, cleaning, etc.) Configuration
Time	Repeat each test three times.
Conditions	-

Test 2. Local control under error conditions

Parameter	Local control
Description	Verifiy the behaviour under error or emergency conditions.
Acquired data	Encoder values Visual Inspection
Equipment	PC and control software
Protocol	Cause the following situations and verify the response by visual inspection, encoder values and error diagnosis of the local control: Power loss Communication loss Local control fault Control system limits Component fault (motor, encoder, ...)
Time	Repeat each test three times.
Conditions	-

Test 3. Optical quality of heliostat

Parameter	Optical quality
Description	Measure the reflected image of the heliostat to asses its optical quality.
Acquired data	Heliostat projection at a lambertian target Lambertian target Sun image Reflectivity Solar data
Equipment	Image capture system Lambertian target Metrological station Reflectometer
Protocol	Capture a least three reflectivity values (in case σmedia < 89 % wash with demineralized water) Focus at center of lambertian and take image Defocuse heliostat and take image of target Repeat 2) and 3) tree times Take image of sun Repeat several times
Time	Mid-day ± 15 min
Conditions	Clean sky DNI > 850 W/m2 Low wind speed

Test 4. Daily evolution of optical quality

Parameter	Optical quality
Description	Measurement of daily evolution of heliostat image, to determine influence of astigmatism and structure deformations onto the image.
Acquired data	Heliostat image at lambertian target Image of sun Solar data Reflectivity
Equipment	Image capture system Lambertian target Metrological station Reflectometer
Protocol	Ensure reflectivity > 89 % Focus on lambertian center Defocus and capture lambertian Capture image of sun Repeat 2), 3) and 4) evey 30 minutes
Time	Sunrise to sunset
Conditions	Clean sky DNI accordint to time of day Low wind speed

Test 5. Focusing quality

Parameter	Tracking accuracy and precision
Description	Measurement of daily evolution of the flux maximum on lambertian target.
Acquired data	Heliostat image at lambertian target
Equipment	Image capture system Lambertian target
Protocol	Focus on lambertian center. Take image every 5 minutes.
Time	Sunrise to sunset
Conditions	Clean sky DNI accordint to time of day Low wind speed

Test 6. Intrinsic focusing quality

Parameter	Tracking accuracy and precision
Description	Precision measurement of evolution of the flux maximum on lambertian target.
Acquired data	Heliostat image at lambertian target
Equipment	Image capture system Lambertian target
Protocol	Focus on lambertian center. Take image every second.
Time	Mid-day ± 3 min
Conditions	Clean sky DNI accordint to time of day Low wind speed

Test 7. Total power consumption

Parameter	Power consumption
Description	Measurement of daily power consumption at design point.
Acquired data	Axis encoder values.
Equipment	Electriciy meter
Protocol	With the heliostat in initial position read electricity meter. Simulate tracking for a spring day reading consumption every 30 min.
Time	Sunrise to sunset
Conditions	-

Test 8. Wind load testing

Parameter	Measure heliostat behaviour under wind loads.
Description	Measure deviation between ideal and actual heliostat focus point.
Acquired data	Image of heliostat at lambertian Metrological data
Equipment	Image capture system Reflecometer Metrological station
Protocol	Ensure heliostat reflectivity > 89 % Normal or reduced operation tracking Measure wind direction and speed Take image of heliostat evert 60 seconds during 60 minutes. Repeat 2), 3) and 4) for winds from E-W, S-N and N-S.
Time	Depending on weather conditions.
Conditions	Clean sky DNI > 800 W/m2 Wind speed > XX m/s

2 Testing results of the selected/developed heliostats

2.1 TEKNIKER-CENER's prototype

Sample heliostat datasheet:

Heliostat Name/Model		EASY
Manufacturer		IK4-TEKNIKER and CENER
Year of construction/design		2016
Total Area	Height	2 m
	Width	3.21 m
Facet	Height	2 m
	Width	3.21 m
	Thickness	4mm
	Number	1
Facet construction		Single facet
Glass manufacturer		
Reflectivity		
Optical accuracy		
Drive type		DC motor + cable based reduction
Controller type		
Tracking accuracy		< 1 mrad RMS
Pedestal Type		Post
Foundation type		Concrete
Weight (excl. foundation)		
Wind Speeds	Fully operational	
	Survival	
Heliostat cost breakdown (%)	Mirror	
	Frame	
	Structure	
	Drives	

	Pedestal	
	Control System	
Unit cost		
Heliostat Picture		

Introduction

The heliostat design from IK4-TEKNIKER and CENER features a cable based transmission drive system and an integrated fast calibration system. In order to evaluate both the quality of tracking and calibration system a prototype has been built and tested in cooperation with Ciemat at their PSA facilities. The heliostat was installed in the CESA-1 heliostat field, at about 380 m distance to the tower as shown in Figure 21.
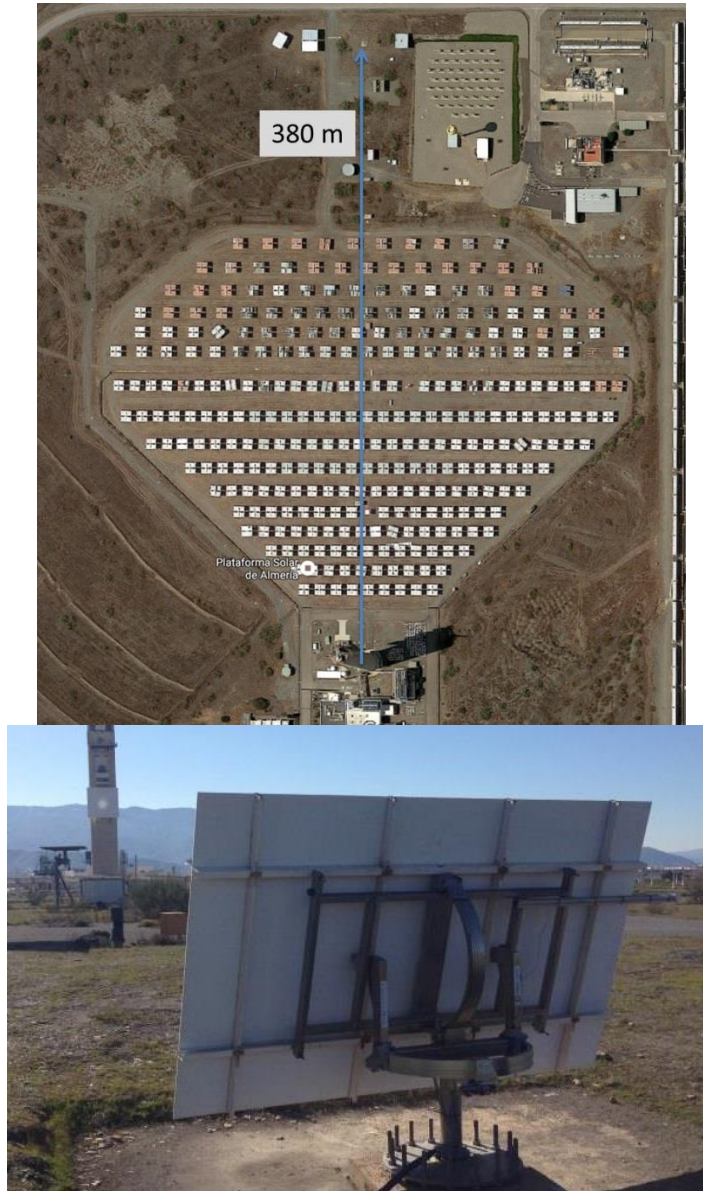
Figure 21. Test site with installed heliostat.

The testing was focused on the tracking accuracy and not the optical quality of the heliostat; for this reason an already existent facet (3.21 x 2 m) from the PSA was mounted on the heliostat. Furthermore, the reflective area of the facet has been reduced to a 1 m^2 area by applying painting to most of the facet (Figure 22). In this way the influence of the facet shape onto the shape of the reflected spot is minimized allowing for a good circular spot and hence a good estimation of the center of the spot on the target surface. By using such a large facet and

reducing its reflective area instead of directly using a small facet the impact of wind loads and other mechanical implications on the tracking accuracy is well reflected in the test results.

Figure 22. Reduced optical area of facet to focus on tracking accuracy.

Preparation

After putting the heliostat in place and connecting it with the control system, the heliostat was calibrated using the integrated calibration system. For this the heliostat was equipped with a camera which is used to observe different targets which have been distributed throughout the solar field (Figure 23).
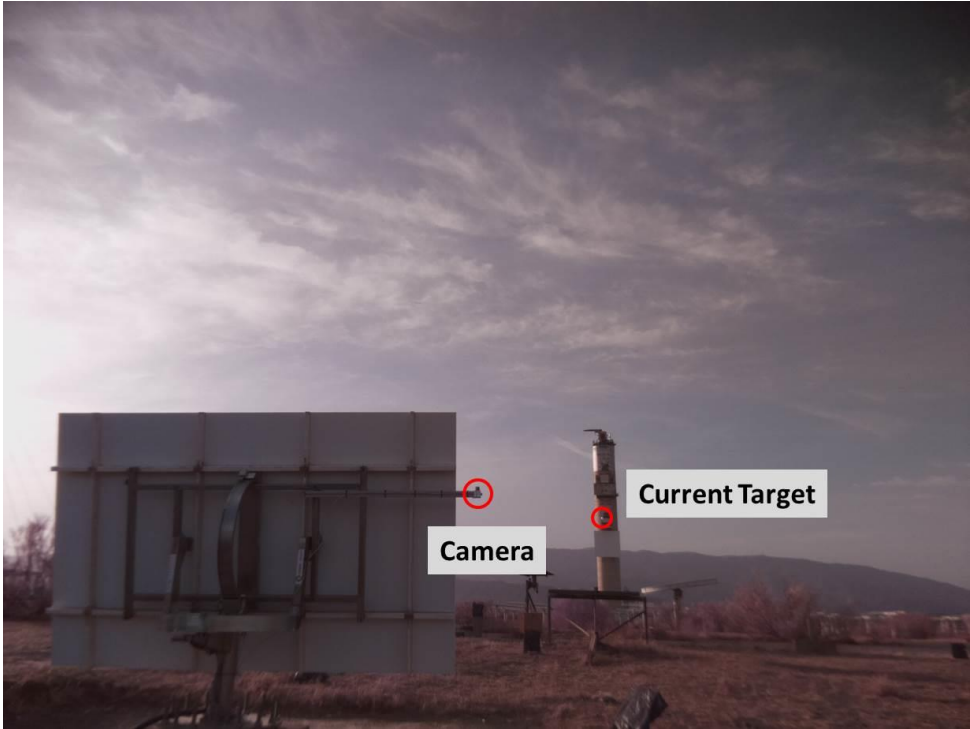

Figure 23. Heliostat is moved so the camera can capture the current target.

In order to facilitate the testing the targets have been placed at well-known positions respectively at easily measureable positions, which in this case means attached to other heliostats and the tower as shown in Figure 24.
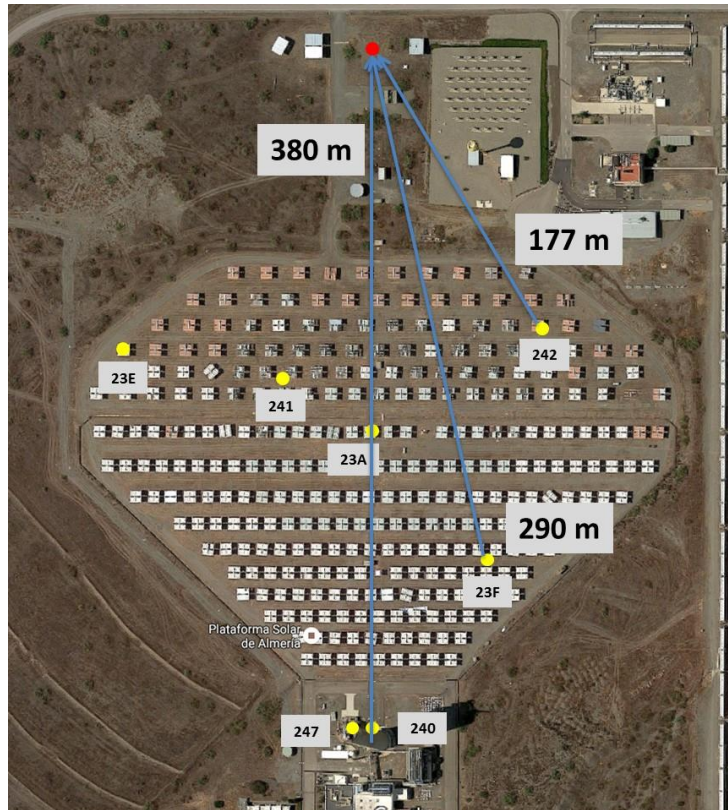
Figure 24. Target distribution used for calibration.

During calibration the heliostat is moved so that the camera can observe the targets under different orientations. Using the heliostat angles, the positions of the targets and their pixel position within the captured images the heliostat has been calibrated according to the approach described in [23]. According to evaluations of the kinematic system, the movement error of the heliostat can be estimated to be in the order of 0.2 mrad. Figure 25 shows an exemplary captured image, where the expected positions of the different targets according to the calibration result have been marked. As can be seen for the target in the lower left part of the image, the prediction conforms very well with the actual positions. The camera was equipped with an IR band-pass filter in order to facilitate the detection of the targets in the image.

Figure 25. Image of heliostat camera (with IR filter) with predicted target positions.

Tracking

After calibrating the heliostat, test of the drive system started. Therefore, during different days the heliostat was put into tracking mode, reflecting the sunlight onto a 12 x 12 m2 lambertian target. For evaluation the target was observed with a high precision digital camera which detects the center of the solar spot. The following results show the behavior of the heliostat during almost 7 hours of tracking where one picture of the target was taking every 2 minutes. The center point was obtained as the peak intensity of the solar spot. The coordinates of these points are shown in Figure 26.

TRACKING TEST: STATISTICS ANALYSIS OF AIMING POSITIONS:

|	
Test date...................................	= 25-Ene-2017
Test interval...............................	= 10:25:06 / 17:00:31 CET
Time between pictures............	≈ 120"
Sample size...............................	= 210 points
Offsets correction.....................	= No
Mean pointing position...........	= (0.069,-0.136) m
X-Y spatial correlation.............	= 0.22
Horz. Standard Deviation (XY)	= 0.155 m or 0.412 mrad
Vert. Standard Deviation (XY)	= 0.163 m or 0.433 mrad
Min. Standard Deviation (UV)	= 0.140 m or 0.370 mrad
Max. Standard Deviation (UV)	= 0.176 m or 0.467 mrad
Ellipticity...................................	= 1.3
Ellipticity direction	= 51.3 deg

Figure 26. Spatial distribution of points on target Surface.

In Figure 27 the evolution of the deviations in azimuth and elevation is shown.
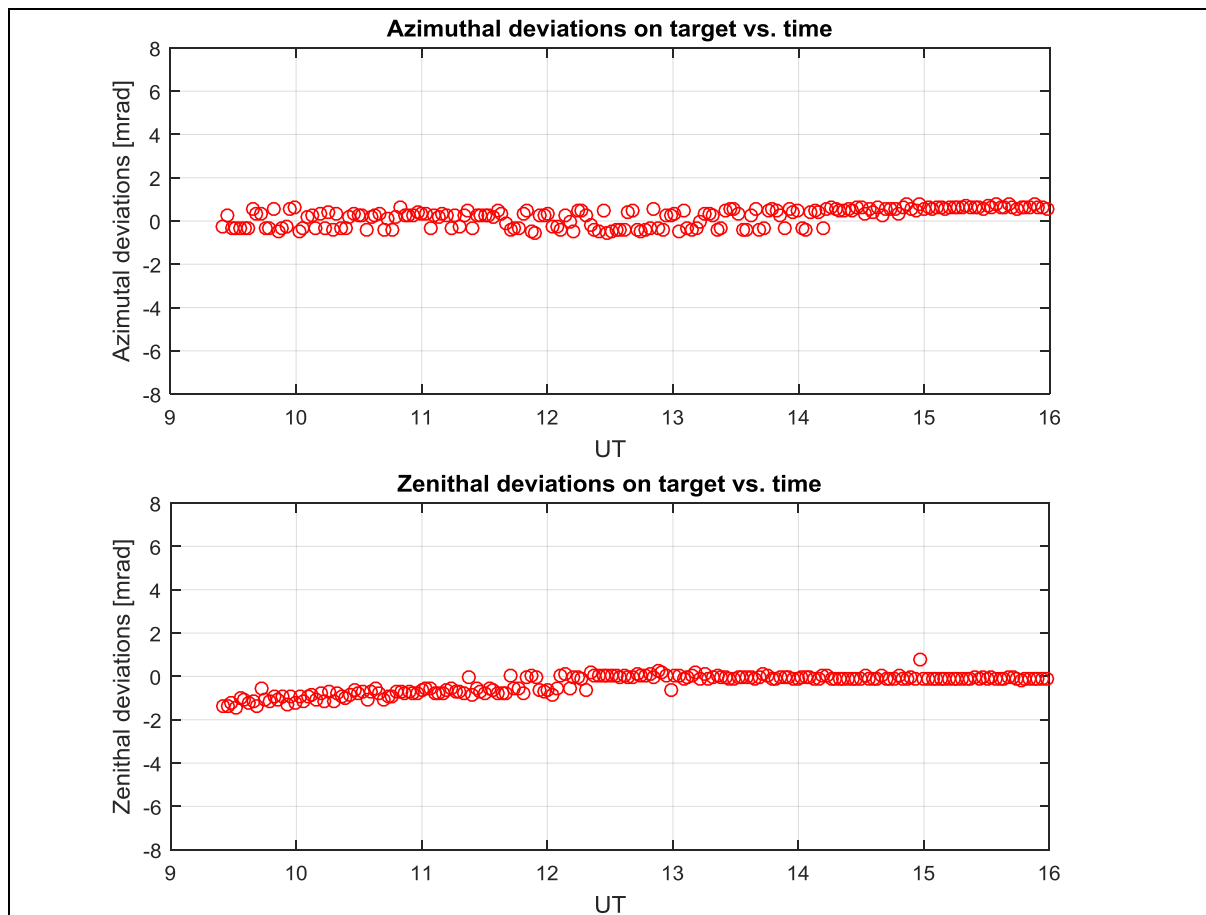
Figure 27. Evolution of error over time.

These deviations are due to errors in the driving system, calibration and control system of the heliostat. Part of the variability of the spot is also due to the low intensity of the solar spot and the problems this caused in reliably estimating the peak intensity. As can be seen from the evolution of the error there is a slight movement of the pointing center over time, which is due to a small calibration error. However, the overall error is still quite low.

2.2 Heliostats installed at CyI

Sample heliostat datasheet:

|		
Heliostat Name/Model		CSIRO 4.5m^2 (updated design: 5m^2, 2.25×2.25m, 1 facet)
Manufacturer		CSIRO
Year of construction/design		2014
Total Area	Height	2.44 m
	Width	1.85 m
Facet	Height	2.44 m
	Width	1.85 m
	Thickness	3mm
	Number	1
Facet construction		Single facet
Glass manufacturer		Guardian Glass
Reflectivity		93%
Optical accuracy		1mrad
Drive type		Linear actuator
Controller type		Open loop control, target aligned tracking, custom controller
Tracking accuracy		2 mrad
Pedestal Type		Post
Foundation type		Concrete
Weight (excl. foundation)		
Wind Speeds	Fully operational	
	Survival	> 150 km/h
Heliostat cost breakdown (%)	Mirror	
	Frame	
	Structure	
	Drives	

	Pedestal	
	Control System	
Unit cost		
Heliostat Picture		

Results according to the tests proposed in Section 1.4:

Local control:

Local control tests performed routinely. System is capable of:

Reference search for actuator "zero" position, Defocused tracking, Normal tracking, Stow to fixed position defined by user

Local control under error conditions:

System tested in cases of:

Power loss / communication loss -> system goes to (defined) stow position.

Control system limits -> system does not allow operation of heliostat to reach limiting position, sends heliostat to stand-by position.

Component fault -> system returns error message and identifies heliostat with component fault and particular component that failed.

Focusing quality and intrinsic focusing quality:

An image analysis software was developed to obtain statistics of the heliostat image formed on the Athalassa target. The software was developed in Matlab and uses the ImageAcquisition Toolbox and yielded the centroid of the heliostat image and some characteristics of the image, e.g. area and ellipticity. An example of the image processing steps performed is shown in Figure 28.
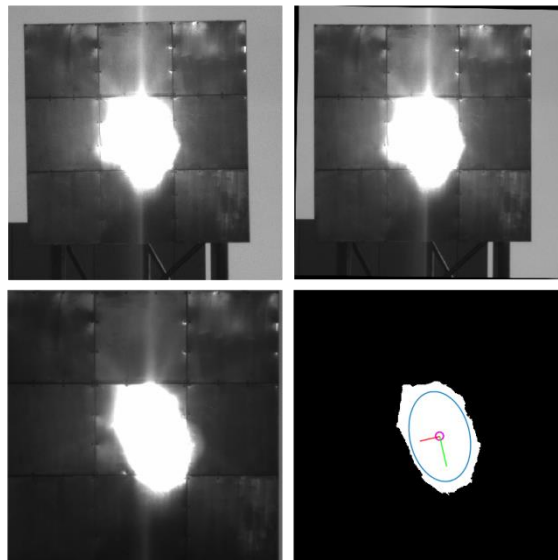
*Figure 28. Image acquisition and processing steps: (a) Image acquisition, (b) Perspective correction, (c) Cropping, (d)Thresholding and extracting image characteristics.*

The experiment consists of two heliostats, each with a single facet of 2.44×1.85m focusing at 35m. The image of the heliostats on a lambertian target consisting of a 2×2m painted aluminum sheet was sampled via a Basler Scout scA1300-32gm camera with a 50-mm lens

and an ND090 neutral density filter. Only one heliostat was tested at a time. The software was operated in a "fast" (1 image per second) and a "slow" (1 image per 20 seconds) acquisition modes.

Sample results for the "slow" (focusing quality) and "fast" (intrinsic focusing quality) acquisition modes are summarized in Figure 29 and Figure 30. Results obtained include the following information:

- The x- and y-axis image centroid locations as a function of time, presented as distance from the target (origin set at target edge, target is 2x2 m, so an {x,y} coordinate of {1,1} represents target center), and distance from target center normalized by slant range to yield an angle.
- The centroid data is also plotted as a scatter plot of distances from origin (plots of δy vs. δx in [m] and [mrad]).
- The image area is calculated both through image processing and through fitting an ellipse to the captured image.
- The orientation of the ellipse is presented as the angle between the ellipse primary axis and the vertical.
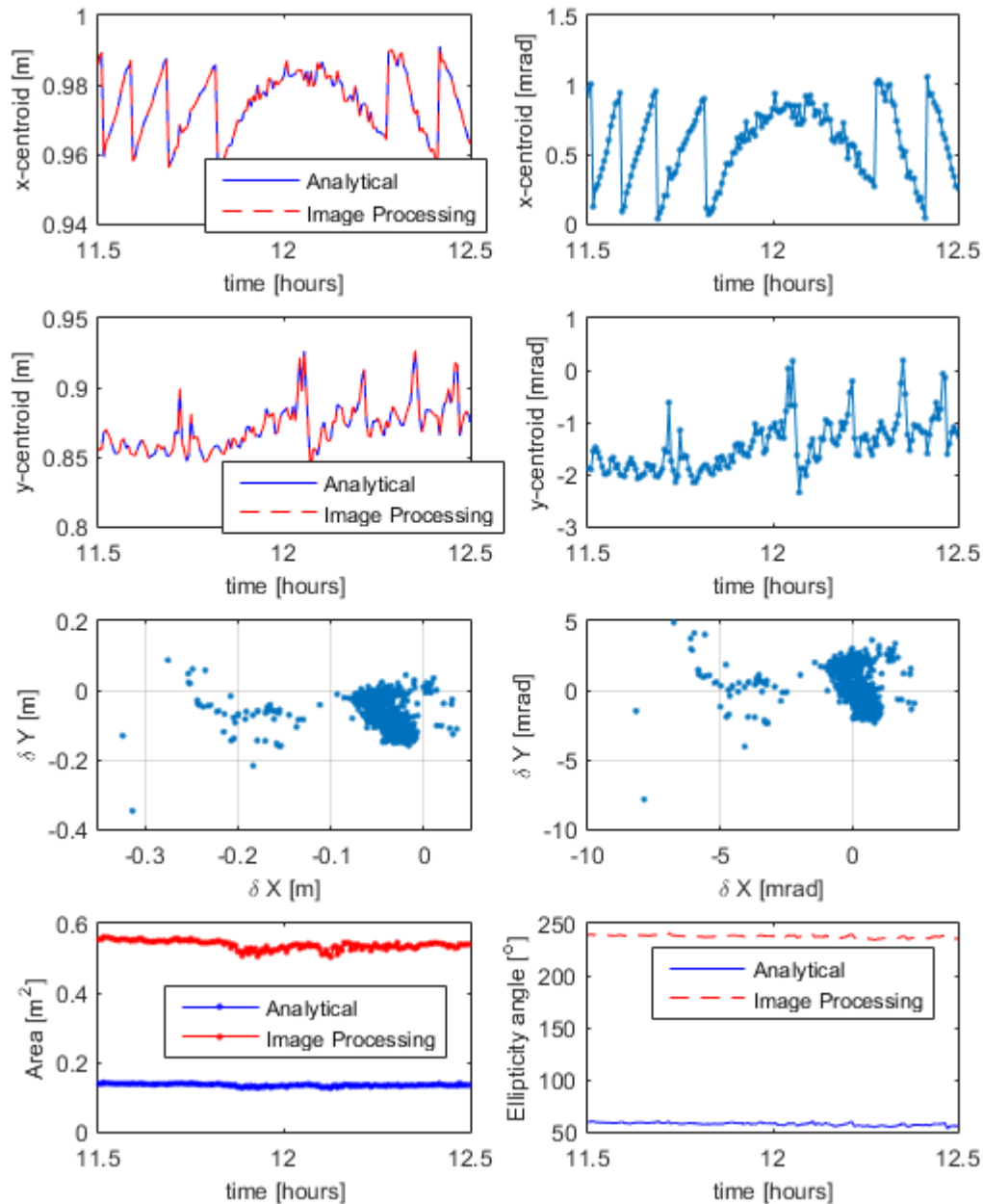
Figure 29. Sample results for "slow" acquisition mode. Results show distance and angular position of the image centroids in the x- (panels a & b) and y- (panels c & d) directions, scatter plots of offset in terms of distance and angle (panels e & f) and image area and ellipticity (panels g & h, respectively).

In Figure 29, the quantity of interest is captured in panel f, where the clustering of points may be visually seen to have an extent of ±4 mrad. Some outliers may be due to clouds during the acquisition period. Larger angular deviations are noted in the y-centroid position (panel d), due to the spin-elevation tracking mechanism employed by the heliostats. The offset of the aim point with respect to the target center, visualized by the center of the clustering of points in panel e, indicates a systematic offset in the aiming position of the heliostat, and the present data may be used to correct the aiming position.
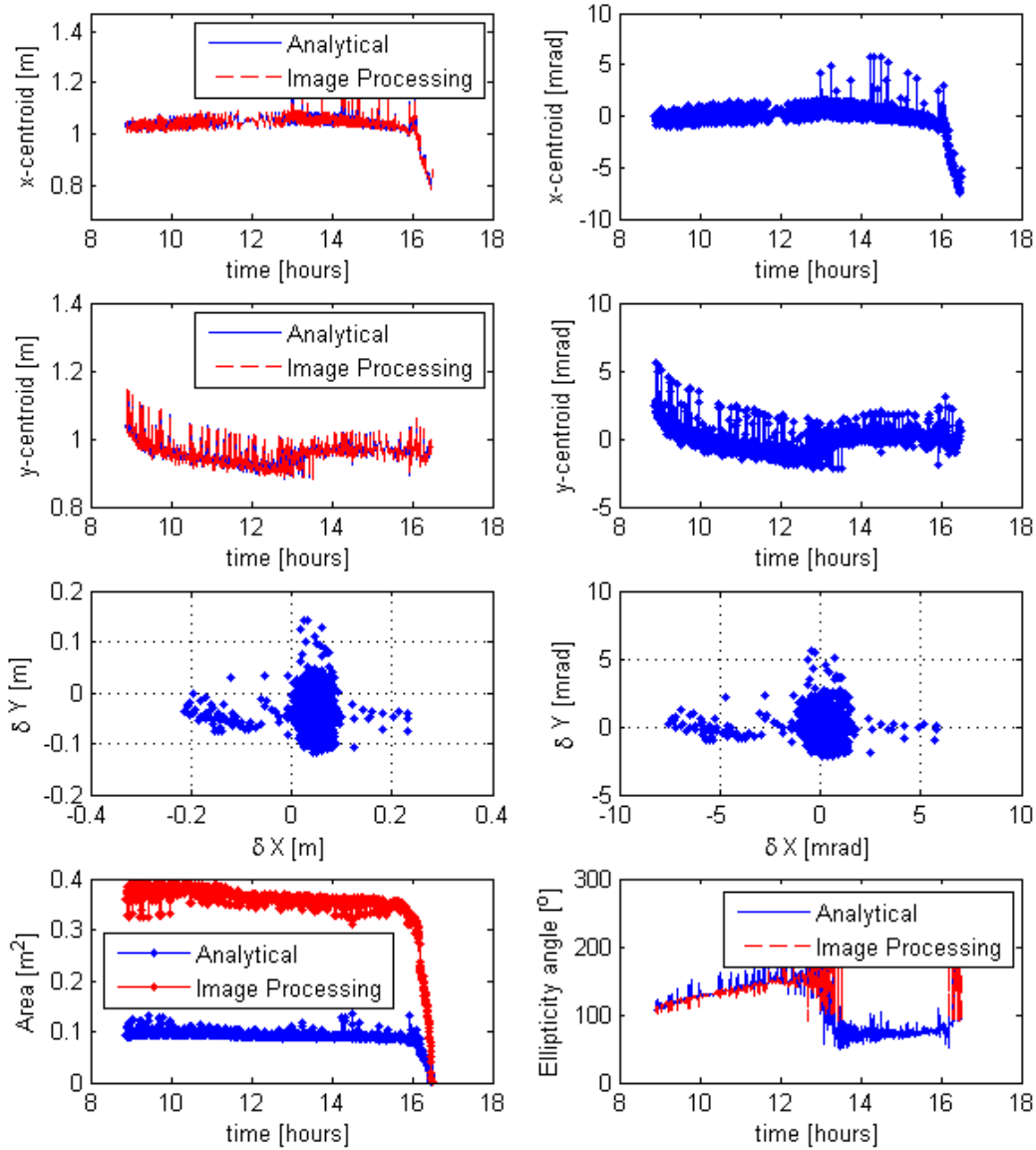
Figure 30. Sample results for "fast" acquisition mode. Results show distance and angular position of the image centroids in the x- (panels a & b) and y- (panels c & d) directions, scatter plots of offset in terms of distance and angle (panels e & f) and image area and ellipticity (panels g & h, respectively).

In Figure 30, the daily evolution of the measured quantities is presented. The rapid departure of the x-centroid from the mean position around 16:00 is due to the partial shading of the heliostat by a nearby structure before sunset. Further, "noise" appearing after 13:00 is due to small clouds present in the sky during the data acquisition period. Similar conclusions as in the "slow" acquisition case are drawn regarding the overall tracking accuracy.

2.3 Heliostat developed by ENEA

ENEA expects to carry out the tests of the heliostat by the end of March. A description of the prototype is presented:

A heliostat prototype has been designed and realized by ENEA in order to test the main mechanical components and the control system too.

A theoretical preliminary analysis has been carried out in order to define the heliostat size matching the best compromise between costs and performances. The results of the study revealed that the best solution in terms of mirror size is of 25 sqm, we developed a smaller area prototype about of 6sqm. This is due to the fact that a 25sqm tracker has to be fixed on a foundation in concrete about of 3,5 cubic meter placed in an excavation pit. Because the ENEA research centre is located in an area subjected to constraints imposed by environmental laws, for the realization of these works we should need to obtain several authorization (from Municipality, from environmental superintendence office, from the so called "Genio Civile", etc). This would take a long time and the prototype would not have been ready for the established project deadline. For this reason we chosen to realize a small area prototype, mounted on a metallic basis that can be easily moved using a mechanical forklift: in this way any authorization is required for its use.

In any case for the design of the heliostat moving group, that is the most important part of the system, we used the same commercial slewing drives identified for the 25 m^2 heliostat. Then the aim of the realization of this prototype is to test the effectiveness of the choice of the slewing drives and to test the control system that has been ad hoc designed and realized for it.
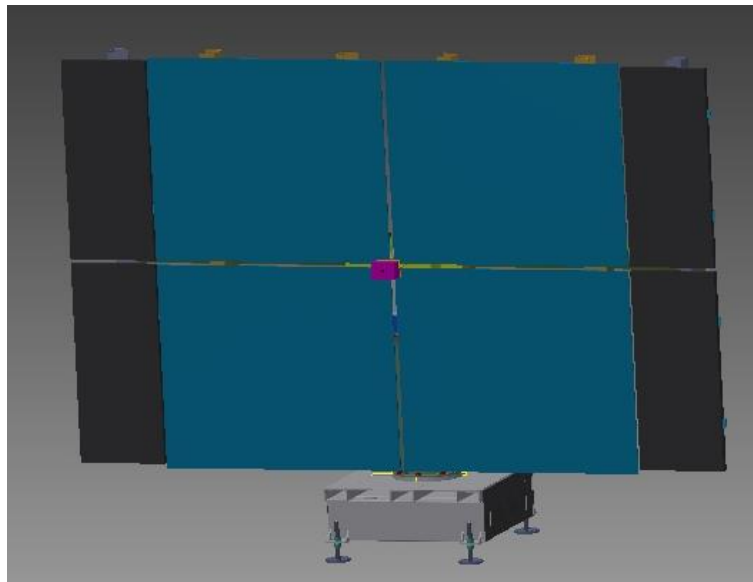

Figure 31. Frontal view of the heliostat.

In particular, we developed a complete independent and wireless system: the control system is powered by some PV panel mounted on the mirror surface and a specific feedback sensor is devoted to make the needed tracking corrections so that the beam reflected by the mirrors hit perfectly the target.

In the following paragraphs, the description of the mechanical and electric/electronical aspects is reported.

The overall view of the tracker is reported in the next picture. Its tracking surface is constituted by four mirrors placed in the central part and four small PV panels on the two lateral sides. The feedback sensor is positioned perfectly at the intersection of the mirrors.

These components are mounted using metallic supports bolted on vertical beams in turn fixed on two horizontal shafts. These latter are connected, by means a mechanic hub to a first slewing drive allowing the rotation of the plane around the horizontal axis (elevation motion). A T shaped mechanical support connects the first slewing drive to the second one which manages the rotation around the vertical axis (azimuth motion). The lower fifth wheel of this component is fixed on the vertical pillar upper flange. All the system is mounted on a metallic square basis resting on the floor by means of four height adjustable supports. These latter are used during the first installation of the heliostat in order to put the pillar axis in vertical position.
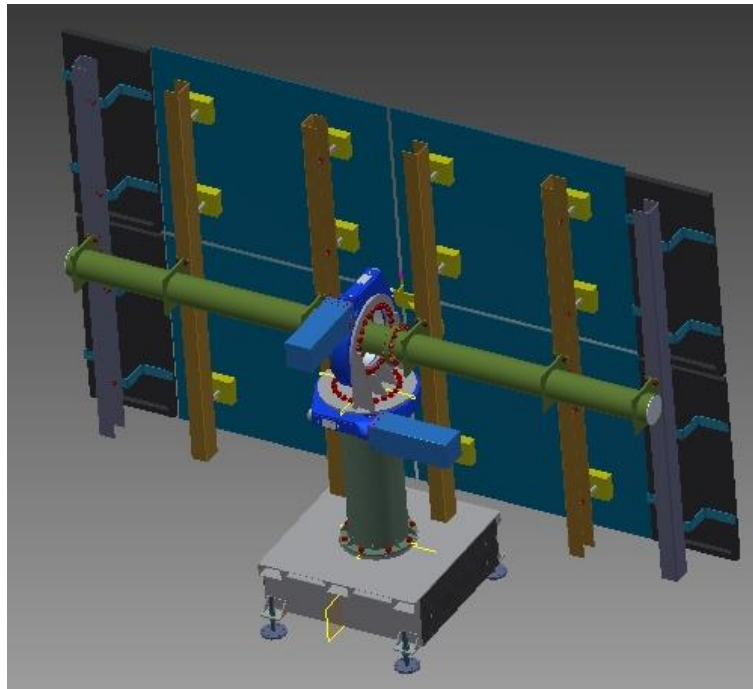
Figure 32. Back view of the heliostat.

2.3.1   Motion Group

This group is the most important part of the tracker because it is responsible of the correct positioning of the mirror surface in the space and consequently of the right direction reflection of the solar beam. It is composed by two identical sub-groups, the first one for the altitude and the second one for the azimuth motion interconnected with a T shape metallic support.

With reference to the next figure, each group is composed by the following components:

1 Slewing drive produced by IMO Company, model WD-LC 0343/3-08501. It presents a reduction ratio of 1:86 and a maximum angular back lash of ± 0.037°; moreover the chosen version is treated with anticorrosive processing assuring long operation life also in outdoor conditions.

2 A shaft with double diameter connecting the output shaft of the epicycloid reduction gear and the input section of the slewing drive.

3 An aluminium block connecting the two mechanical gearboxes.

4 An epicycloid gearbox from Bonfiglioli Company, model "TR 080 2 15 LOW 73A1 CD 9.52 S5 OR SB KE", with reduction ration equal to 1:15, and maximum angular back lash of ± 0.037°.

5 A stepper motor from MAE Company, model MAE HN2003451_0640BX08 connected to the Bonfiglioli epicycloid gearbox.

6 A carter realized in steel sheet having the function to protect the motor from the environmental agents: it presents some holes for the cable routing.
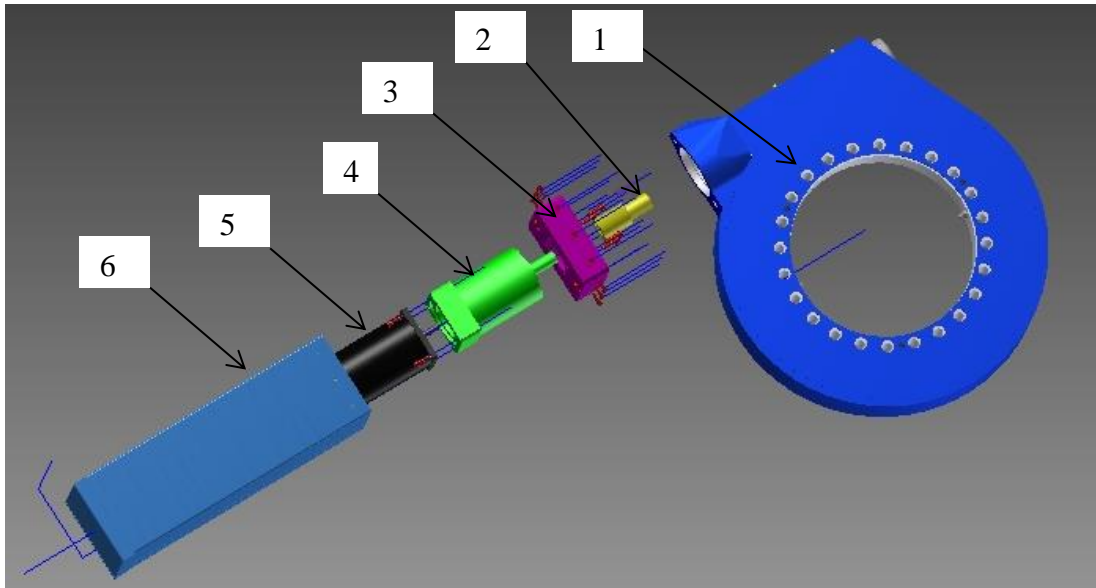

Figure 33. Exploded view of the motion group.

Next chart reports the characteristic curve of the used motor (see curve B). During the tracking phase, as better specified in the description of the control system, motors are controlled in "micro-stepping" mode, then at a very low speed.
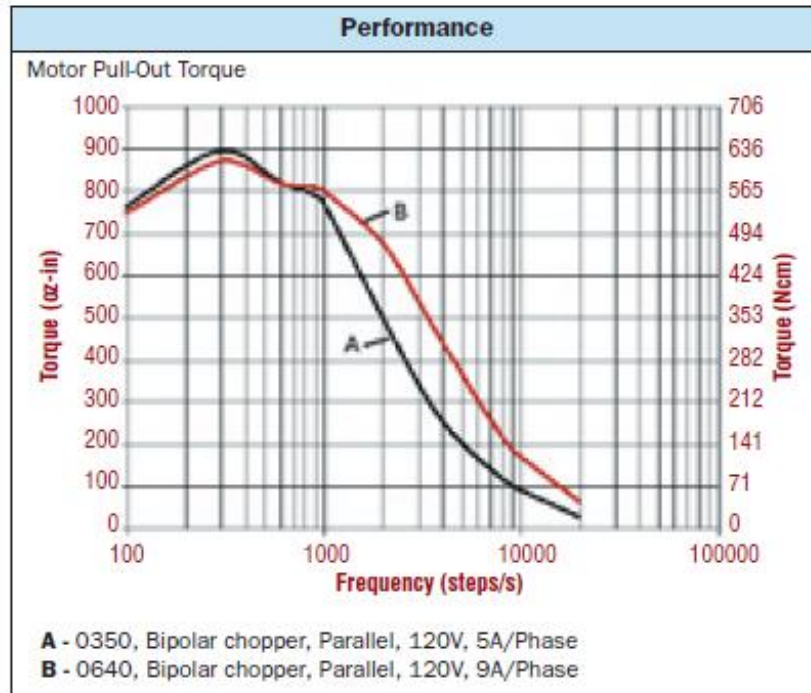
Figure 34. Characteristic curve of MAE HN2003451 stepper motor.

When the tracker has to reach in short time a determined position, as in the case of recovery in safety position due to high wind speed, the control system sets the motor rotation speed at the chosen maximum speed of 1000 steps/second, corresponding to 300 rpm.

In this condition, the motor output torque is about of 800 oz-in, corresponding to 5,65 Nm; considering that the total reduction ratio is of 1:1290, the maximum panel rotation speed is about of 0,232 rpm: this means that to reach the safety position, corresponding to the mirrors plane parallels to the ground, the trackers takes, in the worst condition, occurring if the starting panel position is vertical, about 64 sec.

Regarding the torque, we have to consider a global transmission efficiency about of 50%, then the available torque at the axis (both azimuth and elevation) is about of 3645Nm, that is much higher than the values calculated for an heliostat of this size that are of 1500Nm and 1800Nm respectively for elevation and azimuth axis.

2.3.2 Description of the control system

The realized control system manages all the components needed for the correct heliostat working, such as: actuators, sensors, power supplies, etc. Its main features, deeply described in the following paragraphs, are the following:

- Power supply and control of azimuth and altitude motors.
- Proximity sensors management.
- Feedback sensors management.
- Controlling of the PV panels MPPT function.

- Control of the charge/discharge batteries function.
- Management of the system remote communication function.

In the next figures, a block diagram and a picture of the control system box are reported.
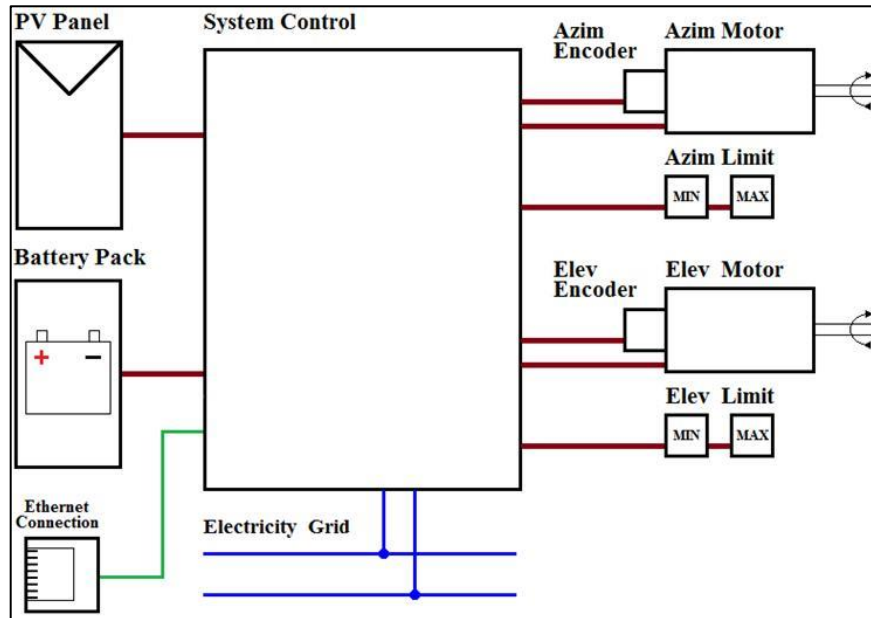
Figure 35. Control system block diagram.

Figure 36. Heliostat control system box.

The control system is connected to the PV panels mounted on the tracker, in order to charge the batteries pack, but it is designed also for the connection to the external electrical greed in case of need.

The features of the 4 PV panels mounted on two lateral edges of the tracking plane, are the following:

- Voltage at open circuit conditions $V_{oc} = 21.8V$

- Voltage at maximum power point condition $V_{mpp} = 17.8V$
- Current at short circuit condition $I_{sc} = 3.2A$
- Current at maximum power point condition $I_{mpp} = 2.9A$
- Maximum dc power $P_{max} = 51.6W$

The PV field has been sized so that the energy produced during the sunny days is enough to supply the heliostat for at least a couple of raining or cloudy days.

The storage system consists of 4 cyclic batteries series connected and placed in a box realized in the bottom part of the heliostat. Their weight concurs to the structure stability against wind load. Main features of each battery are following reported:

- Nominal voltage $V = 12V$
- Discharge capacity in 20 hours @10.5V-20°C $D_1 = 24$ Ah
- Discharge capacity in 10 hours @10.8V-20°C $D_2 = 21.1$ Ah
- Cyclic charge voltage $V_c = 14.5V \pm 3\%$
- External dimensions   16,6 X 12.5 X 17.5   (cm)
- Weight   9 Kg
- Cyclic life @100% DOD   300   (cnt)
- Cyclic life @50% DOD   600   (cnt)
- Cyclic life @25% DOD   1400   (cnt)

The connection to the electric grid is available in the case of failure of the PV stand-alone system; moreover, for safety raisons, through an Ethernet communication channel, the tracker can be also moved from a remote computer.

Azimuth and altitude motions are realized by two stepper motors supplied using the 2 poles configuration, so that they can provide high torque also at high rotation speed conditions. The "micro-stepping" control modality allows to reach high tracking accuracy and to reduce events of vibration and mechanical resonance of the structure.

Tracking accuracy is continuously checked, measuring the effective rotation of the motors axes using two differential encoder each one connected to a motor shaft.

Following are reported motors and encoder technical specification:

Stepper Motors MAE HN2003451_0640BX08

- Rated Phase Current   6.40 (A)
- Phase Resistance   0.50 (Ω)
- Phase Inductance   2.5 (mH)
- Holding Torque Unipolar   620 (Ncm)
- Holding Torque Bipolar   760 (Ncm)
- Detent Torque   23 (Ncm)
- Rotor Inertia   1800 (g-cm^2)
- Motor Weight (Mass)   3.6 (kg)

- Maximum Voltage 140 (V)

ENCODER

- Voltage supply 5 (V)
- Current Supply 0.08 (A)
- Differential encoding PHA-An, PHB-Bn, PHN-Nn
- Switching max frequency 300 (kHz)

2.3.2.1 Electronic motion controller

A block diagram of the electronic controller is reported in the next figure.
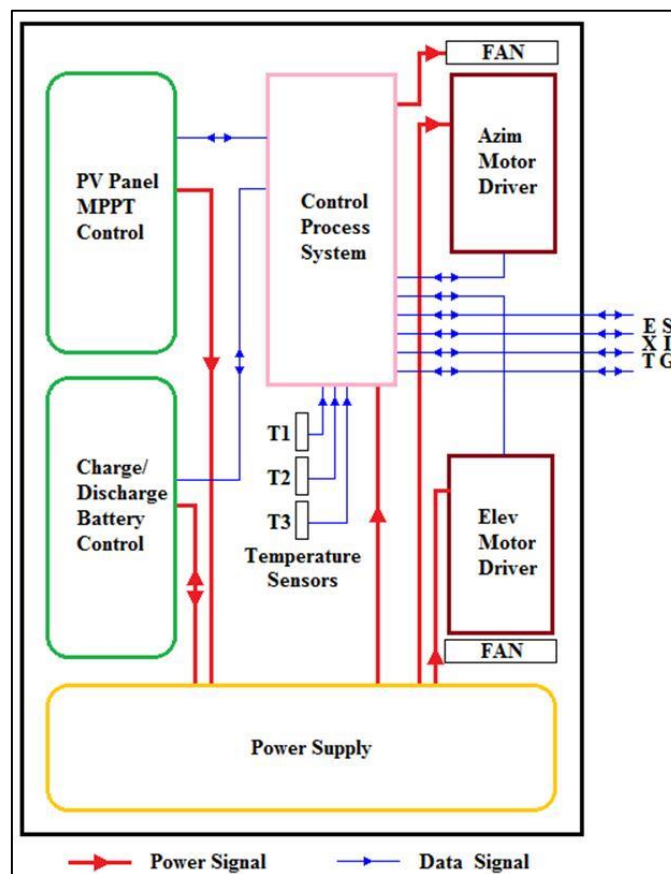
Figure 37. Block diagram of the controller.

The core of the controller consists of an electronic board "embedded" to the microcontroller. It has been designed and realized within the Portici ENEA laboratories and it has been programmed with the aim to carry out all the heliostat control functions, to measure its main working parameters, and finally to manage an Ethernet communication channel for the remote control.

Main controller features are:

- Actuation of the power driver for the stepper motor.
- Detection of the effective axes rotation.

- Detection of the feedback sensor signal and actuation of the tracking corrections.
- Management of the communication and of the remote controlling procedure.
- Measurement of the drivers working temperature and consequent cooling fans actuation.
- Management of the correct working of the MPPT function for the PV Panels.
- Management of the correct working of charge/discharge function of the storage system.
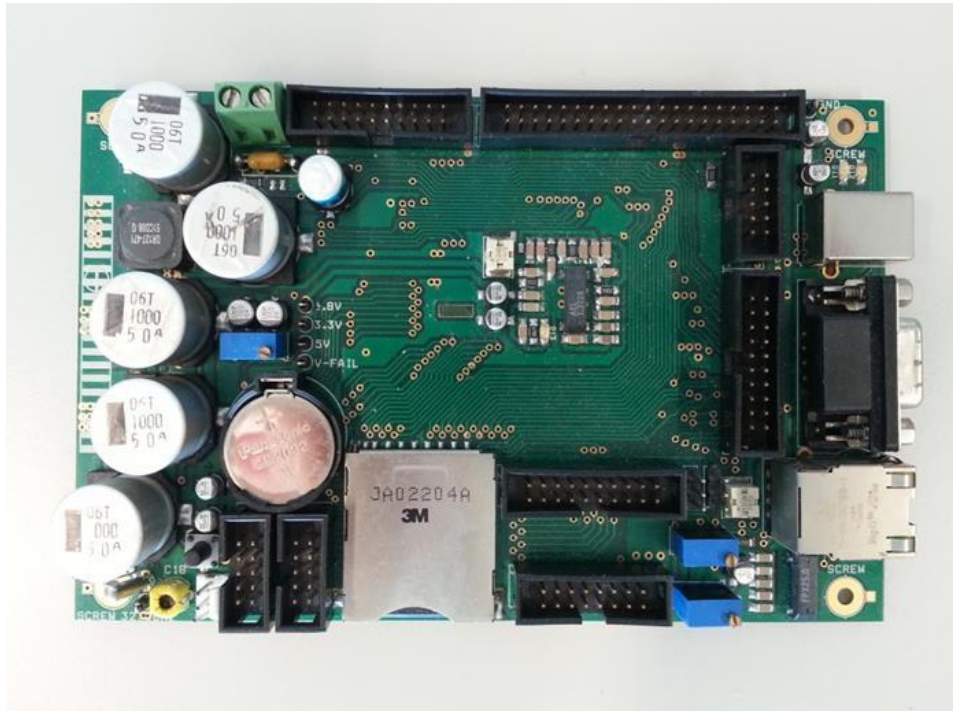
Figure 38. Electronic board "embedded" to the controller.

Commercial components have been chosen for the realization of the power drivers. They realize an optimal actuation of the motors and, using a specific command bus connected to the control board, they carry out several functions such as: supply of the current for the motors coils, realization of micro-stepping control, communication of the controller eventual failures.

Main technical specifications of these components are:

- Voltage supply   [min-max]   24-90 (V)
- Current supply   [min-max]   4-10 (Arms)
- Resolution up to   25600 (step/rev)
- Switching max frequency   300 (kHz)
- Chopping max frequency   20 (kHz)
- High efficiency
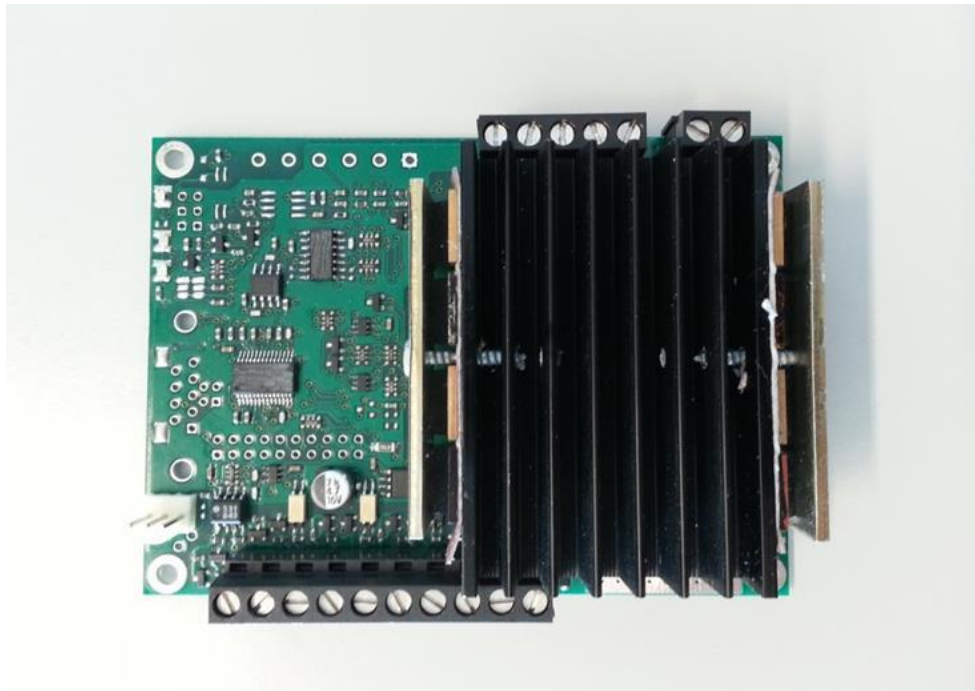
Figure 39. Electronic board of the stepper motor driver.

The PV panels MPPT system has been integrated in the heliostat control box and it has been designed in order to maximize the energetic production. It consists of a commercial integrated circuit devoted to these applications. It acts a "boost type" (step-up converter) dc-dc conversion, using an MPPT algorithm; it increases the dc voltage provided from the PV field in order to supply the motors drivers and in order to charge the batteries pack.

Moreover it is equipped with a communication bus channel used to transmit the working data, then fulfilling the function of PV panel and storage system monitoring. Main features of dc-dc converter are following reported:

- Photovoltaic Voltage supply [min-max]   35-80(V)
- Output voltage supply [min-max]   40-100(V)
- Photovoltaic input current [min-max]   1-10(A)
- Max Output current   10 (A)
- Efficiency [min-max]   70-96 (%)

2.4 Heliostat developed by UNAM/UNISON

Heliostat datasheet:

Heliostat Name/Model		UNISON-MC 1.5m^2
Manufacturer		University of Sonora
Year of construction/design		2012
Total Area	Height	1 m
	Width	1.5 m
Facet	Height	1 m
	Width	1.5 m
	Thickness	3mm
	Number	1
Facet construction		Single facet
Glass manufacturer		Vitro, of the shelf mirror glass
Reflectivity		92%
Optical accuracy		2.41 mrad
Drive type		Worm gear
Controller type		Open loop control, custom controller
Tracking accuracy		1.7 mrad
Pedestal Type		Post
Foundation type		Metal anchors
Weight (excl. foundation)		
Wind Speeds	Fully operational	20 km/h
	Survival	> 120 km/h
Heliostat cost breakdown (%)	Mirror	
	Frame	
	Structure	
	Drives	

	Pedestal	
	Control System	
Unit cost		$ 15.000,00 MXN
Heliostat Picture		

The tests were carried out at the Central Receiver Experimental field, in Hermosillo Sonora, a facility jointly developed by UNISON and UNAM within the Project National laboratory of Solar Concentration and Solar Chemistry (LACYQS). The heliostat was developed by *Departamento de Ingeniería Industrial* of UNISON, with financial support from PROMEP.

Qualitative observations:

In Figure 40 the 1.5 m² heliostat is shown. As can be appreciated, the reflection of the sun at a short distance from the tower (40 m) produces a compact bright image. However, there are apparent holes in the flux distribution, which hint to a curvature problem in the surface. This can be observed in detail in Figure 41, taken with the heliostat at 200m, where the existence of two main spots produced by the same heliostat, as if it were composed of two misaligned facets instead of one. The interpretation of this is that there is a strong bending of the facet around a vertical line, which produces two curved segments with more or less good individual focusing. Actually, it was observed that small loads easily deformed the heliostat frame structure.

Figure 40. Heliostat of 1.5 m² reflecting the sun at 40 m distance.

Figure 41. Image captured during the reflected spot test at 120 m distance.

Quantitative results:

The reflected spot test was carried out with the heliostat at 122 m from the tower. This gives a line of sight distance of 126 m to the target. In Figure 42 the X and Y curves of the heliostat image centroid are presented as a function of time. A clear drift is appreciable in the centroid position. On the other hand, there are oscillations around the main drift trajectory.

To characterize drift both curves were fitted by a third degree polynomial function to define the central tendency. The obtained polynomial coefficients are presented in Table 2. The drift is the characterized by the difference between the maxima and minima of the function in the considered interval. According to this, the maximum variation in the horizontal (X) direction was of 0.61 m, while in the vertical (Y) it was of 0.50 m.
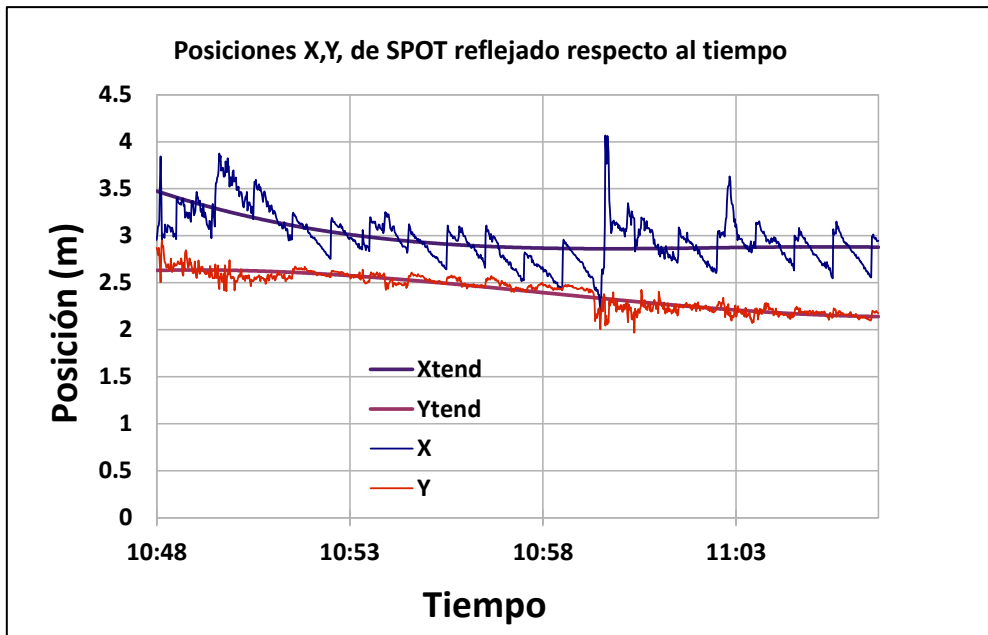
Figure 42. Horizontal and vertical positions of the reflected spot centroid as a function of time, during the reflected spot test.

Table 2. Coefficients of the polynomials fitted to the drift curves.

	C_3	C_2	C_1	C_0
X	-4.8275e+01	1.6003e+03	-1.7686e+04	6.5155e+04
Y	3.4548e+01	-1.1380e+03	1.2494e+04	-4.5708e+04

Different from drift, which characterizes the global image displacement, are the oscillations around this main tendency of the curves observed in Figure 42. Such oscillations have several causes: wind forces, inertial mechanical oscillations, and the control strategy followed. In particular, a saw tooth structure is clearly observed, which is due to the periodic actualization of the motor position each minute. This latter effect induces typical oscillations of around 40 cm in the horizontal direction. In the vertical direction this was not noticeable during the test due to the short duration, which required very little movement in this direction.

The oscillation amplitude is characterized by the standard deviation of the data around the fitted curves presented in Figure 42 and Table 2. The horizontal and vertical values were 0.215m and 0.067m, respectively. Due to the camera pixel size, the maximum resolution in these measurements is 0.0175 m. At the considered distance, the horizontal oscillations translate into a tracking accuracy of 1.7 mrad.

During the reflected spot tests it is frequently not possible to observe the total backlash due to the small wind loads. For this reason a manual static test is carried out by pushing the heliostat from one side to the other and tacking pictures of the image reflected to the target (Figure 43). A gentle force is applied to avoid tensioning the structure. Only the horizontal

direction was evaluated, as the vertical effect does not manifest in normal operation due to intentional weight imbalance around the vertical rotation axis.
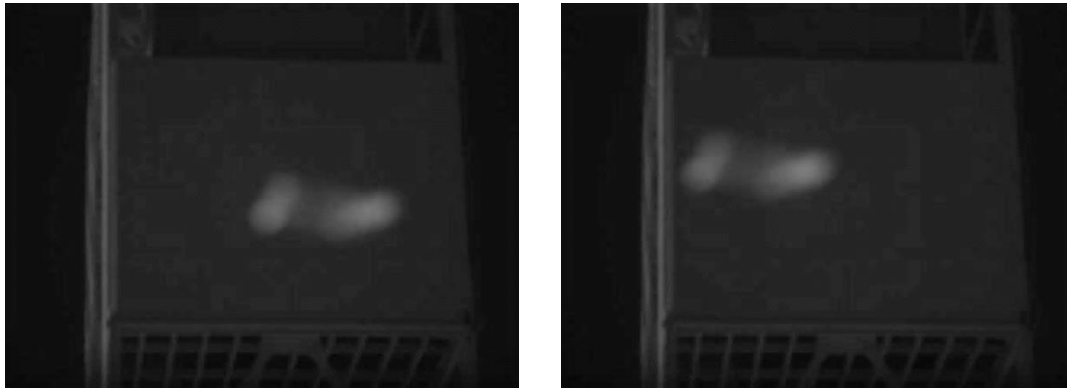

Figure 43. Images of the reflected spot test when the heliostat is manually pushed to both ends of its horizontal gear slack.

The evaluation requires the calculation of the global normal vector of the heliostat at each of the extreme positions. The angle between the horizontal projections of both normal vectors equals the global gear slack (backlash). In Table 3, the main parameters of the evaluation are presented, which gave a final value of 14 mrad.

Table 3. Parameters and results of the gear slack evaluation.

Hour	Centroid of the spot		Solar angles		Vector unitario normal helióstato		
	Horizontal (m)	Vertical (m)	Zenith (deg)	Azimuth (deg)	x (West)	y (South)	z (vertical)
09:24:35 a.m.	-1.332	21.867	46.962	-77.420	-0.472	0.704	0.531
09:25:31 a.m.	0.915	20.900	46.766	-77.267	-0.462	0.710	0.531

Unit normal vector		BACKLASH	
x (west)	y (south)	(Horizontal angle between normal vectors)	
-0.557	0.831	(rad)	(deg)
-0.545	0.839	0.01423	0.81535

The fringe reflection test was carried out with the heliostat at a 201m line of sight distance from the target. Fringe patterns with spatial frequency of 1.5 fringes per meter were projected

on the tower Lambertian target. In Figure 44 a horizontal pattern projected on the target is shown. In Figure 45 the reflection of horizontal and vertical patterns by the heliostat are presented. Large distortions can be appreciated in both directions, which clearly indicate the deviations of the facet surface from an ideal plane.
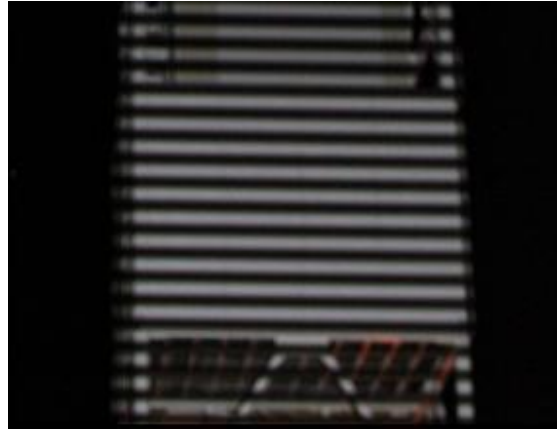
Figure 44. Fringe pattern projected in the Lambertian target.
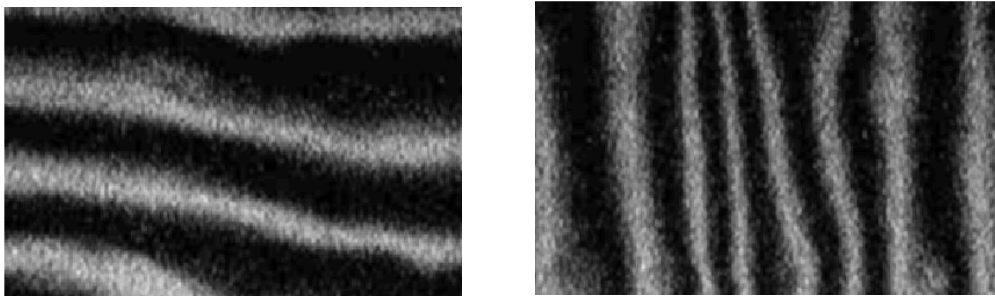
Figure 45. Fringe patterns reflected by the heliostat.

By means of the algorithms implemented in Matlab for the analysis of the fringe patterns, the obtained images where processed, and maps of the local slopes on the mirror for both perpendicular directions were obtained (Figure 46). Such slopes represent the deviations of the surface with respect to a plane.
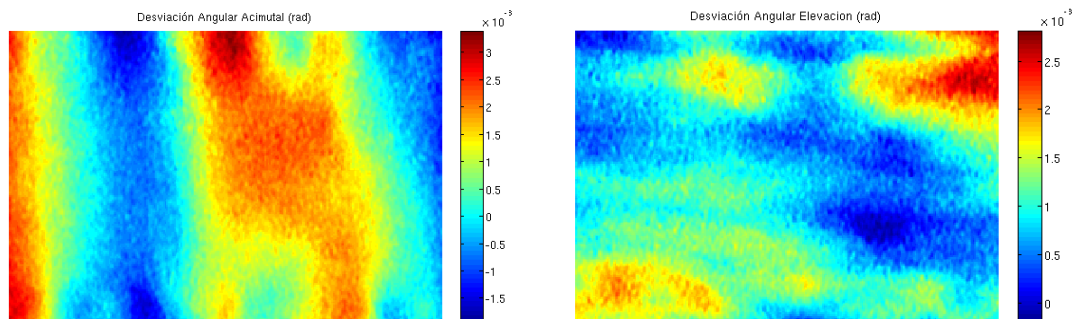
Figure 46. Maps of horizontal (left) and vertical (right) angular deviations on the heliostat surface.

The obtained values for the standard deviation of the slope in the horizontal and vertical directions where, respectively, $\sigma_{slope,h}$=2.41 mrad y $\sigma_{slope,v}$=2.18 mrad. These are large values, if one considers that such slope variations produce reflected ray deviations of twice their values.

With regards to the operational tests (see Section 1.4), not all of them were applicable to the heliostat:

Local control:

This test is only partially applicable, as the heliostat has only a local control system, operated by direct connection to a lap-top, with only the normal tracking operations defined. This tracking operates correctly as described previously. No reference search or security position are implemented.

Local control under error conditions:

Error conditions are not implemented in the local control, as autonomous operation has not yet been developed for this heliostat.

Focusing quality:

As described in the previous test, a tracking accuracy of 1.7 mrad was found, under low wind conditions (20 km/h); however, a backlash of up to 14 mrad could be manifested when wind increases.

Intrinsic focusing quality:

The intrinsic focusing accuracy in this case is based on the optical error of 2.41 mrad.

Total power consumption:

This evaluation has not been carried out.

Wind load testing:

Under wind loads above 20 km/h, the accuracy reduces to 14 mrad.

3 State of the art of methodologies for heliostats optical characterization (CNRS)

3.1 Laser methods

3.1.1 Laser scanning

3.1.1.1 Introduction

Laser scanning technique for surface reconstruction can be divided into two categories: a) direct measurement and b) reflection techniques. The first methods use laser scanners to directly measure the surface geometry of the mirror and the second uses the reflection of a light beam to gain information about the surface normal. Depending on the application one or the other data or both (geometry and normal) are of interest.

3.1.1.2 Direct Measurements

Using laser scanners or laser radars the surface is reconstructed directly by evaluating the light reflected by the surface. This requires a very sensitive light detection system as the reflection of a mirror is mainly specular and only very little light is reflected back to the system where it is evaluated. If the system, however, is capable of doing so it can reconstruct the surface of the mirror with very high accuracy (~0.1 mm for distances up to 10 m [27]). The result is usually a dense point cloud representing the surface. To evaluate the quality of the mirror the surface normals have to be calculated from this data. This is generally done by locally fitting surface patches to the measured points and calculating the normals from these. However, in doing so the data is either smoothed or the measurement noise amplified.
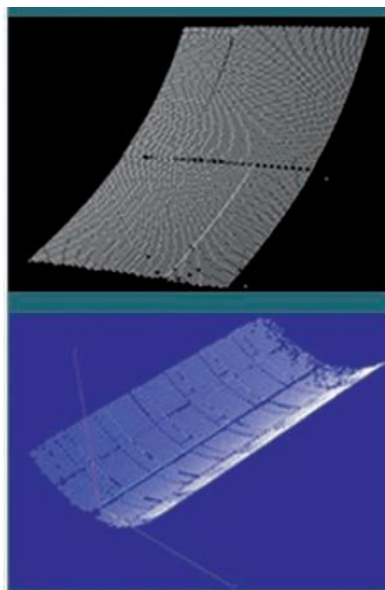

Figure 47. Surface Characterization of Concentrators CTAER.

Evaluating the surface quality of a 3 x 2 m2 facet with 4000 equally space points (~4 cm spacing) using a device capable of estimating the surface point with an accuracy of 0.1 mm, the resulting estimation error will be around 3 mrad. This is just a simple approximation, using a more points and more sophisticated surface interpolation methods, the error can be lower. However, it should be noted that achieving very high precision estimations with this technique is challenging. On the other side, if the surface geometry of the heliostat surface is of interest, for instance for orientation purposes this method is a very good solution.

3.1.1.3 Reflection based

Instead of directly measuring the surface of the mirror, the reflection of a laser beam is evaluated and compared to the expected direction. The reflection is directly influenced by the surface normal at that point, therefore, giving rise to the surface quality of the mirror. However, to calculate the surface normal the surface geometry and position is needed. To solve for this, the surface geometry is generally assumed to be a known shape and its position is iteratively fitted to the observations by a minimization approach. With the information about shape and position the surface normal can be calculated using simple reflection equations. The drawback of this method is that if the actual shape of the mirror surface is not sufficiently similar to the assumed shape a systematic error is introduced into the evaluation of the surface quality. Furthermore, as the reflections are evaluated, this technique is mostly used for strongly focusing mirrors, like dishes and parabolic troughs.

On the other hand, as the deviation between an ideally reflected ray and the observation increases with distance, this technique can achieve very high precision (~0.2 mrad [26]) with relatively simple setups. The most prominent example of such a technique is the VSHOT system explained below.

3.1.2 VSHOT - Video Scanning Hartmann Optical Testing

3.1.2.1 Introduction

This technique was developed to measure the surface quality of dish and parabolic trough reflectors [24]. It works by evaluating the reflection of a laser beam from the mirror and thereby calculating the surface normal at that point (see Figure 48).
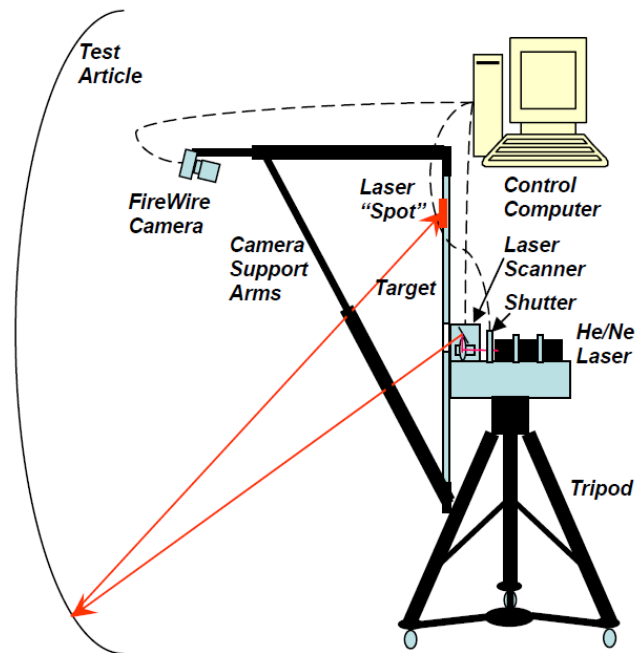
Figure 48. Video Scanning Hartmann Optical Testing [25].

The light of a point laser is reflected at the surface of the mirror onto a target. A camera mounted in front of the target detects this reflection. The distance between laser and surface is twice the focal length of the concentrator. With the known direction of the laser beam and the position of the target surface, it is possible to calculate the surface normal of the mirror at this point. Using a pair of small rotating mirrors it is possible to steer the direction of the laser to cover the entire surface of the mirror and, therefore, estimate the surface quality of the mirror surface. However, as only one surface point is recovered per capture, a compromise between the point density and time is required.

3.1.2.2 Set-up

The system consists of steerable laser (light direction can be controlled), a camera and a target. All components have to be set up in a controlled manner, i.e. position and orientation with respect to each other have to be calibrated. For the laser this means to calibrate the direction of the ray, which is required to be precisely in the desired direction.
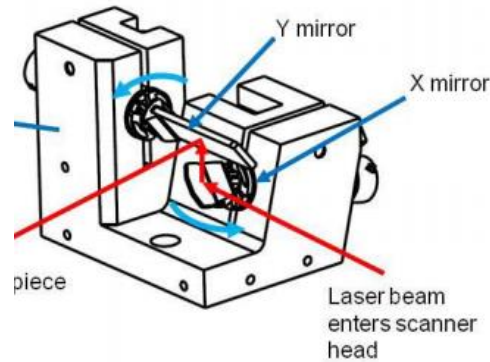
Figure 49. Steerable laser source using two mirrors [26].

In the described setup the laser is sitting in the center of the target and projects its light through a small hole. The camera is sitting in front of the target observing the targets surface. To map between camera coordinates and actual target metrical position the position and orientation of the camera is estimated by a calibration process. It is recommended that mirrors be positioned on the optical axis of the VSHOT, at a distance near the radius of curvature to achieve the most accurate results.

3.1.2.3 Surface estimation

As seen in Figure 48 each position gives rise to information about the surface normal at each point. However, it should be noted that the normal itself cannot directly be calculated from this, as its value also depends on the distance of the surface with respect to the target and light source, i.e. a change in distance in combination with a different normal lead to the same reflection. To solve for these ambiguities a post processing is required, which is done by calculating the least square surface approximation of the mirror geometry.

The surface is assumed to be in an ideal shape, i.e. for parabolic troughs a polynomial representing a parabolic shape is used. The optimization is then performed in an iterative way by starting with an initial value for the surface geometry and position and comparing the value of the ideal reflected light point with the observed one. The polynomial is the successively changed until a minimum error is achieved. This usually means that the error between the observed and ideal reflection has a mean value of zero. With the so achieved polynomial representation of the surface geometry the surface normal error can then be calculated using basic mathematical equations for light reflection.

3.1.2.4 Results

In [26] Gray et al. describe an uncertainty analysis of this technique for parabolic troughs, concluding that the expected error is around 0.3 mrad. One thing to note, however, is that the error is not evenly distributed along the mirror surface (see Figure 50).
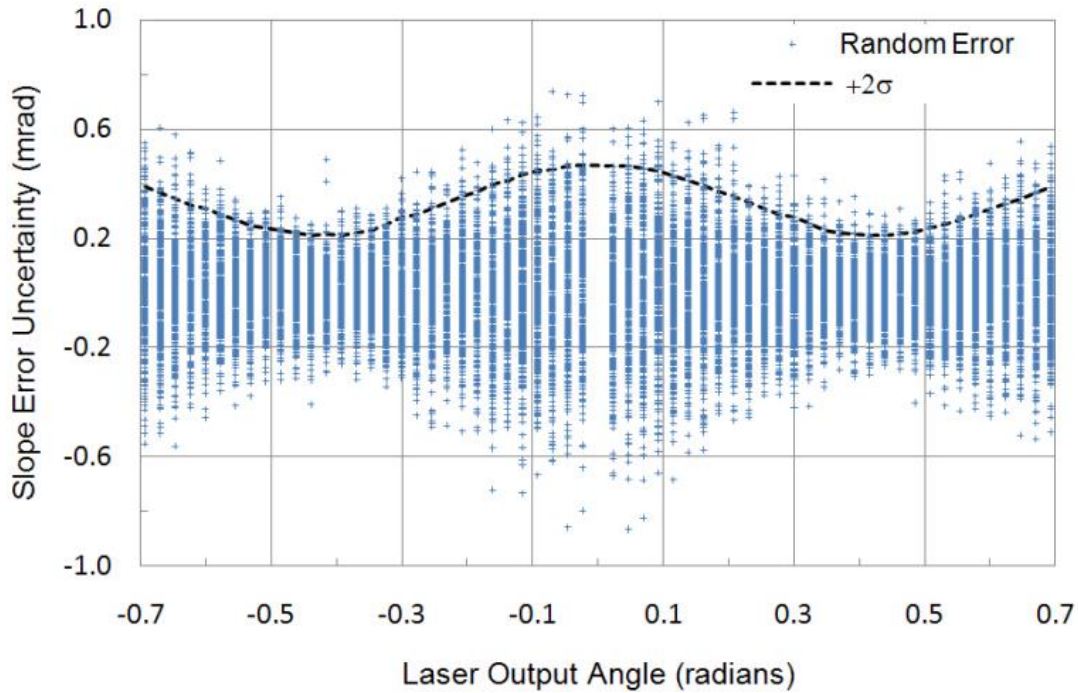
Figure 50. VSHOT slope estimation error varying with surface position [26].

Depending on the direction of the ray, the error varies between 0.2 and 0.45 mrad.

In another study [28], a detailed analysis of the accuracy of the VSHOT method has been achieved. The conclusions were that with better quality device, it is possible to obtain a 0.2% error in focal length with a repeatability of ±0.02% and 0.1 mrad in RMS slope error.

3.1.2.5   Conclusions

Table 4: Comparison between the laser methods.

	Direct measurements	VSHOT
Main advantages		> Can directly measure the surface normal
		> Can achieve high precision (~0.2 mrad) with simple setups
		> Does not suffer from the problems of insufficient illumination encountered in fringe projection techniques for instance
Main drawbacks	> It is difficult to obtain accurate results (~3 mrad with a device with an accuracy of 0.1 mm)	> If the actual shape of the mirror surface is not sufficiently similar to the assumed shape, a systematic error is introduced into the evaluation of the surface quality
		> The scanning task can be time-consuming

Although the system has been developed primarily for dishes and parabolic troughs the basic idea could be extended to heliostats. Mounting a steerable point laser onto the tower and using

a lambertian target it should be possible to automatically reconstruct the surface quality of the heliostats facet by facet. However, in this way the approach suffers from being a point wise, i.e. one point per capture, reconstruction method, as only one point of one heliostat can be measured each time. On the other side, by using a laser, it does not suffer from the problems of insufficient illumination encountered in fringe projection techniques.

An extension of this technique is to make a vertical and horizontal sweeps with a line laser, thereby, significantly reducing the required time for a reconstruction.

3.2 Photogrammetry

3.2.1 Introduction

The formal definition of photogrammetry is the art, science, and technology of obtaining reliable information about physical objects and the environment through the process of recording, measuring, and interpreting photographic images and patterns of electromagnetic radiant energy and other phenomena.

Photogrammetry is a metrology technique in which the shape, size and position of objects are determined from cross-domain fusion of measurements made on two-dimensional images. It can also be classified as a passive triangulation principle, where three dimensional coordinates of points of interest are calculated via triangulation from two or more images taken from different locations.

The use of photogrammetric methods has been a current topic for several decades already, for example, photogrammetry is the science behind the creation of almost every topographic map made since the 1930s. Theoretical photogrammetric methods have been known for more than a hundred years, in the last thirty years the main research has been focused on digital photographs and methods of image processing for obtaining the photogrammetric information.

3.2.2 Close Range Photogrammetry

Photogrammetry techniques can be classified as follows:

Aerial or Far-range photogrammetry (areas of m^2, more than 300 m object-to-camera distance) is used to produce topographical maps, to reconstruct the shape of buildings, and so on. (300 m, safe flying height above populated areas, as required by the FAA).

Close-range and very close-range techniques are preferred for the industrial applications technique. In this case the dimensions of the physical object and of its features can vary between few meters and 1 mm^2.

Close-range photogrammetry (CRP) is using to generate the three-dimensional coordinates of a point in object space. In a typical multi-station photogrammetry network there may be several images and many redundant observations. This leads to an over determined system of

equations that is most often solved by least squares estimation, as was commented above, theoretical photogrammetric methods have been known for more than a hundred years . In the mid1950s, other solution method was developed in which the point coordinates and exterior orientation parameters were determined simultaneously. This solution is known as bundle adjustment.
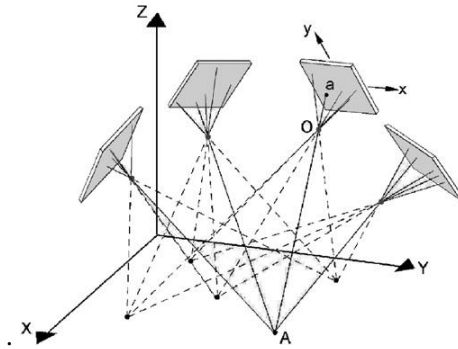

Figure 51. Close range photogrammetry principle.

In the mid-1980s the photogrammetric methods are becoming economically and technically efficient for industrial use. The first breakthrough in automated and high accurate 3D measurements [30] was based on analogue large format "Reseau" cameras, convergent multi-image configurations, digital comparators and digital image processing of the scanned imagery. This close range photogrammetry configuration offered the potential of measurement precision to 1:500,000 with respect to the largest object dimension.

The BLM's national centre in Denver has used close-range photogrammetric techniques to document resources since the late 1980s. At that time, although producing high-quality results, the close-range photogrammetric process could be tedious and time-consuming mainly because of the need to apply traditional techniques, workflow, and equipment to close-range image capture and processing.

The availability of video and digital cameras in combination with direct access to the digital image data generated new concepts for CRP applications. So called off-line photogrammetry systems utilizing high-resolution digital SLR cameras with usually wide angle lenses, retro-reflective object targets and sub-pixel image point measurement operators afforded object measurement within minutes by robust bundle adjustment, including self-calibration e.g. [31] [32].

The principles of these systems are well known [33] and they have gained widespread acceptance for industrial measurement applications [34]. Initially digital photogrammetric equipment and techniques were not sophisticated enough to match the accuracy attainable through the use of other metrology systems such as CMM, theodolites, laser trackers and more traditional film-based photogrammetry systems [35]. Fortunately developments in large area CCD sensors and target image location algorithms have pushed the accuracy attainable using digital photogrammetry to a level where it can comfortably challenge these systems. [36][37].

High-resolution digital cameras are readily available and represent a significant improvement over earlier generations of CCD cameras. Furthermore, recent advances in commercially available and cost-effective three-dimensional measuring and modeling (3DMM) software, and high- performance laptop computers have revolutionized the CRP process. With these advances photogrammetric measurement systems (such as GSI, AICON, GOM) are practically fully automated to such a level that even a non-specialized worker is able to carry out such measurements. Some companies have developed special photogrammetric cameras with integrated processing capabilities, so called intelligent cameras.

In a modern vision metrology system for industrial measurement, object space positional accuracies surpassing 1:100,000 of the principal dimension of the object are now routinely attainable with large-area CCD cameras and photogrammetric data processing.
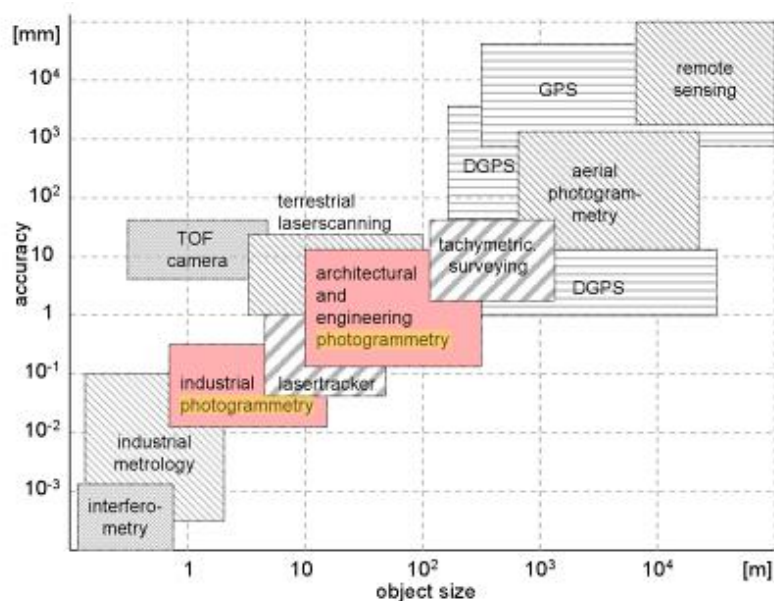

Figure 52. Accuracy of different metrology systems.

The CRP systems can be divided in five different groups:

Offline systems are the most flexible and portable photogrammetry systems for industrial measurements. They follow the classical photogrammetric procedure of targeting, image acquisition, image processing and coordinate estimation. Due to the time offset between image acquisition and availability of results and the fact that usually the camera is not connected to the processing computer, these systems are called offline. The precision of image point measurement can be as high as 1/50 of a pixel, yielding typical measurement precision (RMS 1-sigma) on the object in the range of 1:100,000 to 1:200,000, the former corresponding to 0.1 mm for an object of 10 m size [38]. The absolute accuracy of length measurements is generally 2–3 times less (e.g. about 0.05 mm for a 2 m object) than the precision of object point coordinates, which expresses the relative accuracy of 3D shape reconstruction [39].

Online systems, where the cameras are directly connected to the computer and the results are available immediately after the measurement. In a combination with probing devices these

systems are a kind of symbiosis between optical and tactile measurements. If the frequency of the measurement corresponds to the frequency of change or movement of the part, these systems are called real-time systems. Both types of systems are designed for pointwise measurement of parts.

Typically, an on-line system consists of two or more calibrated and oriented cameras that observe a specific volume. Appropriate object targeting affords fully automated feature extraction in image space. 3D information about points, contours or surfaces is directly generated in order to control a connected process, such as on a production line or for the positioning of an object with respect to an external reference frame.
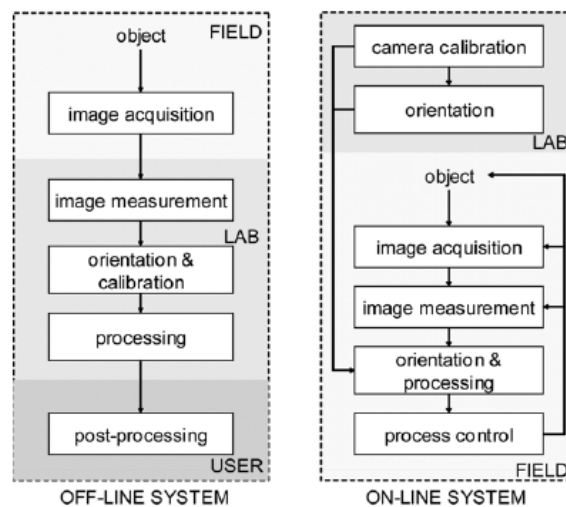

Figure 53. Off line and On line work flow.

The accuracy of on-line systems is usually less than that of off-line systems due to the limited number of images, restrictions resulting in less than optimal camera calibration and orientation, and the manual operation of probes. Typical accuracy figures lie in the order of 0.2–0.5 mm over a range of 2 m[40].

Scanning systems are able to acquire dense surface data: The first three groups are all universal, very flexible and mobile systems to be used in a wide range of applications. White-light surface scanners like the Steinbichler Comet or the ATOS system from GOM use an active fringe projection in combination with one or two cameras. They are not exactly photogrammetric systems, but use mainly photogrammetric principles for camera setup and calibration. The systems are able to deliver dense point clouds, but are limited in field of view. The evaluation procedure is usually a combination of coded light technologies and phase shifting methods. For the measurement of larger objects several patches can be stitched together by a cloud matching procedure or a through a network of references points, usually created with an offline photogrammetry system.

Dedicated systems are adapted for the measurements of special parts or products. Usually they allow online measurements and are integrated in a production environment. These systems allow for highest automation and ease of use.

Hybrid Systems, Photogrammetric sensors can be combined with additional measuring systems, as seen in fringe projection systems, laser tracking or scanning systems, tacheometers or 3D cameras. Most important are hybrid systems where the advantages of two sensor types are combined in order to form a new type of measuring system with extended functionality or performance. Examples are laser trackers equipped with a photogrammetric camera for 6DOF measurements at the object surface, offered for example by Leica, and the optical 3D navigation of a surface sensor through tracking with a stereo or multiple camera system, as offered by Steinbichler.

For example, TRITOP photogrammetric system has being developed by the German company GOM GmbH and published in 2012. The TRITOP system consists of one DSLR camera, contrast coded and uncoded points, robot, scale bars and appropriate software. The program contains the robot measurement positions, definition of the adapters that determine the co-ordinate system and adapters that define the centers of the measured holes.
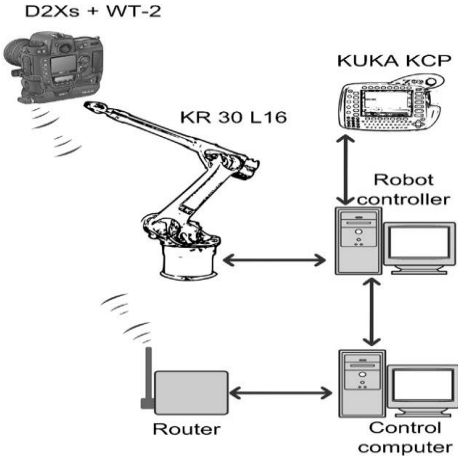
Figure 54. TriTop system.

3D coordinate measurement based on inverse photogrammetry and fringe Analysis [30] is a novel optical coordinate measuring method based on inverse photogrammetry and Fourier fringe analysis. Measurement system mainly consists of a micro-camera connected a measuring rod with a probe and a liquid crystal displays screen. In the measurement process, the probe contacts the surface of the measured object, and the CCD camera captures the stripes image on displays screen. The coordinates of camera principal point in the world coordinate system may be determined by the phase information that the fringe pattern carries.
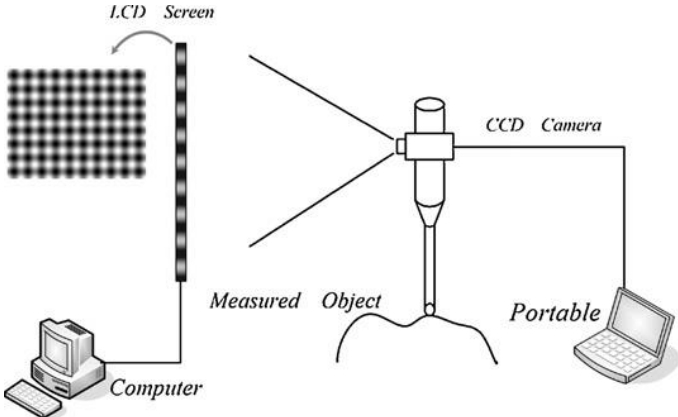
Figure 55. Inverse photogrammetry and fringe Analysis.

3.2.3 Technical issues

The successful photogrammetry use requires a number of technical components that form an efficient system. The following list summarizes these components and related technical issues:

- Network.
- Imaging sensor.
- Targeting and illumination.
- Image processing.
- 3D reconstruction.
- Imaging configuration.
- Verification of accuracy.
- Software and algorithms.

3.2.3.1 Network

The most significant are the geometric strength of the network and the level of redundant measurements in the network. Each 3D reconstruction model has different levels of requirements for the networks. It could be enough with only one or two images or conversely more than hundred.

3.2.3.2 Imaging Sensor

Resolution (number of pixels), available lenses, acquisition and data transfer speed, camera stability, synchronization, data compression, etc. are very influential in CRP.

The selection of the appropriate sensor device is driven by requirements in accuracy, resolution, acquisition speed and frame rate, synchronisation, amount of data, spectral information, field of view, image scale, digital interfaces and cost. In general, it is desirable to use cameras with the highest resolution, imaging speed and accuracy in order to provide maximum efficiency and productivity with respect to system costs and return on investment. Nowadays the range of available cameras and imaging sensors is huge. Based on CCD and CMOS technology, sensors are available with very high resolutions (>60 Mpixel), very high frame rates (>2000 Hz), pixel sizes varying between about 1.4 and 15 μm, and different sensor formats [41][42][43].

High-resolution digital SLR cameras are now available with sensors between 10 and 60 Mpixel and image formats between approximately 20 × 14 mm and 54 × 45 mm. Such cameras are designed for (semi-) professional photographic work with a range of exchangeable lenses, high-capacity storage devices and powerful batteries. Their mechanical stability is usually poor in terms of high-accuracy photogrammetric requirements, and camera calibration is therefore an important step in the complete process chain [44]. SLR cameras are mainly used for off-line applications, i.e. the measurement of static objects. Suitable cameras

in classical small format (35mmSLR) are offered by companies such as Nikon, Canon and Sony, whereas medium-format cameras are available from Rollei, Hasselblad or Alpa, these being usually equipped with CCD sensor backs by PhaseOne or Leaf.

Dynamic processes can be observed by digital cameras with higher frame rates, e.g. video cameras or high-speed cameras Controlled through a fast computer interface (e.g. CameraLink or Giga Ethernet), sensors with more than 1500×1000 pixels and frame rates of 2000 Hz are commercially available, conferring the opportunity to carry out dynamic photogrammetry of high speed events. Video cameras with typically 1.3 Mpixel sensors and frame rates of 10–30 Hz are used in a variety of applications of photogrammetric on-line systems, examples being tube inspection [66], stereo navigation and robot guidance. Digital high speed cameras are usually equipped with CMOS sensors that enable fast data access, programmable field of view, extremely short exposure times and high dynamic range. Typical high-speed cameras provide images of about 1500×1000 pixels at 1000 Hz, though there are already on the market newly developed cameras with similar spatial resolutions, but with frame rates of more than 2000 Hz.

There are very few cameras specifically designed for close range photogrammetric applications. The classical 'metric camera' approach with stable interior orientation requires high additional effort in terms of optical and mechanical sensor design. The main advantage of these cameras is their assured stability and the consequent reduced need for periodic or on-the-job calibration, for example in applications where high accuracy is demanded without the technical possibility for simultaneous camera calibration.

However, the term 'metric camera' should only be used in conjunction with the desired accuracy level of the camera. Consequently, even metric cameras have to be calibrated on the job if the desired accuracy exceeds the metric tolerance of the camera. The measurement of targets is performed inside the camera processor.

3.2.3.3   Targeting and Illumination

Representation of interesting object features, target shape and size, wave length of light sources, restrictions to object access, illumination power and measurement volume is contemplated in this section.

It could be possible to implement an algorithm that looks for interesting points in the image or selecting these points in a manual way, but it is very common to use targets to indicate which points are useful. In general, there are two types of targets, retroreflective and projected.

Retroreflective targets have been in use for industrial photogrammetry for many years. The resulting quasi-binary images allow for a good separation of target and background. Also the complete illumination is controlled which makes that the image acquisition is much more independent from individual camera settings. Another reason was the shorter search and measurement time in the quasibinary digital images, but with the current processing power this has less importance. Plain paper targets can be used without noticeable loss of performance.

The next and maybe most important step towards automation was the invention of coded targets. The first coded targets were introduced by AICON in 1991 [45].

These targets have a unique identifier either in form of a ring code or a geometric target pattern. Each point is detected, measured and labelled automatically by the software. Probing devices combine optical and tactile measurement techniques. The same principle is used for hidden point adapters.

Some applications use projected targets like dot or grid patterns.
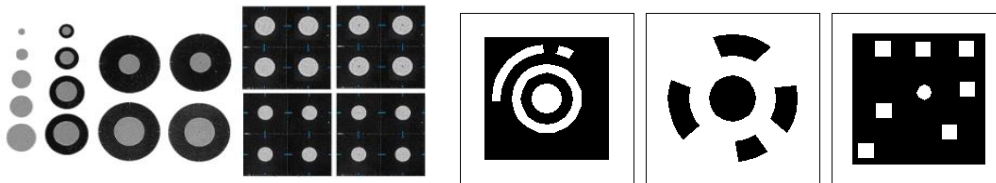
Figure 56. Retro-reflective targets (Coded targets preferred, circular targets, hard-body tooling targets).

Figure 57. Projected pattern.

A comparative review was carried out between retro reflective and projected targets [68][75]. The case studies highlight some of the advantages of a target projection system. The ability of the system to quickly and accurately map dots onto a surface makes it ideal for many applications that have traditionally shunned photogrammetry due to the inconvenience of targeting.

The review concludes that projected targets are fast, more density targets, versatile, and accurate. No consideration has been given to the associated project hardware cost of the projection system but it is evident that the system would recover its cost within the context of a modest measurement program.

The non-contact nature of the system makes it well suited to applications where the object is too hot or perhaps too fragile to handle. The development of the target projection system is likely to have a substantial influence on surface measurement using photogrammetry.
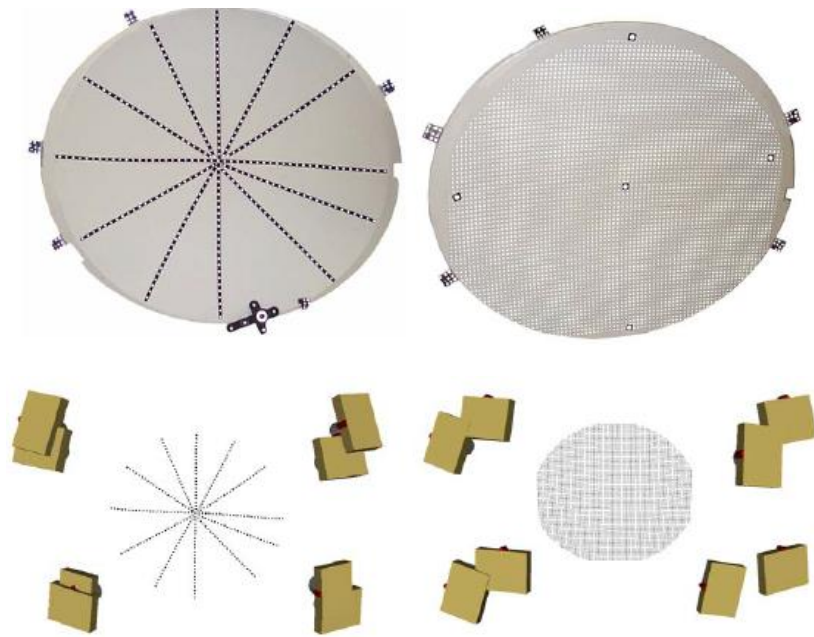
Figure 58. Ganci and Brown comparative system.

3.2.3.4 Image Processing

It can be understood that to accurately reconstruct the 3D information and orient the images, extracting the exact image locations of the targets and robustly establishing the correspondences of them are firstly needed. They are the only input of the whole 3D reconstruction on which the accuracy depends.

Target image location algorithms such as the weighted centroid have theoretical accuracies of approximately 1-2% of the image pixel size and have been utilized in many videometric applications.

In many practical cases the dimensions or structure of the object require more than one measurement position of the surface sensor system. Hence, the exterior orientation of the measurement system with respect to a global coordinate system must be solved for each single measurement setup, or for each local point cloud.

This task can be solved using different approaches:

- Optical sensor navigation by an external photogrammetric system.
- Mechanical sensor navigation by robot or articulated arm.
- Photogrammetric orientation by means of control or tie points.
- Point cloud matching by iterative closest point (ICP) or equivalent methods.

If the tracking device is used at different stations, the measurement volume is almost unlimited. By contrast, mechanical orientation devices such as CMMs, robots or articulated arms have limited working areas and restricted mobility. Their advantage is the independence of light conditions. Compared to laser tracking or optical tracking, mechanical devices are most advantageous in small volumes of usually less than 1 m3.

Hand-held sensors can also be navigated by tie or control points that are located on the object surface. In case of the HandyScan system from Creaform, shown along with a second system oriented by control points, two cameras are used to observe targets in 3D space while a laser system is used to scan the surface. The system can be used for large objects if the distribution and accuracy of object points is sufficient. In this case the object targets are measured by a high-resolution photogrammetric off-line system and subsequently used as known control points. The concept is also able to work with unknown tie points, however with generally poor conditions for error propagation. Image-based 3D surface measurement systems can also employ exterior orientation determination by mechanical means, as exemplified by the two systems.

The registration (orientation) of single 3D point clouds using surface features can be performed via the ICP algorithm, the applicability of the method depending strongly upon the surface structure which must provide sufficient points, corners or other features that can be matched with respect to adjacent point clouds

In special cases the photogrammetric measurement of object structures such as edges or contours is desired. If these structures cannot be derived from discrete 3D points, they have to be extracted from image edges or contours. The measurement of regular geometric elements such as circles, spheres or cylinders based on grey-level edges is enabled by the so-called contour method of Andresen. Usually three images from different positions are required to determine the element parameters in 3D space, namely the position, normal vector and radius of a circle. The method assumes that the physical object edge and the optical edge in the image are identical.

3.2.3.5   3D Reconstruction

The methods for determination of 3D coordinates, (e.g. spatial intersection, least square method, bundle adjustment, stereo triangulation) and error statistics, number of camera stations is allocated in this section.

There are a lot of mathematical camera models most based on the collinearity equations. The linear pinhole camera model shown in Figure 87. Reconstructed slopes and shape error of the heliostat for A = H = 100 mrad.

, where coded and un-coded points are placed on or around an object. Photos of the object are taken from different orientations. After image processing, point clouds of the object are matched and reconstructed, and the distances between arbitrary two marker points can be determined precisely. For any point P in 3D space, if the 2D coordinates of P in any other two photos are known, the 3D coordinates of $P(X, Y, Z)$ can be calculated by next equation.
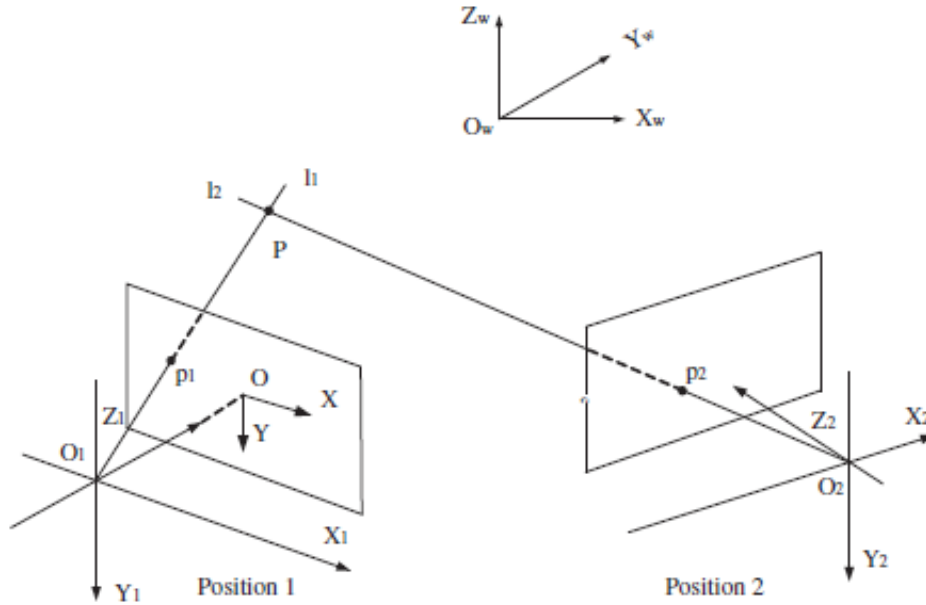
Figure 59. Reference systems in CRP.

$$\begin{bmatrix} a_{11} - u_1 a_{31} & a_{12} - u_1 a_{32} & a_{13} - u_1 a_{33} \\ a_{21} - v_1 a_{31} & a_{22} - v_1 a_{32} & a_{23} - v_1 a_{33} \\ b_{11} - u_2 b_{31} & b_{12} - u_2 b_{32} & b_{13} - u_2 b_{33} \\ b_{21} - v_2 b_{31} & b_{22} - v_2 b_{32} & b_{23} - v_2 b_{33} \end{bmatrix} \begin{bmatrix} X \\ Y \\ Z \end{bmatrix} = \begin{bmatrix} u_1 a_{34} - a_{14} \\ v_1 a_{34} - a_{24} \\ u_2 a_{34} - b_{14} \\ v_2 a_{34} - b_{24} \end{bmatrix}$$

Where $u1, v1$ are the 2D coordinate in pixel of the point mi in left image; $u2, v2$ is the 2D coordinate in pixel of the point $m'i$ in right image; $\begin{bmatrix} X \\ Y \\ Z \end{bmatrix}$ is the 3D coordinate of the object spatial point. From this approach, one of the many methods exist to solve it is used bundle adjustment. There are other methods such as least minimum square, least mean square, SIMULTANEOUS LEAST SQUARES ADJUSTMENTS, SEPARATE LSE.

The linear pinhole camera model described above is only an approximation of the real camera projection. It is not valid when high-precision 3D reconstruction is required. Various sources of lens distortions, radial, decentring and thin prism distortions should be incorporated in a more sophisticated camera model or in a later calibration method.

The purpose of *3D reconstruction* is to eliminate discrepancies caused by redundant observations, estimate the probable values and evaluate the qualities *(e.* g. accuracy and reliability) of the coordinates of the object points and the orientation elements of the photographs. In recent years, photogrammetric adjustment has made a great progress on aspects of compensating systematic errors, introducing non-photogrammetric information, detecting blunders and reliability theory, etc. There are a lot of methods of 3D reconstruction, it depends of the characteristics of the system.

3.2.3.6 Imaging Configuration

Imaging configuration can be refuge self-calibration ability, datum definition and object control, self-control of orientation and calibration.

Camera calibration has always been an important issue in computer vision. It consists of finding the mapping between the 3D space and the camera plane. This mapping can be separated into two set of transformations. The first one involves the location of the camera in the scene and it is described by the extrinsic parameters of the camera model. The second one is the mapping of the 3D points in the scene to the 2D coordinates in the image. This mapping is modelled by the intrinsic parameters which give the geometry of the camera and the optical features of the sensor.

Camera lens distortion was first introduced by Conrady [46] with the decentring lens distortion. Afterwards Brown proposed, [47]the radial, decentring and prism distortion model which has been widely used. Some modifications to this model have been reported focused on mathematical treatment of the initial model, or from a conceptual point of view, without any quantitative evaluation. Recently, a non-parametric model for camera distortion has been proposed by [48] which only considers the radial distortion. Although the radial component of lens distortion is predominant, it is coupled with the tangential component and therefore it should be taken into account.

In fact, the basic formula which represents the conventional model of lens distortion is a sum of three terms corresponding to the radial, decentring and thin prism components.

Up to now, a variety of methods for camera calibration have been developed to accommodate various applications [49][50][51][52][53][54](to cite a few). One family of pin-hole calibration methods resolves the camera model using metric information of a 3D, 2D, 1D template. The other family does not use any metric information from the scene in what is called self-calibration methods. The problem of self-calibration is that if all camera parameters are unknown, it is very unstable. In these cases, known camera motion helps in getting more stable and accurate results [55][56], but it is not always easy to get ''pure camera rotation''. Better results are always computed with metric calibration methods.

Referring to the computed camera models, some only compute the pin-hole model parameters, and others solve the pin-hole model together with the distortion parameters. Since the distortion is most often coupled with the internal and external camera parameters, methods which extend the calibration of the pin-hole model to obtain the camera distortion parameters result in high errors on the internal parameters. Therefore, it is necessary to use a different method to estimate the camera distortion model apart from the pin-hole model. Furthermore, if distortion parameters are known before, it allows correcting observed positions of points in the image, achieving quasi-ideal camera behaviour similar to the pin-hole model and the camera can be calibrated accurately. To compute the camera distortion model only, several methods have been proposed which do not rely on any knowledge of the scene points, nor do they need calibration objects or any known structure. They are called non-metric calibration or self-calibration methods. These methods use geometric invariants of some image features like straight lines, vanishing points or the image of a sphere. Methods rely on the fact that

straight lines in the scene must always be perspective projected on straight lines in the image. In addition, [57] use the minimum vanishing point dispersion constraint between three mutually orthogonal sets of parallel lines to recover the distortion parameters. In this case, the inconvenience of the method is to find triplets of orthogonal lines. Other methods use correspondences between points in different images from multiple views to compute camera distortion parameters. They are not easy to solve and are likely to produce some false data to the distortion algorithm.

Ricolfe-Viala [87] proposes a metric method for lens distortion calibration. Since metric information of the scene is going to be used in the pin-hole calibration process. His propose is using this information prior to calibrating the lens distortion. In this way, the camera calibration should be understand as a two-step procedure where first the camera lens distortion is computed and corrected and second, the pin-hole camera model is calibrated.
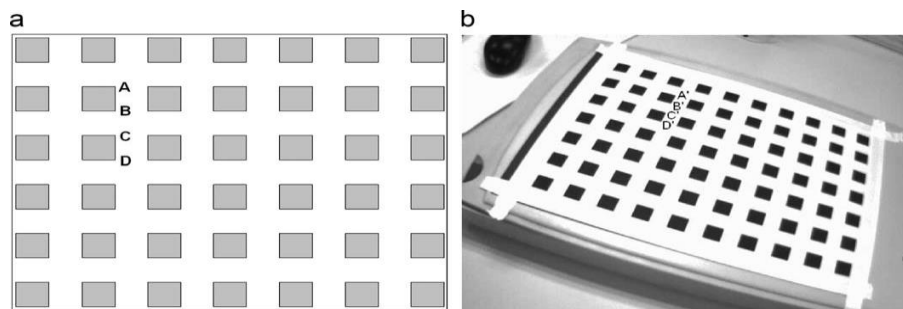

Figure 60. Ricolfe-Viala calibration pattern.

Camera calibration for off-line systems is based on a multiimage setup that is recorded either for a test field (test field calibration) or for the measured object itself (on-the-job calibration). In both cases a minimum number of tie points must be provided and these can be natural or signalised points. Optionally, given control points or distance constraints can be introduced. The datum of the object coordinate system can either be defined by three or more control points (with the risk of introducing shape constraints in the photogrammetric orientation), by minimum definition or by free-net adjustment.

If the mechanical instability of the camera is worse than the required accuracy level, the camera can be calibrated image-wise, i.e. each image of the bundle configuration obtains individual calibration parameters [58][59].

Usually the distortion values are kept constant for all images in the network, while the position of perspective centre is adjusted for each image. This method leads to significant accuracy enhancements as long as the imaging configuration consists of enough well distributed images (usually more than 30 including images rolled around the optical axis).

The precision of camera calibration can be measured by the precision of image and object points, or by standard deviations of camera parameters. A reliable and strict accuracy assessment is only possible if checks can be made against independent control points or standardised calibrated distances. Typical internal precision measures for digital SLR camera self-calibration can reach1:100,000 and beyond (RMS 1-sigma accuracy vs. largest object

dimension), whereas accuracy values determined through length measurement are generally closer to the 1:50,000 level [61].

Camera calibration for on-line systems with fixed or limited camera positions can only be solved by multi-image bundle adjustment if a local test or reference object can be moved through the measurement volume. In this case an appropriate multi-image configuration can be recorded which is usable for self-calibration. In cases where an additional calibration body is not provided cameras have to be calibrated in advance. The successful use of the system then requires stable cameras with respect to the desired accuracy level. Use of an extended space resection approach with additional parameters for interior orientation may allow for a camera-wise calibration based on given 3D control points. However, the potential of self-calibration bundle adjustment cannot be matched by single image space resection.

Calibration of on-line systems with fixed camera set-up can be performed either by observing a calibration body which is located at different positions in object space, or by measuring an additional calibrated scale-bar that is moved in front of the cameras [58]. The latter method is easy to handle and provides scale information throughout the measurement volume, hence it is advantageous for accuracy assessments based on distance measurements.

3.2.3.7   Verification of Accuracy

The specified accuracy of an industrial measurement system and the achieved accuracy within a real project are two of the guidelines and standards exist, the definition of accuracy performance of photogrammetric systems is still very heterogeneous. Terms like 'precision', 'relative accuracy', 'accuracy', 'measurement uncertainty', 'length measuring error', 'standard deviation', 'RMS 1-sigma' and others exist, while only a few are defined according to international standards such as ISO 10360 or GUM,1993.

In many photogrammetric applications internal precision measures from adjustment results (e.g. sigma 0, standard deviations, RMS 1-sigma values) are presented as final accuracy figures. In these cases the performance of a system can easily be manipulated simply by increasing the number of observations. It can be argued that real accuracy measures can only be generated if independent control/checkpoint data is available in object space. This verification data can be formed by 3D control points, which, however, are often not available in practice with sufficient (higher) accuracy. For tactile probing systems (e.g. CMMs and hand-held probes), diverse reference bodies are available, including ball plates or reference scales. In general, these reference bodies are relatively small, expensive, heavy and not suited for optical probing. A rather simple way of providing calibrated and certified references is via the use of scale bars with target points that are equivalent to the type of targets used for the optical measurement system. Scale bars are very mobile, easy to calibrate and they enable traceability to national length standards.

For optical 3D point measuring systems the German guideline VDI 2634 [60] part 1 has been available for about 10 years, and this procedure for accuracy assessment for acceptance testing and accuracy performance verification is now well accepted in industry. Indeed, larger companies may often not employ measuring systems whose performance has not been verified with respect to VDI 2634. The main idea is to arrange a number of scale bars in

object space such that the principal coordinate axes are represented by a number of calibrated lengths. For the accuracy test, all photogrammetrically measured distances are compared to their calibrated nominal length. The results are presented in a diagram that easily shows the length measuring error (LME) as the largest distance deviation from all measurements. For all-around image configurations and bundle adjustment the resulting length measuring error can be estimated from RMS 1-sigma values of object points. Assuming equal RMS values in all directions and a confidence interval of 3 sigma, the estimated LME results to:

$$LME = \sqrt{18} \cdot RMS$$

For area-based probing systems, such as fringe projection devices, VDI 2634 part 2 and 3 recommend procedures for the assessment of probing errors, plane measuring errors and sphere distance errors. Usually calibrated spherical or plane reference bodies are applied for system testing. In general, the acquired 3D points are analysed with respect to a reference surface whereby 3d of the measured points can be neglected due to typical outliers. Since most of the systems operate in measurement volumes of less than 1 m3, the provision of suitable reference bodies is feasible [62].

3.2.3.8   Software and Algorithms

Beneath improvements in image measurements, which are also related to software. The important point in the software is an efficient user interface which is basically self-explanatory and intuitive to handle.

A major part of the software development is now the programming of post-processing functionalities like deformation analysis or geometry checks like roundness checks or CAD comparison.

3.2.4   CRP in Solar Systems Applications

There are a few works with CRP applicated to solar technologies, the most of them are related with cylinder parabolic concentrator technology.

One paper [63] shows the work carried out to determine the real shape and the intercept factor of a new prototype of parabolic solar collector. Convergent photogrammetry with off-the-shelf equipment was used to obtain a 3D point cloud that is simultaneously oriented in space and adjusted to a parabolic cylinder in order to calculate the deviations from the ideal shape. The normal vectors at each point in the adjusted surface are calculated and used to determine the intercept factor.

At the Plataforma Solar de Almería, a set of methods and algorithms based on close-range photogrammetry has been developed on the last years. These methods allow to evaluate the geometrical quality of solar concentrators. The application of these techniques to different concentrators prototypes, permits to determine their geometrical, optical and energy behaviour as well as to detect improvements on their design.
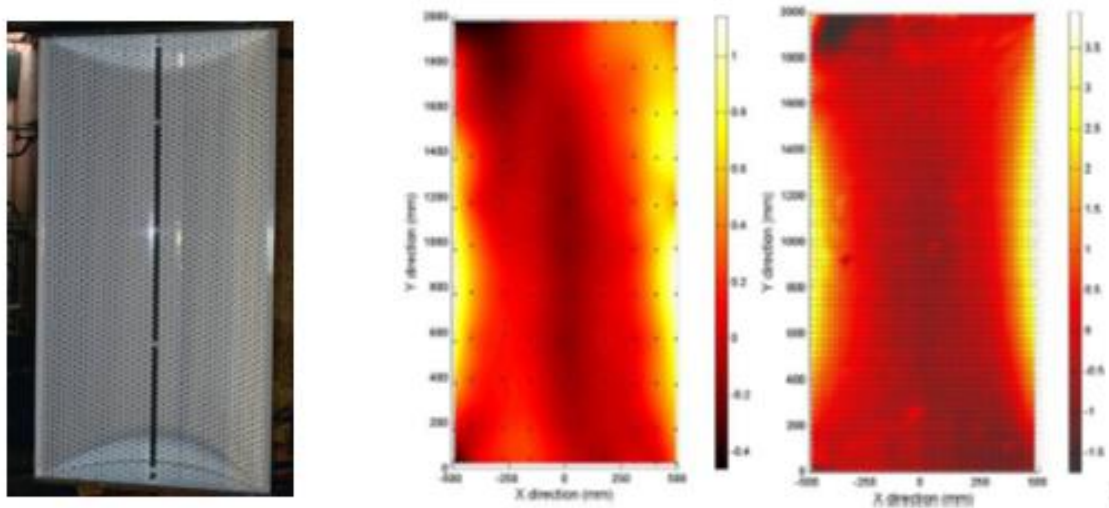
Figure 61. Small CCP with dot pattern and deviation graphics obtained in the PSA techniques.

Close-range photogrammetry has proved to be a suitable tool that supports the design and manufacturing improvement as well as quality control in solar concentrating systems. Using an adequate target pattern and taking a sufficient number of photographs with a conventional digital camera, it is possible to achieve accuracies up to 1:10000 / 1:60000 meaning pattern coordinate errors lower than 0.1 mm. This accuracy is high enough for solar concentrator's quality inspection as well as for determining their optical performance, where tolerances from 3 to 5 mm are required. This task has become essential on the evaluation of the different concentrators used nowadays on solar thermal systems [64].

Also, CTAER has developed different projects using CRP for the analysis of solar concentrators such as parabolic dish, parabolic trough and heliostats.
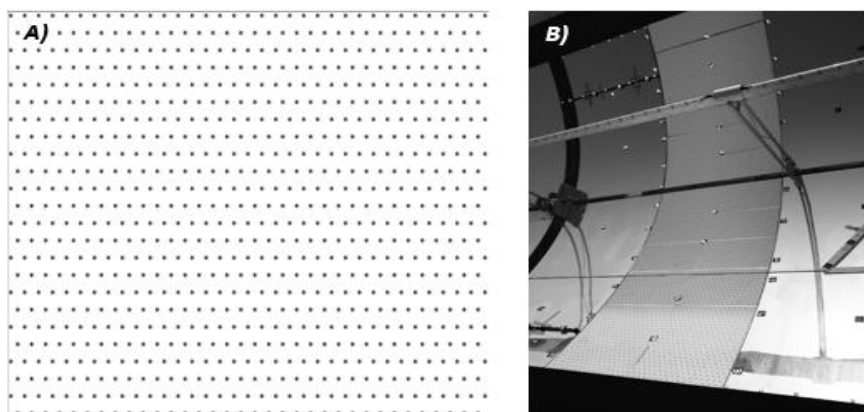

*Figure 62. (A) Dot pattern, (B) Parabolic trough collector ready to CRP.*
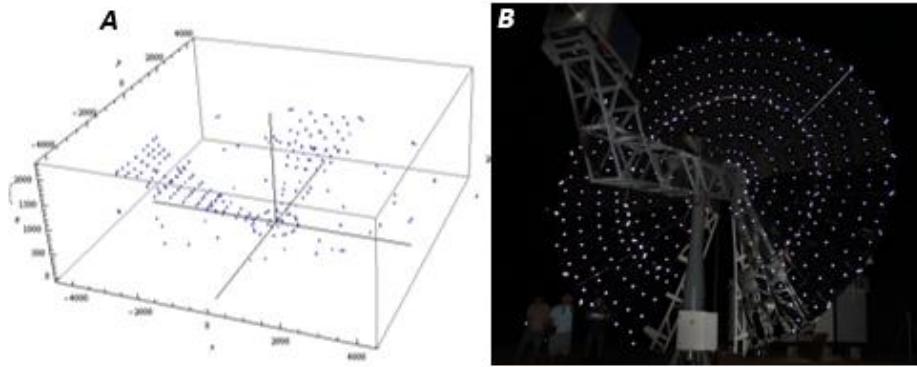
*Figure 63. (A) Cloud pint obtained through CRP, (B) Solar Dish ready to CRP.*
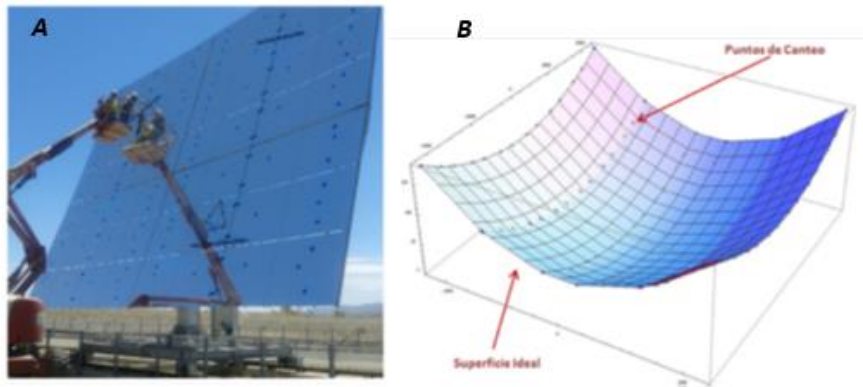
Figure 64. (A)CTAER´s members placing targets on heliomobile; (B) Surface generated by CRP.

3.2.5 Close Range Photogrammetry and other Systems

3.2.5.1 Comparison of CRP and Industrial Theodolite Systems

The modern digital photogrammetric system has succeeded a point where it can offer traditional users of triangulation systems a very attractive alternative. The case study examined in [77] is one example of how the digital photogrammetric is a strong alternative. This paper reports on the suitability of digital photogrammetry as an alternative measurement technique for applications that have traditionally been completed using theodolite triangulation.

The most significant conclusion is the obvious savings available both in terms of time and money, with the CRP system. Given that the accuracy achievable is commensurate with that of a theodolite triangulation system.

3.2.5.2 Laser-Scanning and close range photogrammetry

The use of 3D laser-scanners is becoming more and more popular for a wide range of purposes because of their high performance. The huge datasets produced by a laser-scanner

provide considerable possibilities for the modeling and visualization of objects. Although they deliver a point cloud with high density, the accuracy of individual points barely reaches one centimetre. To attain much higher accuracy, photogrammetric methods or optical scanning techniques can be used. Considering all advantages, each of these methods has its specific limitations.

While photogrammetry carries the potential to measure edges very accurately, the measurement of freely formed, surfaces that requires a high levels of resolution or point density and sparsely structured surfaces causes problems. On exactly those surfaces a laser-scanner works properly. However, precise determination of edges is not really possible here.

There is a paper [81] where described an approach to exploit the strengths of both sensor-types by combining the acquisition and evaluation of datasets. By combining the acquisition and evaluation of laser-scanner data and image data, results with a high richness of detail and accuracy are produced. This would not be possible if laser-scanning or close-range photogrammetry were applied separately. Small details visible and measurable in an image cannot be identified in the noisy point cloud. Also, such small details would not be noticeable in the scans even with an additional filtering process. However, by means of close range photogrammetry sparsely structured surfaces can hardly be measured with an adequate point density. Here, the combination of methods is the key to get best results with a reasonable amount of time, work and equipment.

3.2.5.3 *Deflectometry and close range photogrammetry in solar applications*

Photogrammetry and deflectometry are two optical measurement methods that have been compared and validated by measuring a typical mirror panel under optimal conditions [85].

A detailed error analysis is conducted for both methods and compared to the experimental findings. The both methods, when used correctly, show acceptable measurement uncertainties for presently achievable accuracies of CSP applications, but also give evidence that there are numerous sources of errors that can affect the results significantly. Both methods are suitable for quality control and further improvement of the panel shape, though deflectometry shows several advantages: it is much faster than photogrammetry (several minutes compared to several hours for CRP), more accurate and allows higher spatial resolutions. Furthermore, evaluation of the entire panel surface up to the very edges is possible, which is not the case for CRP.

3.2.5.4 *Laser tracker and CRP*

A large aerospace manufacturer conducted a comprehensive acceptance test of Geodetic Services Inc.'s (GSI's) V-STARS/S photogrammetric measurement system [67]. The purpose of the test was to establish the accuracy of CRP system on typical objects under industrial measurement conditions, using typical equipment, and aerospace company personnel. The tests were performed on two objects that represented a wide variety of potential applications. The two objects were measured in typical industrial measurement conditions, not in laboratory conditions. The results were compared to an independent measurement of the

object established by a laser tracker. Every practical step was taken to ensure the laser tracker measurement was of the highest possible accuracy.

The acceptance tests at this aerospace company established that the CRP system meets its established accuracy specifications, and is a reliable metrology system when used with proper procedures. The testing showed the system accuracy can be met in a wide variety of potential applications. In addition, the results were achieved using typical equipment in an industrial measuring environment using and trained aerospace personnel.

3.2.5.5 *Reverse Engineering and CRP*

Reverse Engineering techniques allow to get the digital duplication of a real object starting from a point cloud acquired with a 3D scanner from a point cloud by means of CMM (Coordinates Measure Machine). The use of CMM can ensure results very accurate ($\approx 1\mu m$), but shows two drawbacks [78]:

> 1) The digitizing phase is very slow, and due to the high number of points a powerful computer is needed.

> 2) The high cost of the CMM.

Today, optical systems, like laser scanner 3D, are often used in this applications. They allow to realize very fast acquisition with an acceptable smaller accuracy. Optical systems though less expensive than CMM, remains however too expensive.

The typical CMM process, often, involves an expensive and slow process for the 3D model acquisition and the shape reconstruction. By means of a photogrammetric process, instead, the errors can be very small by means of cheap tools in industrial applications on mechanical components. The Photogrammetry methods can be powerful alternative techniques in the CAD model reconstruction of small real objects. At present, it is possible to get interesting results in many fields and applications, even in the industrial sector. CRP allows the analysis of any features to be conducted obtaining reliable and accurate data.

3.3 Autocollimation based in-line solar facet verification cell

3.3.1 Introduction

This document presents a novel solution for the in-line control of solar reflector panels based on the autocollimation principle. The proposed technique outperforms previous approaches in several aspects. On the one hand, the inspection cell is only slightly larger than the reflector panel under test, as a result, the inspection cell is compact and improves the use of the layout of the plant. On the other hand, the measurements are carried out with considerably smaller uncertainties than other approaches. The compact arrangement of reflectors and autocollimators provides a solution that is very stable from the mechanical point of view. The measurement principle also contributes to low measurement uncertainties as it has been demonstrated in multitude of commercially available autocollimators. Finally, the measuring time is really short because the measurement consists on taking a simultaneous measurement

with the set of autocollimators, similar to taking one photograph. The commercial feasibility of the proposed approach demands the availability of cheap but yet accurate enough autocollimators. IK4-TEKNIKER has already demonstrated such possibility by the design, manufacture and testing of an autocollimator unit specifically developed for the application. Calibration of this device and also uncertainty estimation is also studied in this paper.

3.3.2 Description of the autocollimation based solution

The proposed measurement solution comprises a mount which supports as many autocollimators as control points are required for the reflector panel, see Figure 65. The number of control points lie in the order of one hundred, turning out enough for deriving the main characteristics of standard size panels.
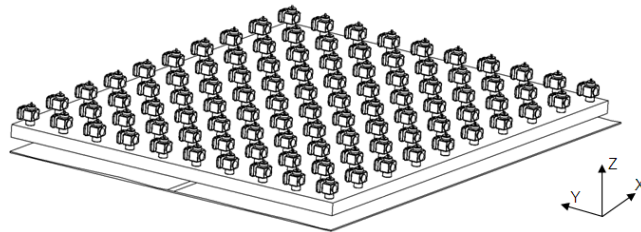

Figure 65. Mount with a set of autocollimators facing the reflector panel.

Autocollimators are high accuracy small angle measuring instruments well established in many technical areas. They are being used for alignment tasks in large scientific facilities, verification of rotary motions with the aid of calibrated polygon standards, verification of parasitic rotary motions of linear slides or deflectometric profilers among other applications [97].

The functional principle of an autocollimator [98] is deflectometry, as it is in many other reflector panel measurement solutions. However, due to the use of an autocolimating objective the distance between the instrument and the reflector panel does not affect the measurement, providing a much better chance to give accurate measurements.

As a result of the arrangement of a number of autocollimators in front of the reflector panel, direct measurements of panel slopes in both directions are obtained with a single reading of the autocollimator outputs. Only easy post-processing of the measurements is required in order to obtain the parameters of interest.

The advantages of the solution are the compactness of the cell, the short measuring time and low measurement uncertainties.

As shown in Figure 65, the functional elements of the verification cell only need to be slightly larger than the reflector panel itself. Compared to other solutions that need for a whole room, a big step on layout space savings is foreseen with the proposed solution.

With regard to the achievable cycle time, apart from the time required to handle the reflector panels and avoid issues related to the vibrations before establishing mechanically, the

measurement only implies taking a reading from each autocollimator simultaneously. That is it, the time to acquire a single image with an electronic device (both PSD or imaging CCD/CMOS solutions could be adopted). Compared to fringe projection solutions that require a multitude of projections and corresponding image acquisitions, it supposes a step forward in reducing measuring times.

Finally, a significant improvement on measurement uncertainties is expected with the proposed solution due to several reasons: improved geometrical stability of the functional parts of the cell and increased measuring accuracy of individual point measurements.

With regard to the geometrical stability, the improvement relies on the compactness of the solution compared to others that need for larger distances between functional elements (beamers or fringe standards, the reflector panel under study and image acquisition solutions composed of cameras and sometimes flat projection surfaces). The proposed solution only requires the stability of the mount where the autocollimators are fixed. The compactness also improves the whole cell vibration issues that large inspection cells could present in adverse shop-floor conditions.

On the other hand, autocollimators have been found to provide extremely accurate measurements in many applications. Among other reasons because they decouple at a large extent the measurand of interest, the angles, from other aspects. The basic deflectometry based solutions derive angle information from position, that is it, the measurements do not depend only on the measurand of interest, the angles, but also on the location of elements in space. Therefore, the uncertainty budget increases due to uncertainties on these locations, which does not happen on the proposed solution. Moreover, in the proposed solution the information generated by a complete CCD is available, resulting in an increased resolution of the measurements and therefore an improved accuracy as far as repeatability is achieved.

3.3.3 Development of the proposed solution

The feasibility of the proposed solution depends on several aspects:

- A technical solution is required for being able to align or calibrate the individual autocollimators in order to obtain all the individual readings in a common reference system.
- Standard autocollimators are expensive instruments. However, the verification of reflector panel for the solar energy industry is not demanding the accuracies provided by standard autocollimators. Therefore, the development of an autocollimator that perform well enough at a low price is a must.
- The autocollimators require a flat mirror in order to achieve the highest accuracies during its use. In this application the reflector panel flatness is not guaranteed, so its effect on the measurements must be investigated.

In the following sections these aspects are discussed.

3.3.3.1   Autocalibration solution for the cell

First of all, an individual calibration of all the autocollimators is necessary. Standard procedures to calibrate autocollimators can be applied.

A more challenging requirement consists in giving the measurements of all the autocollimators on a common reference system. With this purpose, the orientation of the autocollimators must be determined in such reference system.

Apart from manufacturing the mount and its mechanical interfaces with the autocollimators accurately enough, a calibration solution is envisaged as necessary in order to correct small misalignments, which reduces significantly the mechanical alignment requirements.

3.3.3.2   Development of low cost autocollimators

A must for the feasibility of the solution is the availability of cheap autocollimators whose performance is good enough for the application. The cost target for each autocollimator is in the order of few hundred dollars.

With this aim, a prototype autocollimator has been developed and tested. The development has been supported by optical simulation software ZEMAX. In Figure 66, the prototype autocollimator as well as a ray tracing simulation on ZEMAX are shown. The device has been designed to provide a ± 40 mrad measuring range.
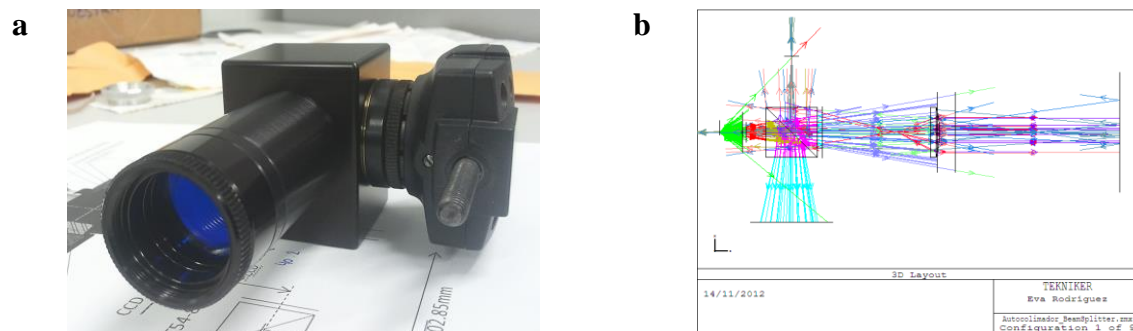

Figure 66. (a) Developed simple autocollimator; (b) ZEMAX ray tracing simulation of the autocollimator.

The first results obtained with the autocollimator are very encouraging. Even if measuring uncertainty has not been thoroughly studied yet, the measurement errors on several runs are under 0.015 mrad in the complete range of measurement, and the repeatability is better than 0.005 mrad. Tests have been carried out with the aid of a small angle generator table and precision electronic levels, see Figure 67.

Figure 67. Autocollimator calibration set up.

3.3.4 Application of the technology

3.3.4.1 Calibration of autocollimator-set mounted on a frame

In order to analyze the geometry of the mirror panel under test, the measurements of all the autocollimators should be carried out in the same coordinate system. Therefore, besides manufacturing the frame and the mechanical interfaces for mounting the autocollimators accurately, it is necessary to determine the correction to be applied to the every single autocollimator due to misalignment in relation to the nominal orientation.

Several approaches could be applied to determine these corrections. A conceptually simple solution is to measure with all the autocollimators a known surface geometry, a standard with the same size as the control mirror. This solution, though possible, requires the availability of a suitable standard and relies on the calibration and stability over time. Due to size of the mirror size, it may result in an impractical solution.

Next, another possibility is presented. It is an error separation technique in which error of each autocollimator can be calibrated together, using for this task a mirror of unknown geometry and pattern of a reduced size. There are many error separation and autocalibration techniques, and they are rarely directly applicable to different problems [99].

The developed calibration procedure involves carrying out several measurements with the set of autocollimators against the same mirror. Autocollimators frame moves in X and Y directions in the diverse measurements see Figure 66, so as to always deal with the same points of the mirror. That is, the movement in each direction is similar to the distance between the lines of autocollimators. Once the measurements have been realized, this technique can determine both the misalignment of the autocollimators and the geometry of the mirror, but this is not of interest in the calibration. Hence, the name 'error separation technique'.

In Figure 68, the elements, coordinate systems and variables involved in the mathematical development of the solution are described. The problem is studied in the XZ plane, so that the angles involved in a linear approximation, are the angles around the Y axis. On the one hand, both the mirror and mount have their own coordinate system. The autocollimator i, has its optical axis at an angle yi in relation to the frame, whereas the normal point of the mirror that

faces to the autocollimator i, has an angle vi with the Z axis of the coordinate system of the mirror.

On the frame, also a reference autocollimator is defined with *ref* index. The coordinate system of the frame is aligned with this autocollimator.
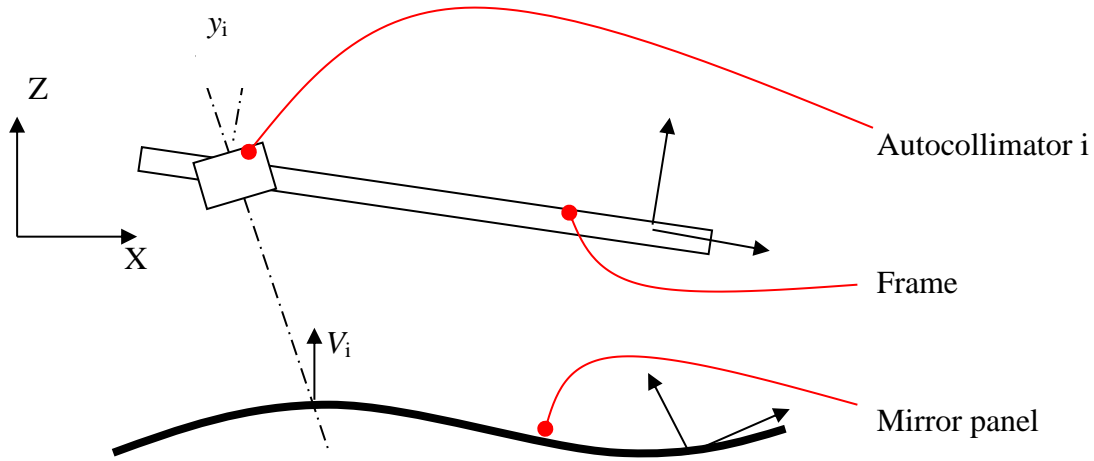

Figure 68. Variables that are involved in the calibration procedure.

Therefore, the autocollimator's measurement will be composed by,

$$m_i = y_i - v_i + C$$

considering C as the angle between the mirror and the frame.

Similarly, the reference autocollimator's measurement will be,

$$m_{ref} = y_{ref} - v_{ref} + C$$

And the relative measurement

$$m_i - m_{ref} = (y_i - y_{ref}) - (v_i - v_{ref})$$

The differences $(y_i - y_{ref})$ and $(v_i - v_{ref})$ will be the variables to be determined by means of the error separation technique. In Figure 69a, the numeric identification of each autocollimator (in red) and the points of the mirror (in black) are shown. The blue square represents the pattern which covers the points 65, 66, 75 and 76 of the mirror.Figure 69b shows the frame in a position moved a column in relation to the mirror. In this position, the measurement of the autocollimators will be,

$$m_i - m_{ref} = (y_i - y_{ref}) - (v_{i+1} - v_{ref+1}) = (y_i - y_{ref}) - (v_{i+1} - v_{ref}) + (v_{ref+1} - v_{ref})$$

And in the case of moving a row,

$$m_i - m_{ref} = (y_i - y_{ref}) - (v_{i+nCol} - v_{ref+nCol}) = (y_i - y_{ref}) - (v_{i+nCol} - v_{ref}) + (v_{ref+nCol} - v_{ref})$$
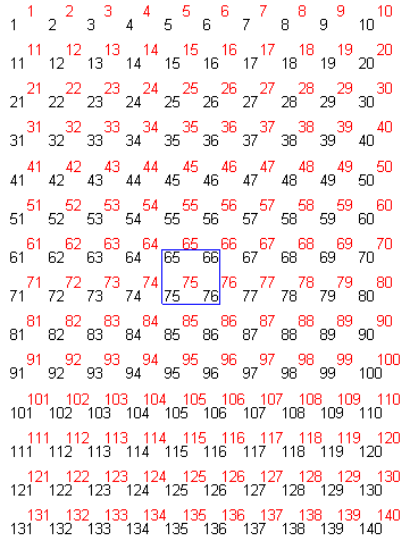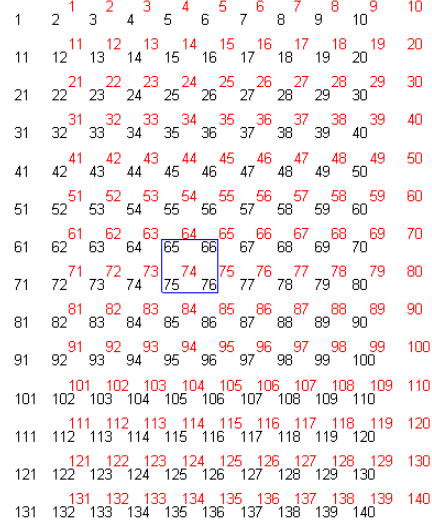
Figure 69. Mirror, pattern and frame in 2 relative positions.

nCol being the number of columns of the frame. Similarly other measurements can be carried out with other movements of the frame.

For each position of the frame, the relative measurement between each autocollimator and the reference one, adds an equation to the linear equation system. The independent terms to be determined are the differences mentioned above.

$$\begin{Bmatrix} m_1 - m_{ref} \\ ... \\ m_\alpha - m_{ref} \end{Bmatrix} = [M] \begin{Bmatrix} y_1 - y_{ref} \\ ... \\ y_{nColnFil} - y_{ref} \\ v_1 - v_{ref} \\ ... \\ v_{nColnFil} - v_{ref} \end{Bmatrix}$$

Those autocollimators that they are not facing the mirror, because they have moved beyond the edge, don´t perform any measurement and therefore, they don't add any equation to the linear system associated with that position and those autocollimators.

In the system of equations above, several known independent terms have been included. On the one hand, the differences $(y_{ref} - y_{ref})$ and $(v_{ref} - v_{ref})$ are equal to zero. Moreover, the pattern is also known. All of them must be removed from vector of independent terms and their contribution should be added to the measurements.

Similarly, and independently, calibration of the autocollimators around X axis can be established.

To carry out the propagation of uncertainty with the corrections identified in the calibration procedure, first the previous system of equations is rewritten as

$$\{m - m_{ref}\} - [M]_0 \{y - y_{ref}\}_0 = [M]_r \{y - y_{ref}\}_r$$

being

$\{m - m_{ref}\}$	The vector of measurements
$[M]_0$	M columns related to known
$\{y - y_{ref}\}_0$	The known parameters
$[M]_r$	M columns related to unknown
$\{y - y_{ref}\}$	The unknown parameters

The uncertainty of the terms on the left side considers the measurement uncertainty of the autocollimator and the uncertainty of the pattern.

After determining the uncertainties of the data for each linear system equation, and considering that the measurements are not correlated, the covariance matrix of the input data is constructed, C_m, with the square of the standard combined uncertainty of each input data on the diagonal. The estimated covariance matrix for the unknown parameters C_y is determined by [72].

$$[C_y] = \left([M_r]^t [C_m]^{-1} [M_r]\right)^{-1}$$

Proceeding as mentioned, it is possible to estimate the uncertainty of the correction of each autocollimator in different scenarios. In the following example, the case of a mirror in which 10 column points and a total of 14 rows are considered is presented (140 control points). The standard is centered under the frame with the autocollimators. Thus, the expanded uncertainties of each autocollimator's correction are shown in Figure 8. It is assumed to obtain an expanded uncertainty (k = 2) for each autocollimator about 0.020 mrad, an experimentally obtained value with the characterization of the prototype autocollimator, and an expanded uncertainty (k = 2) of the pattern that only covers four autocollimators of 0.005 mrad.

The results obtained in two different scenarios are presented below. Figure 70a, where, besides the measurement of the frame centered on the mirror, two additional measurements are taken by moving the frame a row and column respectively. In the second scenario, the column and row displacements occur in both directions, for a total of five measurements.

Five measurements (second scenario) provide substantially less uncertainty than three measurements (first scenario).
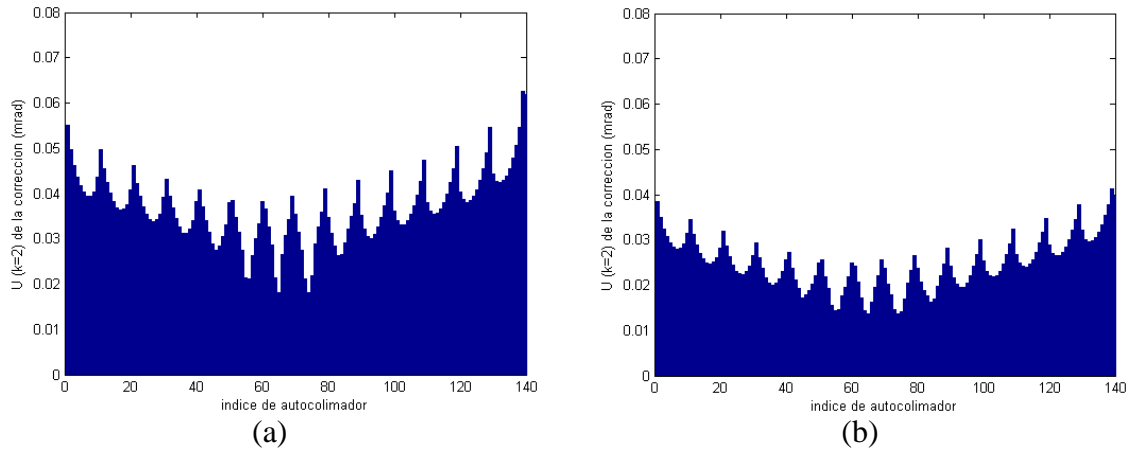
Figure 70. Uncertainty of the correction of each autocollimator:
(a) 3 measurements; (b) 5 measurements.

3.3.4.2 *Estimation of measurement uncertainty of the cell*

To carry out the inspection of a mirror, the measurements of the autocollimators are obtained and then the determined corrections for the calibration frame are applied

$$l_i = m_i - m_{ref} + (y_i - y_{ref})$$

The standard combined uncertainty of the measurement is obtained therefore by

$$u_{l_i}^2 = 2u_m^2 + u_c^2$$

Considering the previously shown error separation technique and the obtained corrections for the case with five relative positions between the frame and the mirror, uncertainties between 0.028 mrad and 0.048 mrad are obtained.

In this uncertainty analysis some parameters of influence were not considered in depth. For example, it was not considered the effect of misalignment of the autocollimators around its optical axis on the frame, neither the accuracy with which the frame of autocollimators is positioned above the mirror in the different positions of calibration, neither the influence that can cause a mirror whose flatness is not accurate. Anyway, it may be representative of the performance expected of a successful implementation of the proposed concept.

Finally, the detailed calibration method results in high correlations between the errors of the identified corrections. However, the correlation of the measurement errors of the cell is significantly lower due to the uncorrelated contribution of the uncertainty of the measurements of control points and the point of reference. Anyway, it may be necessary to consider the resulting correlation to determine the estimation uncertainty of features involving the measurement of a multitude of points, such as focal lengths.

3.3.5 Conclusions

A novel Inline reflector facet geometry verification cell has been proposed. The solution relies on the availability of economical autocollimator and technical solutions to calibrate a set of them against a common reference frame.

The first aspect has been faced by the design, manufacture and testing of a prototype, providing encouraging results. Measuring uncertainties around 0.015 mrad have been achieved with a prototype which cost is under 500$. The expected measurement uncertainties of the inspection cell lay in the 0.040 mrad in each measured point.

An autocalibration procedure has also been developed to cope with the second requirement of the proposed solution. As a result, practical calibration of the inspection cell is possible without the need of calibrated standards and external means.

Therefore, important steps towards the feasibility study of the proposal have been carried out, enabling the development of a novel solution that outperforms previous approaches in several aspects: Size of the cell, only slightly larger than the reflector facet under test; Measurements uncertainties, considerable smaller than other approaches; Inspection time, very short because the measurement consists on taking a simultaneous measurement with the set of autocollimators.

3.4 Theoretical Overlay Photographic (TOP) method

3.4.1 Introduction

The Theoretical Overlay Photographic Collector Alignment Method (TOPCAT) is a technique mainly used for trough concentrator alignment whose principle is to compare images of the reflection of the heat collection element (HCE) in the concentrating surface made by several cameras, to a theoretical projected image. Mirrors are then adjusted to bring the measured image to coincide with the theoretical image. With this approach, it is possible to make adjustments and observe real time feedback or to post process the information and subsequently prescribe adjustments to each mirror mounts.

3.4.2 Theoretical development
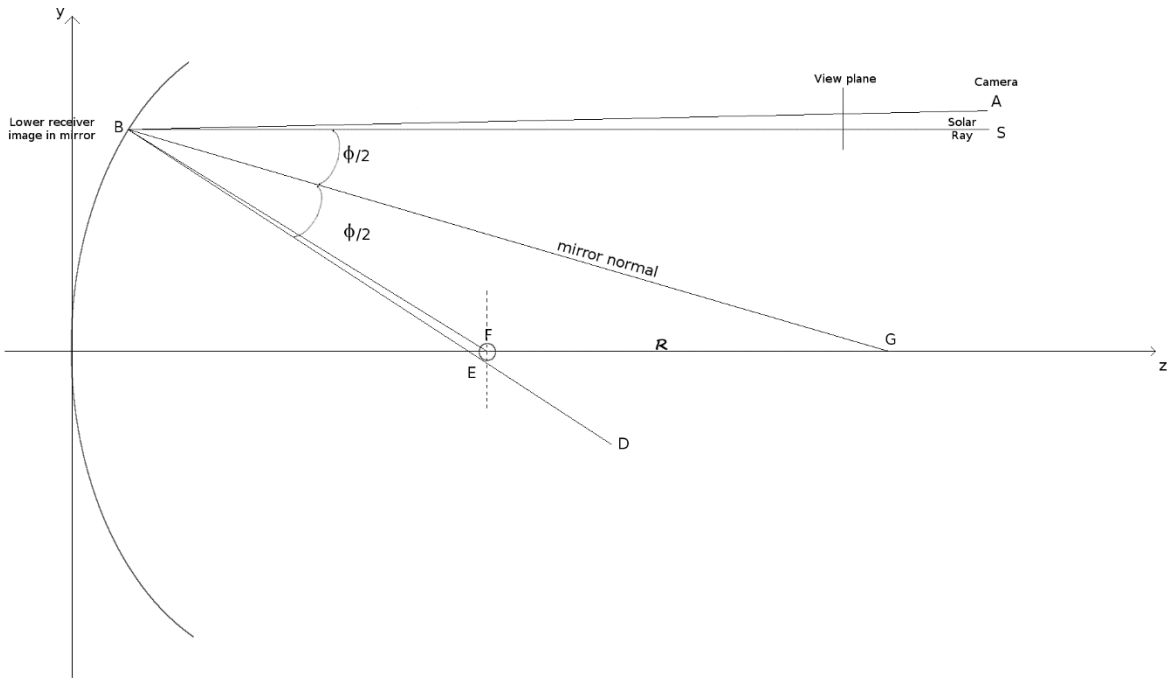
Figure 71. Schematic showing the coordinate system and useful geometric data.

Figure 71 represents a parabolic trough, the x axis is the axis of the cylinder and the z axis is the optical axis. Considering the light reflected from the sun (*S*) to the focus (*F*), the vector **BG** which represents the mirror normal for a perfect parabola, must bisect the angle SBF, and the distance *FG* and *BF* are equal (*R*). This relationship is true for all the points B belonging to the concentrating surface (but the value of R is not fixed).

As we say in the introduction, we have to calculate the theoretical position of the HCE image in the mirror and then determining a graphical projection of the image and mirrors as seen by the camera. We will not consider the alignment errors along the x-axis because the trough shouldn't have curvature along these axes.

To determine the location of the image of the lower receiver edge in the mirror (B) as seen by the camera (A), the reflected vector **BD** can be iteratively calculated using the vector **BA** from the camera to the mirror and the mirror normal vector **BG** by the use of the following formula:

$$\mathbf{BD} = 2\left(\frac{\langle \mathbf{BA}|\mathbf{BG}\rangle}{\langle \mathbf{BG}|\mathbf{BG}\rangle}\right)\mathbf{BG} - \mathbf{BA}$$

We consider that vectors **BD** and **BA** have the same magnitude. Note that every point *B* along the theoretical parabola has a unique mirror normal that can be determined with the equations of the parabola:

$$B_z = \frac{B_y^2}{4f} \quad \text{and} \quad R = \frac{2f}{1+\cos\phi}$$

The point E where vector **BD** intersects the target plane corresponds to the bottom edge of the HCE and can be calculated by obtaining the y component of vector **BD**.

Let's call M the scale factor between **BE** and **BD**

$$\mathbf{BE} = M.\mathbf{BD} \quad \Rightarrow \quad M = \frac{E_z - B_z}{D_z - B_z}$$

And the y coordinates of the point E is

$$E_y = B_y + M(D_y - B_y)$$

However this set of equations is not sufficient to explicitly solve the location of the point B, it requires an iterative solution. In addition, because of the form of the HCE, the effective location corresponding of the intersection of vector **BD** and the HCE depends on the angle in the z-y plane of vector **BD**. For the lower and upper receiver edge image, the effective target plane locations are

$$E_y = \frac{-r}{\cos(\phi + \frac{r}{R})} \quad \text{and} \quad E_y = \frac{r}{\cos(\phi + \frac{r}{R})}$$

Where r is the HCE tube radius.

The previous equations when iteratively solved can determine the y locations on the mirror corresponding to the bottom and top edge of the HCE absorber as seen from the camera. As the trough has no curvature along the x-axis and assuming the HCE's and trough's lengths are the same, it should not be difficult to determine the x theoretical location of the point E.

Solving the above equations for both sides and ends of the HCE gives the theoretical corner positions on the mirrors of the reflected image as seen by the camera of perfectly aligned parabolic mirrors.

3.4.3 Alignment Approach
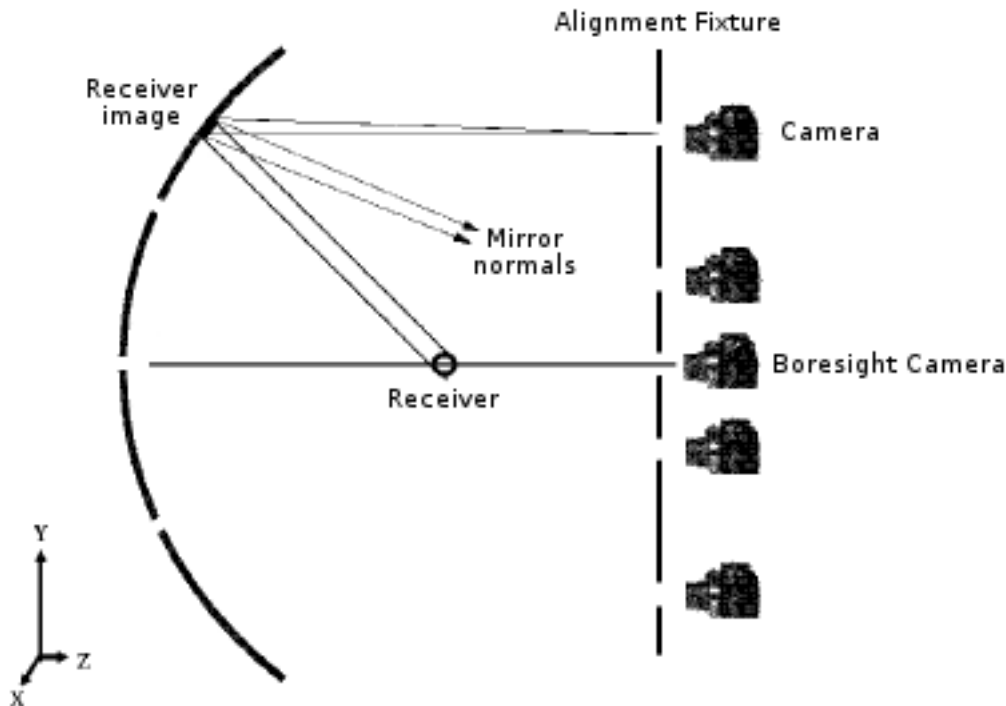
Figure 72. TOP alignment technique.

Figure 72 illustrates the basic principles of the TOP alignment approach. The alignment fixture is placed at a convenient distance from the trough collector, which means close enough to be within the row in the trough field and far enough away so that a camera can see an entire module without significant distortion of the image. The trough is pointed horizontally toward the fixture which contains five cameras, one for each module plus a boresight camera to help to position the fixture correctly regarding the trough with the help of some boresight gauges.

Images taken by the other four cameras are then used to align the mirrors in each of the four rows in the module. Each camera records the location of the collector in each mirror as a digital photographic image. The HCE image location in the photograph is then compared to the theoretical projected image location by overlaying the two images. Mirrors are then adjusted to bring the measured image to coincide with the theoretical image. This approach allowed us to make adjustments and observe the slopes in real time or to post-process the information and prescribe adjustments to each mirror.

The accuracy of this technique could potentially be improved by the use of additional cameras (or camera positions), or by the use of computational comparisons of the measured and theoretical images. The difference between the theoretical and measured HCE image edge locations as seen by the camera can be used to measure the vertical component of mirror slope error magnitude and direction for each corresponding image pixel location in the mirror. By taking images at multiple locations per row, this technique could be used to optically characterize individual mirrors or mirrors on modules with high spatial resolution.

To apply this technology at an industrial scale for parabolic trough power plant, a trailer-mounted camera fixture surveyed by technicians could be envisioned. After adjusting the fixture to boresight the center camera on axis with the trough and checking the verticality of the fixture, images would be taken and stored in a database. The fixture would then be driven to the next concentrator and the process repeated for the entire field. The image processing of the data recorded could be done later and the alignment adjustments when convenient. Additional measurement to ensure proper alignment would be made for quality assurance.

3.4.4   Test results

The TOPCAT method has been tested on different loops in California. The latest one (found in the literature) has been performed in June 2009 on an LS-3 loop at the SEGS VIII and IX parabolic trough power plants.

The data collection was performed with a pickup truck mounted TOPCAT field characterization system. This fixture permitted to reduce the measurement time to 20 seconds per module and less than 45 minutes per loop of LS-3 collectors at SEGS VIII and XI.

This alignment characterization is feasible under most conditions. The fixture is stable enough to characterize alignment in winds up to 40 km/h. However, to minimize camera glare from reflected images of the sun in mirrors, especially in the morning, it is preferable to acquire data the winter and fall (acquisition have been performed during the day for lightning reasons). It has been shown during this measurement campaign that the TOPCAT method is capable of reducing the magnitude of alignment errors to less than mirror slope errors and can reduce the need for precise manufacturing fixtures. The data indicates a 3°C increase in loop outlet temperature or an improvement of 3.5%.

3.4.5   Application to heliostat fields

Since the TOPCAT method has been successfully demonstrated for aligning the trough concentrators, an adaptation of this method has been developed. In this new method, the alignment fixture has nine special targets and five cameras disposed as in the Figure 73.

Figure 73. Target used for TOP alignment technique on heliostats.

The size of the alignment fixture is equivalent to the chosen heliostat. At the beginning of the process, the alignment fixture is in front of the heliostat and it is oriented vertically. Each camera is used to take many pictures. Based on rangefinder, one can determine the relationship of the distance between the alignment fixture and the chosen heliostat. The theoretical position of the nine targets can be calculated from the image based on reflection principles. The mirror facet is aligned repeatedly until the photographic images of the targets match the theoretical images.

I didn't manage to find a lot of articles dealing with this method applied to heliostats' fields (just Ren et al Review and a poster from Sandia laboratories), however I think that the setting-up of this methods on heliostats fields could be difficult. First of all moving such a target through the field could not be easy on power plants were the heliostats are on a hill or on the ground without asphalt on it. In this way, the setting-up of the method could need to asphalt the all field. Then, the position of the target is unclear: its dimensions are the same as a heliostat, although these heliostats have different focal distances and the target isn't positioned at infinity so the principle of the TOPCAT method for the parabolic troughs couldn't be applied.

3.5 Deflectometry

3.5.1 General points

3.5.1.1 Definition

Deflectometry, also known as the fringe reflection method, is an optical measurement technique which consists in studying the deformation of a reflection on a specular surface.

In this method, a fringe pattern is projected onto a screen which is then reflected by a mirror, and finally the reflected image is recorded by a digital camera (a fringe pattern target can be used instead of the projector and the screen). In most cases, the acquisition has to be realized with 2 fringe patterns, one with horizontal same thickness fringes, and the other with vertical same thickness fringes.

Then the local slopes are determined directly by image processing or phase shifting techniques. Further advantages of deflectometry are its high resolution, short measurement time and accuracy. In this way, deflectometry seems to be a promising method for fast heliostat calibration even if some problems related to the position of the camera and to the numerical treatments need to be solved.

### 3.5.1.2   *Experimental protocol and data acquisition*
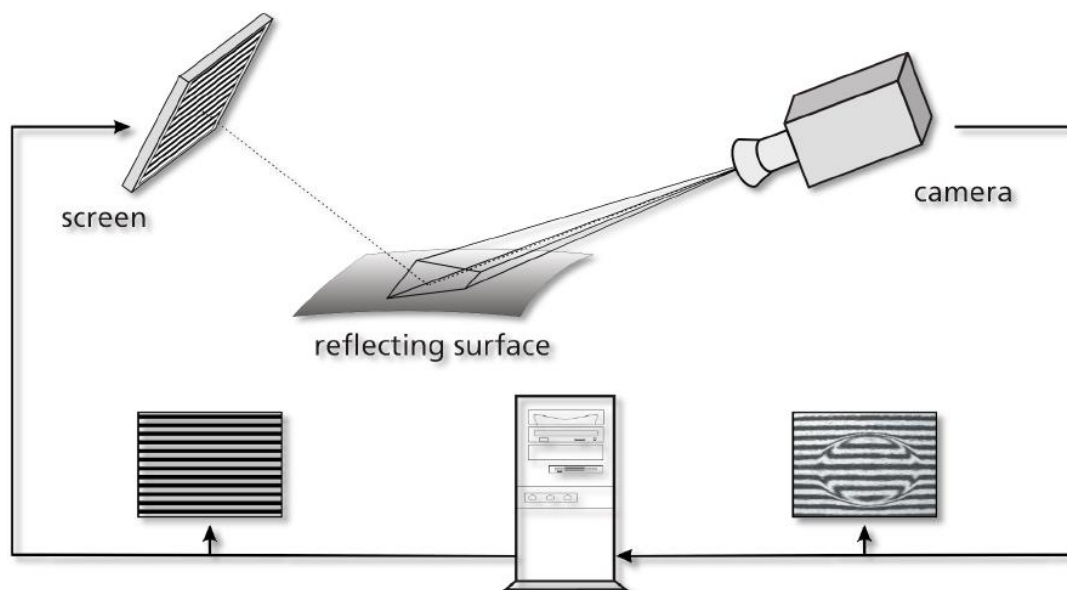
Figure 74. Set-up used for deflectometry measurement [108].

There are two possibilities to image fringes with the camera: first the fringes can be projected on a screen which is reflected by the surface, or the fringes can be drawn on the target. There aren't any fundamental differences between the two methods, except the fact that it would be easier to change the direction of the fringes using the projector than rotating the target.

3.5.1.3   *Methods of fringes analysis*

3.5.1.3.1 Phase-shifting method

This method is based on the same principle used for Fizeau and Zygo interferometer, that is to say the optical phase is proportional to the surface's slopes and it's possible to calculate them from several acquisitions of the same signal to which we add a known phase.

The signal recorded by the sensor is of the form of $= a + b\cos(\varphi + \phi)$. Let's consider the case where we record 3 images with $\phi_i = \frac{2i\pi}{3}$ $i\epsilon[1:3]$. We obtain the signals: $e_i = a + b\cos(\varphi + \phi_i)$.

By developing the cosines from the two first signals using usual trigonometric formulae we can obtain: $2e_3 - e_2 - e_1 = 3cos(\varphi)$ and $e_2 - e_1 = \sqrt{3}b \sin(\varphi)$

which permits to obtain the phase by

$$\varphi = \arctan(\sqrt{3} \frac{e_2 - e_1}{2e_3 - e_2 - e_1})$$

This formulae can be generalized for n signals:

$$\varphi = \arctan(\frac{\sum_{i=1}^{n} e_i \sin((i-1)\phi)}{\sum_{i=1}^{n} e_i \cos((i-1)\phi)})$$

However, we have to project close numerous sinusoidal fringes to be accurate with this method.

3.5.1.3.2 Fourier Transform

As for the phase-shifting method, this method needs the projection of numerous close range fringes to be accurate. The objective is similar, because we want to find the phase of the signal.

We consider that the recorded signal can be expressed as

$$e(x,y) = a(x,y) + b(x,y)\cos[2\pi f_0 + \phi(x,y)]$$

where x and y are the coordinates according to two perpendicular axes associated with the detector. Let's write out $c(x,y) = \frac{1}{2}b(x,y) \exp[i\phi(x,y)]$.

Now we can write:

$$e(x,y) = a(x,y) + c(x,y) \exp(2i\pi f_0 x) + c^*(x,y) \exp(-2i\pi f_0 x)$$

By using the Fourier transform according to x of the equation (3), we obtain:

$$E(f,y) = A(f,y) + C(f - f_0, y) + C^*(f + f_0, y)$$

where the capital letters are the Fourier spectra and f is the spatial frequency matching the x axis. So we obtain three maxima and the further to the right corresponds to $C(f - f_0, y)$. We translate this peak of f_0 to obtain $C(f,y)$, then we apply the Fourier inversion theorem according to f to the peak to obtain $c(x,y)$. Now we can use the complex logarithm and then find the phase ϕ by taking the imaginary part of the left part of the next equation:

$$ln[c(x,y)] = ln[\frac{1}{2}b(x,y)] + i\phi(x,y)$$

3.5.2 Review of different applications

3.5.2.1 SOFAST method (Sandia Optical Fringe Analysis Slope Tool)

SOFAST is a mirror facet characterization system based on deflectometry that has been developed at Sandia National Laboratories [109]. It has been developed for quick characterization of point focus mirror facets and heliostats. Concerning the hardware, the fringe reflection approach is shown in Figure 75. A camera views the facet, which is positioned such that the camera sees the reflection of the target in the facet. The target is an LCD monitor which shows sinusoidal fringes. The advantage of such a device is that the spatial control of the fringes is easy and accurate. The camera and the target need to be carefully positioned relative to each over so they are fastened together.
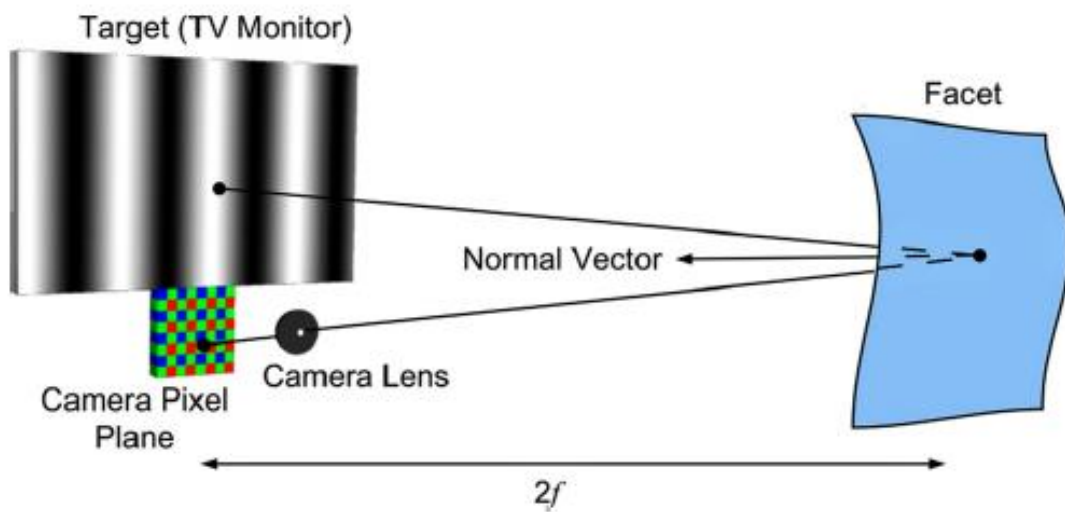

Figure 75. Fringe reflection method layout [110].

The system is positioned such that the entire mirror reflects the target from the point of view of the camera. Then the acquisition is recorded for a sinusoidal fringe brightness pattern on the target which is shifted 3 times. Four images are obtained, so the phase ϕ can be obtained by a similar method as the one presented in Section 3.5.1.3.1:

$$tan(\phi(x,y)) = \frac{I_4 - I_2}{I_1 - I_3}$$

where the I's are the intensities of the pixel during each of the phase-shifted displays. The process is repeated according to a perpendicular axe to determine the coordinates of the target position in two dimensions. These data can be easily converted to slope data and then fitted to the following equations via least squares.

$$\frac{\partial z}{\partial x} = 2Ax + C + Ey$$

$$\frac{\partial z}{\partial y} = 2By + D + Ex$$

where facet focal lengths are represented by $\frac{1}{4A}$ and $\frac{1}{4B}$, the C and D terms can be interpreted as the tilt of the facet, and E represents others aberrations depending on the shape of the facet. An analysis of the SOFAST system used to characterize 24 ADDS (Advanced Dish Development System) has been performed by Finch and Andraka in 2014 [101].This study has shown that SOFAST can provide facet characterization with extremely low focal length uncertainty (<0.5%), local slope measurements accurate to within ±0.05 mrad and global slope measurements accurate to within ±0.005 mrad.

In this way, the SOFAST system seems to be a method with a very decent accuracy with an acquisition time of only a few seconds. Unfortunately this system can characterize only one facet at once, which for a field with hundreds of heliostat can be time consuming if we have to move and adjust the device for each acquisition.

3.5.2.2 Calibration of parabolic troughs using the reflected image of the absorber tube

In the case of parabolic trough collectors, methods have been developed using the reflection of the absorber tube in the concentrator as seen from some distance.

TARMES (Trough Absorber Reflection Measurement System) was developed to achieve high accuracy and high spatial resolution and produces slope error maps in curvature direction from a set of photos.
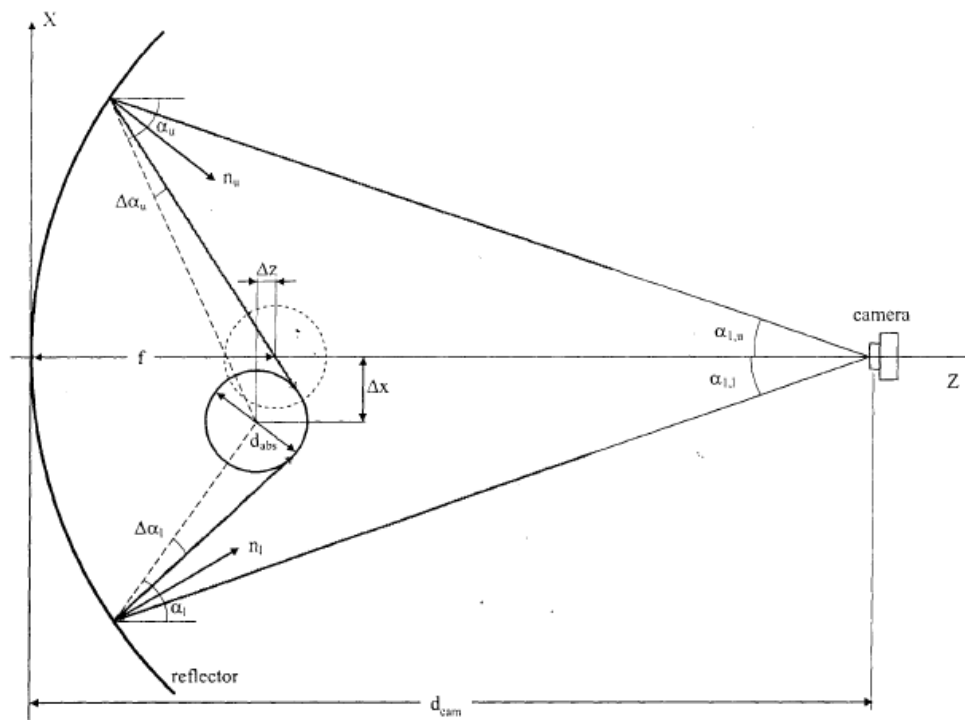

Figure 76. Measurement set-up for the TARMES method [114].

The measurement set-up is shown on Figure 76: a digital camera is placed at a distance around a hundred times the focal length close to the optical axis of the concentrator. The absorber tube has a possible deviation represented by Δx and Δz from its ideal position due to

manufacturing accuracy and temperature variations. At the distance d_{cam}, we can consider that the rays from the camera to the concentrator are parallel, and the reflection of the absorber tube appears largely magnified in the concentrator. Before starting the measurement, the collector is tilted until the reflection disappears completely. Then, a series of picture is taken while tilting the collector until the reflector disappears completely on the other side (the total tilt angle is about 5 deg).
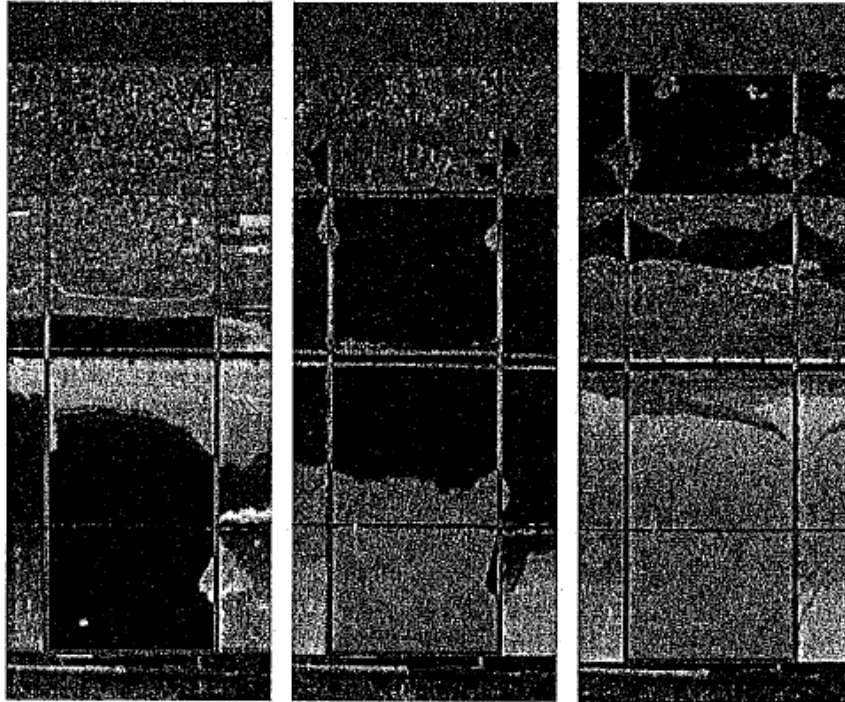

Figure 77. **Reflected images of the absorber tube with different tilts of the collector [113].**

The slopes are then evaluated by computer software and the accuracy obtained is around ±1 mrad. With this method, the collectors are easily measured facing horizon, while the measurement of a trough collector in its prevailing operating position (around zenith) involves considerably increased effort. That's why this method has been improved by replacing the terrestrial camera by an airborne one in the Qfly method [113].

With airborne image acquisition, the collector must remain at a certain elevation angle and the variety of view angles is achieved by moving the camera perpendicular to the collector axis. However, the relative position between the camera and the collector have to be known accurately and the use of GPS is not enough accurate or too expensive. In this way, a photogrammetric evaluation has to be done to determine this parameter. In addition, weather condition have to be appropriate, the wind speed in particular has to be under $6 \ m.s^{-1}$. Concerning the uncertainty of the measurement, it's complicated to have a good estimation because the uncertainties accumulate (most of them concerning the position of the airborne drone) but the accuracy seems to be ±0.1mrad based on a level of confidence of 68.3%.

3.5.2.3 *Measurement system for solar tower power plant*

The measurement system used for this method is presented in Figure 78:
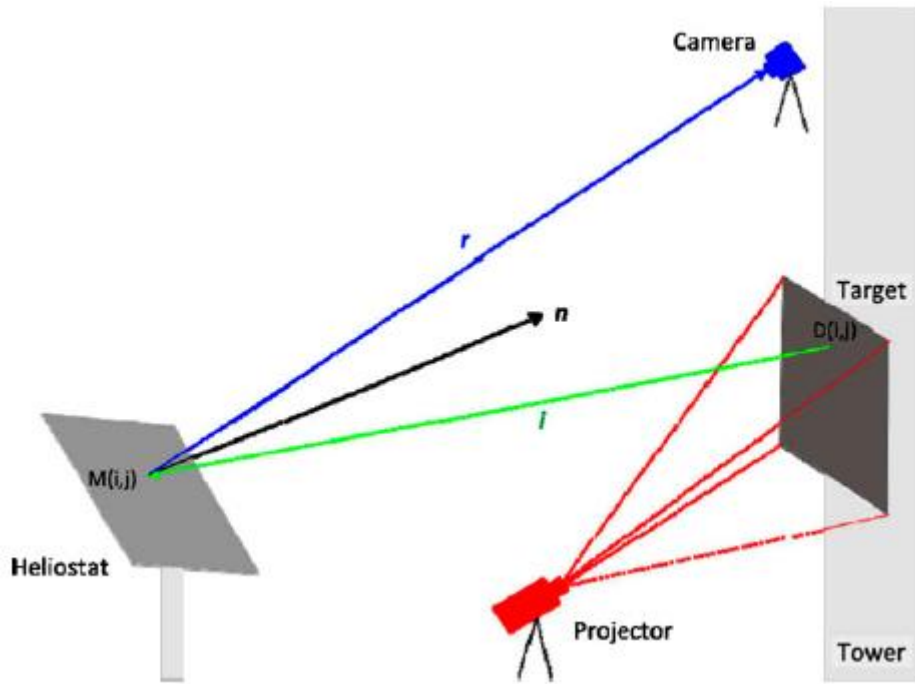
Figure 78. Measurement set-up used for heliostat measurements in the field.

The acquisition took place at night, a projector is used to cast the fringes on a target positioned on the tower then a camera is used to film the heliostat which reflects the target. The identification of the reflected target points is achieved by codifying the target surface with labeled sinusoidal brightness variations stripe patterns. Vertical stripes are used to codify the target in the y-direction and horizontal stripes are used for the x-direction.
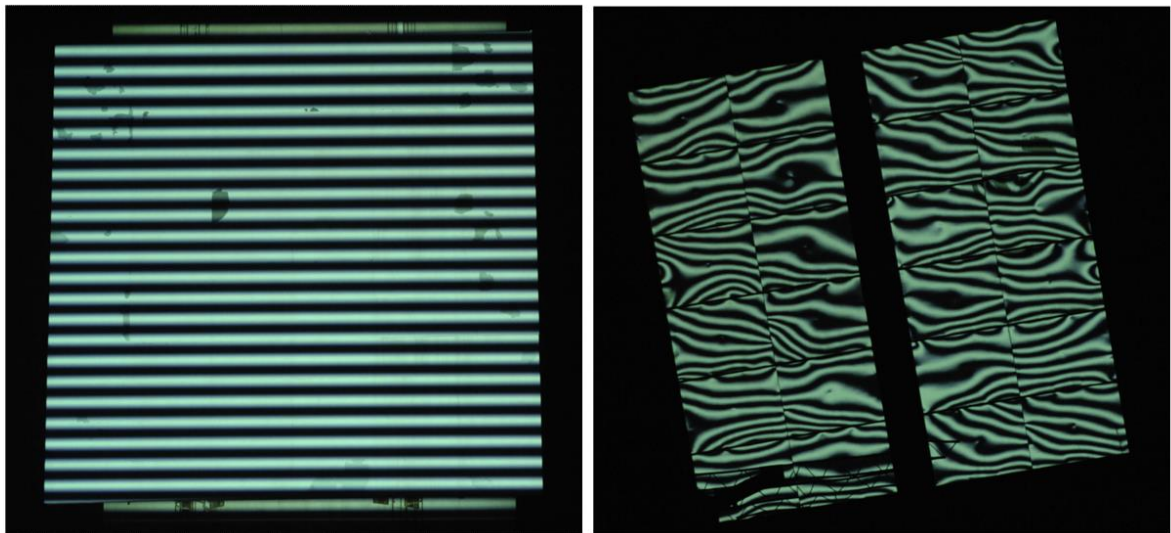
*Figure 79. The fringes projected on the target (left) and an example of reflection by an heliostat (right) [115].*

From the brightness seen at a certain point, the corresponding phase of the sinus wave can be assigned. Using four patterns with a phase shift of $\frac{\pi}{2}$ between each, the phase can be determined using the formula (6). The accuracy can be improved by repeating the acquisition

with different wavelengths. The surface normal vectors are then calculated by a computer software which also corrected errors like lens distortions.

The measurement procedure and evaluation was automated: an industrial type CCD camera with a computer controlled tilt head allow completely automatic scan of the entire heliostat fields. Nevertheless, some start values for automatic edge detection and thresholds have to be determined, which is done during the evaluation of the first heliostat. The evaluation for one heliostat is around 1 min which permits to evaluate the entire fields in one night.

The system was tested at the CESA-1 Plataforma Solar de Almeria: the measurement has a resolution of about 1 million points per heliostat with a measurement uncertainty of less than 0.2 mrad. Although this method shows considerable advantages, we can wonder if the accuracy is sufficient (0.2 mrad). Another limitation is that the facets need to be pre-aligned to guarantee that the reflection of the stripe patterns on the target can be seen in the entire heliostat.

3.5.3 Conclusion about performances and advantages/drawbacks

Name of the method	SOFAST	TARMES	Qfly	Deflectometry for solar tower plants
Main advantages	> High accuracy (< 0,05 mrad)	> Fast measurement time > Only one camera is needed to perform the acquisition	> Good accuracy (±0,1 mrad) > The acquisition can be done quickly (about a day for a parabolic trough collector field but it depends on the weather conditions and on the number of images taken)	> Quick and completely automated
Main drawbacks and Remaining problems	> This method's objective is to determine the small defaults of the surface, not to calibrate an heliostat field, it will be to long to analyse all the heliostat with SOFAST devices	> All the troughs collectors have to faced the horizon for the measurement to be achieved > The accuracy obtained (≈±1 mrad) may not be sufficient	> The position of the camera in the air needs to be known exactly so an another system is needed and the errors accumulate > The system depends hardly on wind conditions	> The facets need to be prealigned because the system cannot detect too important defaults

Figure 80. Comparison between the different deflectometry methods.

We can have noticed that deflectometry can be used to calibrate an all heliostat field in a reasonable time with the methods described in the sections 2.2 and 2.3 with a good accuracy. In addition, these methods require less devices than others methods like photogrammetry or VSHOT. However the Qfly can be difficult to put into practice because of the wind and others mistakes related to the position of the aircraft, and the method used for the solar tower power plants can't be used if the facets have huge slope defaults.

Table 5. Advantages and disadvantages of the methods.

	V-SHOT method	Photogrammetry	Autocollimation (IK4)	Deflectometry	TOPCAT
Speed, easy-to-use	The V-SHOT method needs a high number of measure points, so the scanning task could be time-consuming	The acquisitions could be a time-consuming task	The acquisition consist of taking only one picture so we can hope that it will be performed quickly	The automation described in Ulmer et al [116] allows substantial gain in time and set-up	The acquisition on a loop can be performed in less than 45 mn
Cost and hardware	Lazer + Target + Camera	Camera + equipment to position it accurately + heliostats equipped with targets	Need in the order of one hundred collimators (~500$ each)	Cameras + controls + target	Pick-up + cameras + control fixture (+ targets and wheels for TOPHAT
Possibility to perform the adjustments without disturbing the power plant's functioning	Impossible (the concentrating surface have to face the devices used to perform the acquisition) but could be performed at night	Seems difficult (the heliostat has to be fixed) Maybe at night?	The system is envisaged to perform quality control of panels in assembly line, the application to panels in the field requires a feasibility study.	Deflectometry can be performed at night	Impossible to not disturb the functionning by day, the method hasn't been tested by night for lightning reasons
Other drawbacks	In the case of long focal lengths heliostats, there are problems with the accuracy of the lazer	- The method is very sensitive, a small error on a camera's position can have huge consequences on the results - Deflectometry seems to be better on the three standards considered	Can't be used for out-door measurements or verifying large solar fields	- In certain cases the reconstruction performed by image processing could be a source of issues - If an heliostat is misadjust with an error taller than 2 mrad, the error can't be measured (on heliostats fields)	There isn't mush literature about the TOPHAT method, we wonder if this method is convenient to use but we doubt it

| **Main applications** | Calibration of parabolic troughs and short focal lengths heliostats | Useful to know accurately the shape of the surface and the small defaults | On-line verification, assistance during concentrator/heliostats assembling process | The different methods based on fringe reflection principles allowed to use deflectometry for fast calibration of parabolic troughs and tower power plants | Fast calibration of parabolic troughs power plants (TOPCAT) and heliostats fields (TOPHAT) |

3.6 Conclusions

Five methods for measurements of solar concentrators were discussed above. All of them have their own advantages and disadvantages.

It has been identified that the selected method must verify the following standards:

- First the method must be easy to set-up and the acquisition time should be the shortest possible
- Then the method must permit to adjust the heliostat with minimum cost and hardware
- Finally it will be a great advantage if the method could be applied without disturbing the power plant operation, by performing the acquisition during the working or by setting up the method by night.

Here is a quick summary of the possibilities of the previous methods regarding these standards:

Depending on the type of power plant we want to calibrate, here are the different possibilities:

First of all for parabolic trough power plant:

- The VSHOT method can be used, we suppose that the devices could be moved easily next to the troughs and that the short focal lengths (6-15 m) of this kind of surfaces wouldn't disturb the acquisitions. However the problem of time-consuming acquisitions remains.
- Deflectometry could be used, especially the TARMES method, but we suppose that moving the collector could be constraining.
- Of course Photogrammetry could be used, however the acquisitions are very long. It could be a good idea to detect small defaults at the surface of the mirrors or high orders optical aberrations but not for fast optical calibration.
- Finally the TOPCAT method seems to be the fastest to set up.

Then to calibrate heliostats fields associate to tower power plants. The main difference with the parabolic troughs is that the focal lengths of the concentrating surfaces are now from 80 m to about 1000m.

- Photogrammetry could be used with the same drawbacks as we explained before
- The TOPHAT seems adapted but we have found little information about it and we suppose that moving the target wouldn't be so easy if the field isn't asphalted.
- Finally the method described by Ulmer et al [117] based on Deflectometry seems to be the fastest to set-up and the more adapted, however the fact that the maximum angular default the method can detect is 2 mrad could be prejudicial.

4 Heliostat calibration procedures

4.1 State of the art

4.1.1 Introduction

Several methods exist for controlling heliostat tracking. For the heliostats to concentrate solar radiations on the receiver, their inclinations have to be aligned on the solar position. In most of cases, a pre-alignment is made by calculating the solar position and adjusting the heliostat on this theoretical value, then a system to control that the radiations are well reflected on the receiver is set-up, which can correct misalignment errors. In the first section, the principle of the automatic control of heliostat tracking errors and correction is exposed. In the second section, the state-of-the-art of the techniques used to detect heliostat misalignment with different devices is given. Finally, a development from ENEA trying to implement a closed-loop control that avoids the need for heliostat calibration is also summarized.

4.1.2 Method for automatic control of heliostat track alignment

The following flow-chart is showing an algorithm which can be used for closed-loop control of alignment of heliostats (from Patent US 4,564,275 [123]).
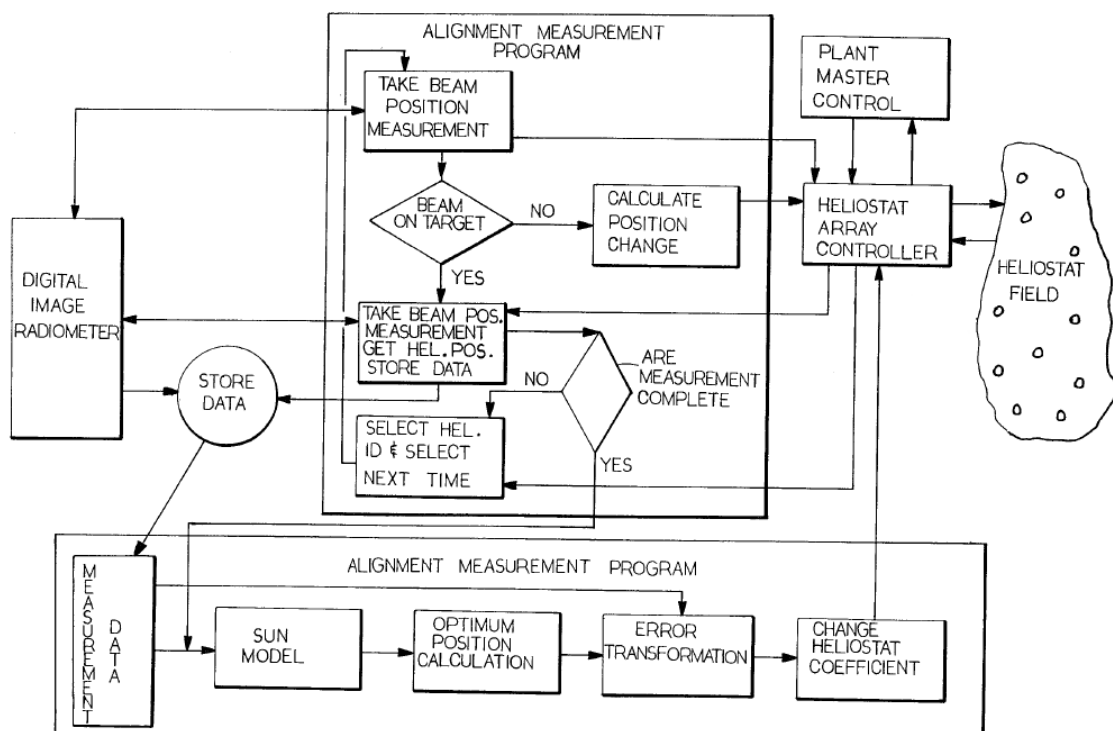
An alignment measurement program systematically selects a heliostat from the heliostat field for alignment. A heliostat array controller interfaces the individual controllers in the field. A

master control station provides manual override for the system and allows the operator to be in complete control of the heliostat field. The heliostat selected from the field is identified, the time of day noted, and the computer makes a measurement to check its position using the digital image radiometer. Each heliostat must have several position measurements made periodically to collect enough data to make the necessary alignment calculations. Three measurements are taken for each heliostat with approximately a two hours interval between the measurements. One measurement may only take a couple of minutes. If the beam is not on the target, a position change is calculated and the heliostat's position is changed to place the beam on the target before measurement is made and another heliostat is selected. The computer selects each heliostat for the first measurement in a first supervision of the field. After the first measurements are made, the measurement process is repeated for the second supervision of the field at a stored time interval for each heliostat.

When the last set of measurements is being made, the first heliostat selected has its alignment coefficients checked by the alignment calculation program 56. The alignment calculation program 56 determines a new set of coefficients for the heliostat by analyzing the beam centroid error. The new alignment data is stored and the heliostat array controller 54 then commands the heliostat to its new position by means of its individual controller. The next heliostat is then selected and the last measurement is made, the alignment coefficients checked, and new coefficients are stored and sent to the controller.

In the alignment program, calculations are made for the sun's position based upon the stored time data when the measurements were made. Such factors as the sun's azimuth and elevation are calculated. This process is represented by the sun model block in the flow chart diagram. The program then calculates the position of the heliostat based upon the sun's position and the command position of the sunbeam. Once the program has calculated the optimum heliostat position, this information is compared with the stored measurements made. In the error transformation routine errors between the command position and the measured positions are used to calculate the alignment error coefficients.

4.1.3 Controller systems for heliostat tracking

Two types of controller systems were developed. The first one is located on the heliostat, whereas the second is located on the tower close to the receiver. Below the state-of-the-art systems are reported and discussed.

4.1.3.1 *Closed loop system with a viewfinder at the Big Solar Furnace (CNRS-PROMES, France)*

The heliostats of the 1MW-CNRS Big Solar Furnace at Odeillo (France) are located on terraces to reflect the sun rays horizontally. All the heliostats are independent and include an anchorage viewfinder (which will be replaced by a camera) placed in front of the central facet, as shown on the picture below.

This procedure is divided in two steps. First, the positions of the sun are calculated with an algorithm based on the VSOP87 (Variations Séculaires des Orbites Planétaires), and the angles of each heliostat are determined according to these positions. This adjustment is made for the central facet to reflect the sun to the camera that enables the camera to make an image of the sun. Secondly, the tracking based on a closed loop begins. The purpose of this second adjustment is to correct the error between the position of the reflection of the sun seen by the camera and the ideal position which is the center of the picture of the facet taken by the camera. With this information, a PID corrector calculates the appropriated angular speed for the heliostat to correct its position.

The advantage of this method is its accuracy but the main drawback is the cost and the longevity of such electronic devices exposed to weather changes.

4.1.3.2 *Closed loop control of heliostats (Tel Aviv University, Weizmann Institute of Science, Israël)*

In 2004, a closed loop control system was presented by A. Kribus et al. [122]. This method is based on the measurement of the incident solar radiations on the edge of the receiver, without disturbing the operation of the plant. This system allows dynamic corrections for tracking errors and assigns individual corrections for heliostats in the field. The method was tested at the Weizmann Institute Solar Tower (Israël), and a detection sensitivity of 0.3 mrad was achieved.
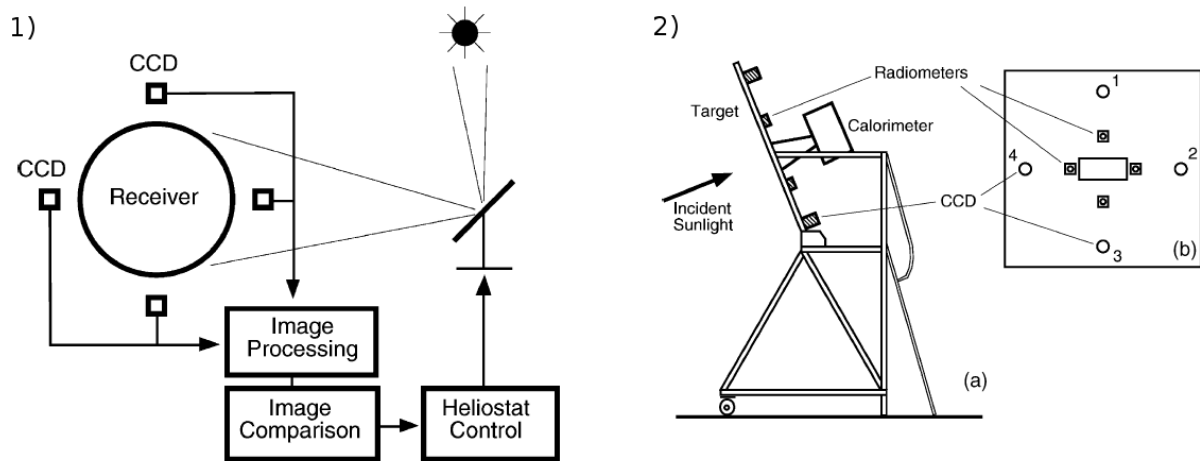
Figure 81. 1) Method Flow-chart 2) Set-up.

The set-up is presented on the figure above. The square target (2x2 m) is made of alumina, and is supported by a steel frame. A small central aperture leads to a calorimeter. The four cameras aims at the same portion of the heliostat fields, centered on the heliostat 307. The image analysis determines the edge of the heliostat in each of the four images. Then, the average brightness within the detected area is computed for each image, and the control correction is determined.

The system has been tested by introducing errors on the heliostat and letting the closed loop system to correct these errors. The sensitivity of aiming error detection corresponds to a tracking error of 0.1-0.3 mrad (at the Weizmann Institute heliostat field). The accuracy is limited by the opticalquality of the heliostat and the resolution of the tracking mechanism.

4.1.3.3 *Double feedback control method for a heliostat (Patent US 7,207,327 B2 [124])*

The purpose of this patent is to describe an optical system for closed loop control of the position of a movable heliostat used in a solar power receiver system. According to the principle of the invention, a viewfinder (figure) acquires an image of the receiver and an image of the sun reflected off the movable heliostat. By superimposing the two images, the viewfinder detects whether an offset exists between the two images. If an offset is detected, the viewfinder determines the magnitude and direction of the offset. Then the viewfinder generates a position error signal used to re-position the heliostat to improve the pointing accuracy.
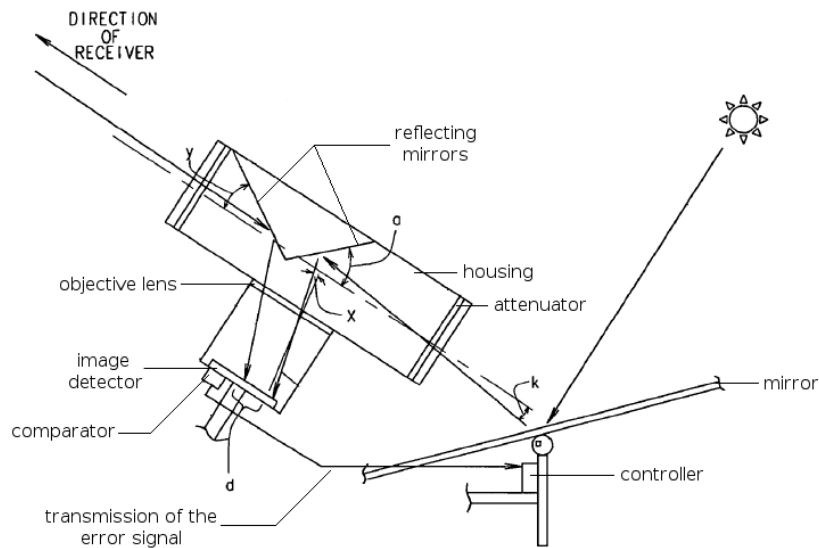
The system used to associate the viewfinder and the heliostat is not described. The location of the viewfinder associated to the time needed to align all the heliostats (during sunny days) are the main drawbacks of this system.

4.1.3.4 Heliostat with integrated image-based tracking controller (Patent US 7,906,750 B2 [125])

This patent describes a system, integrated in all the heliostats of the field, which includes an imager, a tracking controller linked to the imager, and one or more actuators connected to the reflector and tracking controller.
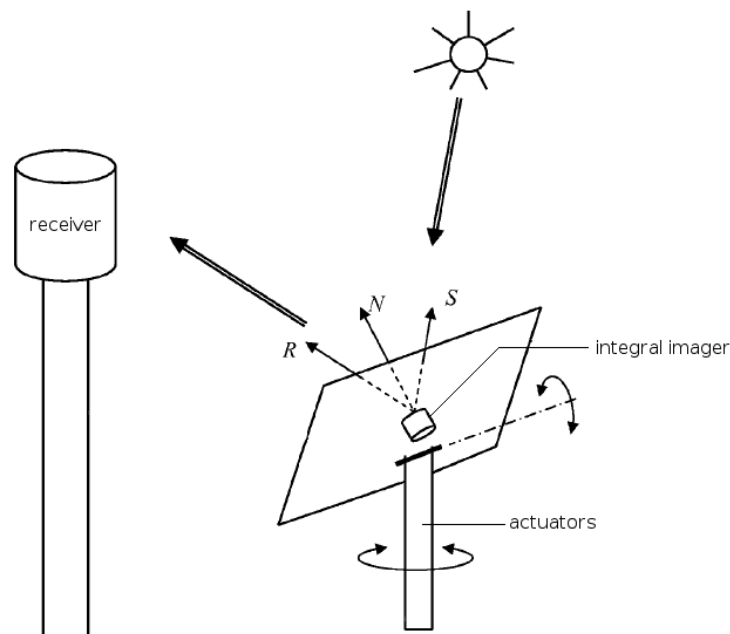
To increase tracking accuracy, the tracking controller orients the mirror based on calibrated reference points that compensates for the deviation between the heliostat normal vector and the optical axis of the imager. In the optimal configuration, the mirror normal bisects the

receiver and sun direction vectors with the receiver and sun presenting at antipodal positions with respect to the calibrated reference point.

By orienting the heliostat to maintain the antipodal relationship between the sun and the receiver, the heliostat can track the sun using a simple tracking algorithm. As each heliostat can independently execute tracking operation, there is no need of a central controller coordinating a plurality of heliostats.
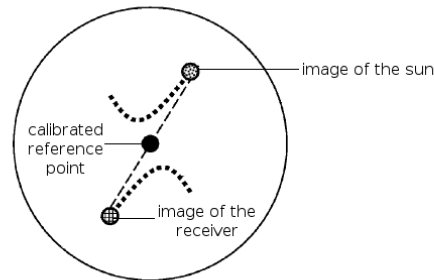
Figure A:
Mirror properly aligned

Figure B
Mirror improperly aligned
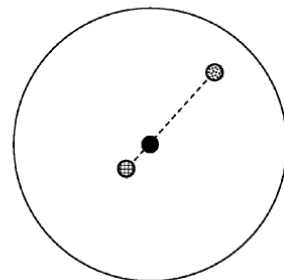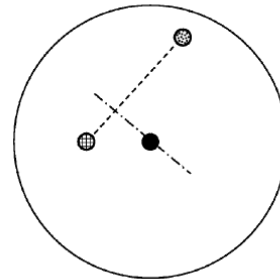
Figure C
Mirror properly aligned
only on one axis

Illustrated on the picture above, are diagrammatic illustrations of the image of the sun and the receiver acquired by the camera at various stage of tracking or misalignment. When the heliostat is correctly adjusted, as shown in Figure A, the calibrated reference point of the camera is located on the line between the sun and the receiver. The Figures B and C show cases where the heliostat is not properly aligned with the sun and the receiver, according with two or one axis. The following algorithm is used to control the field:
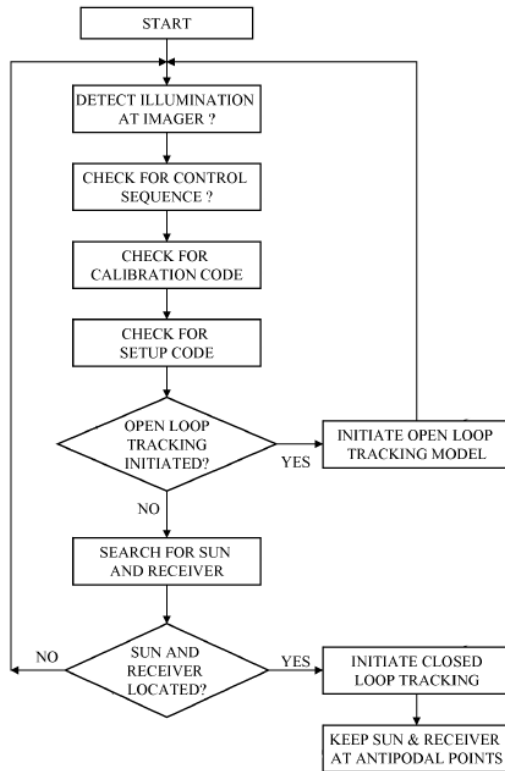
This technique requires equipping each heliostat with an imager that would result in increasing the cost of the heliostat field and the maintenance.

4.1.3.5 *System for aligning heliostats of a solar power tower (Patent US 8,344,305b [126])*

The principle is to place sensors on an off-focal area close to the focal area of the solar power tower. These sensors are linked to the heliostats and a processor interprets the communication between the off-focal sensors and the misaligned heliostats to identify the misaligned heliostat and realign it.
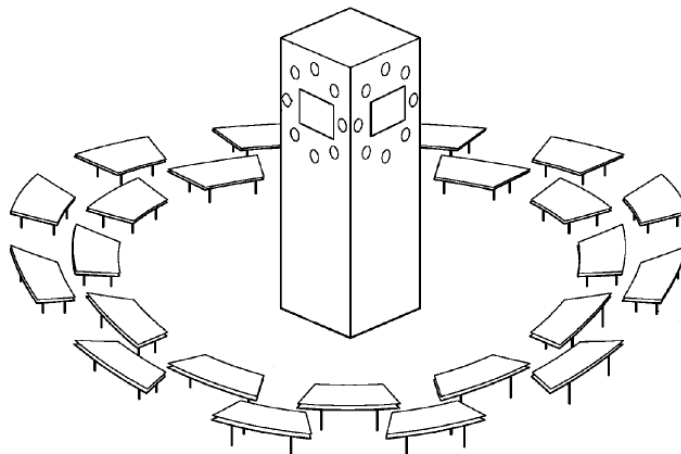
There are 2 different possible processes to identify the misaligned heliostat. The first is a binary search type algorithm: for example the processor may instruct half of the heliostats used with the common signal to modify signal transmission. If the signal detected by the sensor is not modified, the processor can determine that the misaligned heliostat is not within

that half of the heliostats. By repeating this process iteratively, the processor can determine which heliostat is misaligned and is able to correct the misalignment.
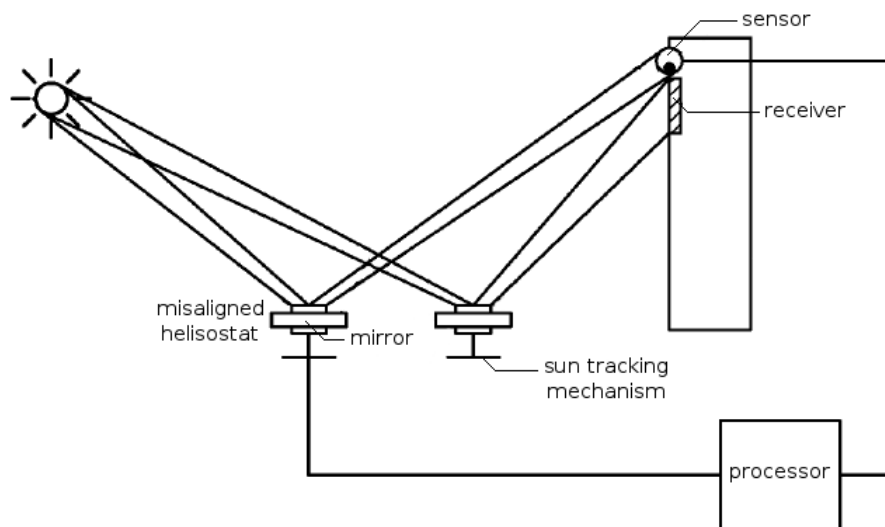
The second one consist in allocated a unique characteristic to each heliostat: for example each heliostat could include a different light filter as a reflection modification element. In this way the light reflected by each heliostat could have its own spectral response which could allow the processor to identify the misaligned heliostat. The light filter may be electrically actuated such that reflected light is filtered only when the processor actuates the filter. Another variation possible is that the processor could make each heliostat vibrate at a different frequency in a way that the processor could identify the misaligned heliostat by recognizing the frequency of the vibration of the light on the sensor. The vibration element is preferably a speaker coil that is coupled to the reflective mirror and dithers the reflective mirror at a frequency within the audio frequency range, for example between 10 hertz and 100 kilohertz.

This method uses non-imaging technique. The first process requires an iterative and time consuming step to find the misaligned heliostat. The second one results in an expensive heliostat field.

4.1.3.6   *Heliostat Control Scheme Using Cameras (Patent US 2011/0120448 A1 [127])*

This patent describes a heliostat control system based on the observation of the field by one or several camera(s) located in (or proximate to) the receiver volume.

Each heliostat is associated to an area of the captor(s), in this way the image produced by the camera include pixels having a brightness dependent on the orientation of the various heliostats. As a result, the image(s) can be used to determine errors in the alignment of the heliostats: the principle is that the computer tries to maximize the sunlight seen by the camera from each heliostat. If a portion of the image assigned to a particular heliostat does not include a spot or includes a spot that is not as bright as expected, the computer can send command to motors on this particular heliostat to adjust the mirrors in a better way.
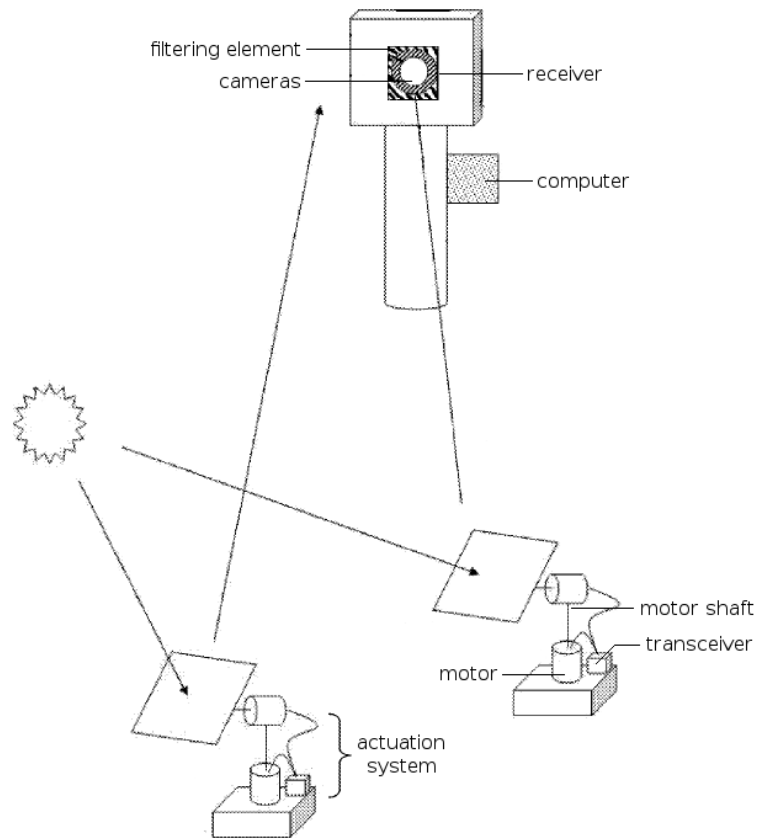
As the receiver is a hot and harsh environment, the camera needs to be protected from the heat. A cooling system can be used, for example a jacket of coolant surrounding the camera connected to an external liquid coolant circulation system. Another possibility is to use filters, placed in front of the camera which allow only light at particular wavelengths to enter the camera while keeping the majority of the thermal energy away.

The main drawback of this technique is that it should perturb the receiver operation and movable structures are exposed to high radiative fluxes.

4.1.3.7   eSolar's system

The system [128] which will be described in this section is the one used by eSolar in their demonstration plant in California.

Where other solar thermal power plants use large curved mirrors to reflect the sunlight, this field is composed of small flat mirrors. The plant consists of two adjacent modules featuring a total 24,360 heliostats. Each module is divided into two 175x95m sub-fields of 6,090 mirrors each that reflect the light onto a central thermal receiver located between the sub-fields.

Two white 5x5m target are mounted on each tower facing each a sub-fields, 36m above ground. Four GigE cameras are located approximately 150m away from the targets. They are connected to a switch linked to fiber optic cabling that get together all the cameras in the adjacent fields, and then transmits all the image data in a laboratory located 90 km away via high speed internet connection for analysis.
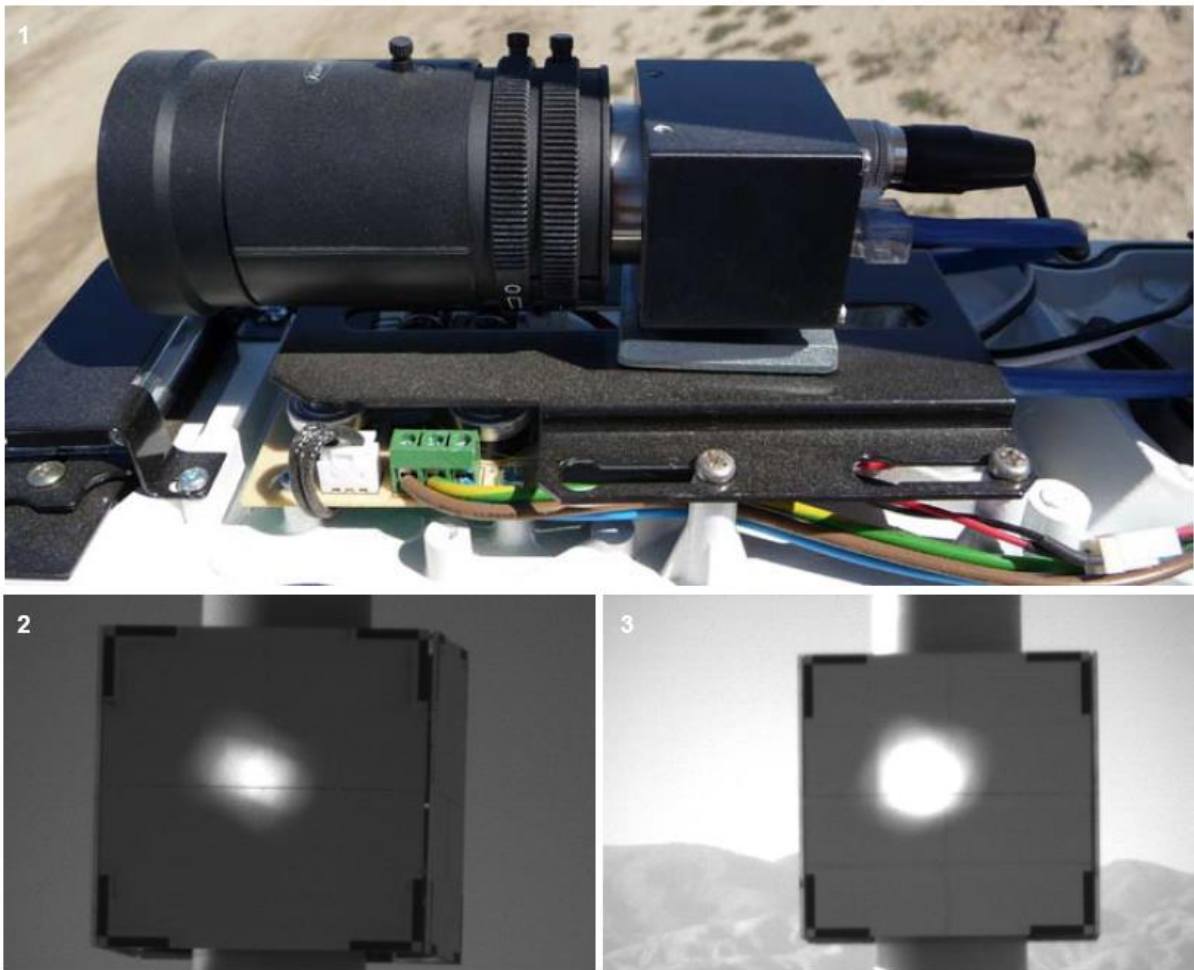
Mirrors are programmed to track and focus the sun to the center of a target. Individual frames are taken at 30 seconds intervals as various mirrors slew on the target. All imaging is software controlled. Once the system receives confirmation that a mirror is pointing at the target, an image is taken. When an image is received, the basic analysis is a centroid of the reflected sunlight compared to the center of the target. A perfectly aligned mirror will consistently reflect sunlight to the center of the target throughout the day. When a divergence is spotted, eSolar engineers update the proprietary sun –tracking algorithms to correct the mirror alignment. Camera functions controlled by software include triggering, exposure, and gain. All of these are set to provide the best image of the reflected sun. The application software was developed by eSolar's engineering team.

4.1.3.8   Determination of heliostat orientation by radar technology

An alternative (open-loop) method to determine heliostats orientation during operation of the solar thermal power plant was tested by Solar Institute Jülich and Fraunhofer Institute for High Frequency Physics and Radar Techniques in the feasibility study HelioScan [133]. The method uses a high resolution radar instead of an encoder network to control the heliostats positions during operation. The principle of the method, its testing and evaluation are described below.

4.1.3.8.1   Principle of the method

A high-resolution millimeter wave radar (KOBRA94) is installed in the solar tower underneath the solar receiver. The radar technology used is a synthetic aperture radar (SAR), the emitted radar waves have a bandwidth of 2 GHz, which leads to a resolution of 7.5 cm. The radar unit is equipped with three rectangular horn antennas, the first antenna (emitter) sends a signal with vertical polarization to the measuring scene, and the second and third antenna (receiver) receive respectively the co-polar and cross-polar reflected signal. The measuring scene consists of the heliostat field, in which every heliostat is equipped with three corner reflectors. The corner reflectors have the advantage of visibility from nearly every point of view of the radar and thus help to detect the precise heliostat position. The applied method of synthetic aperture radar (SAR) implies a relative movement between the radar and the measuring scene in order to achieve high resolution with relative small antennas. Therefore, during the measurement the radar moves linearly along a rail with a length of 1.45 m. The three corner reflectors of each heliostat are detected by the radar and their three-dimensional coordinates are calculated. Thereby the normal vector of each heliostats plane is determined and azimuth and elevation are calculated. The heliostat tracking is calculated using the obtained position information of the radar measurement and − as in current tracking systems − an astronomic sun position software. **¡Error! No se encuentra el origen de la eferencia.** shows a comparison of the principles of a conventional tracking method and the new one using radar.
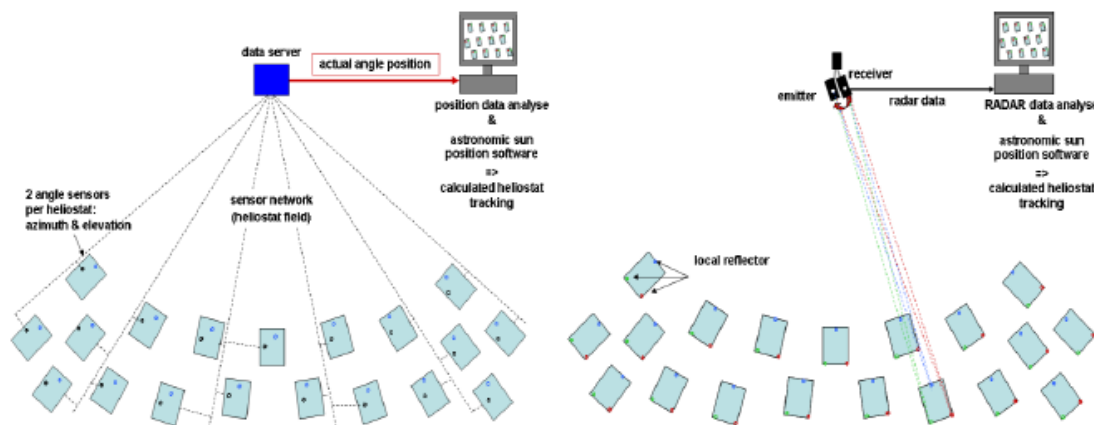

Figure 82. Comparison of a conventional heliostat tracking method using encoders (left hand side) and the new method of determining the heliostats positions using high-resolution radar (right hand side).

4.1.3.8.2 Testing and evaluation of the method

In a preliminary test, the orientation (azimuth and elevation) of the heliostat of a single heliostat, equipped with four corner reflectors, was determined in order to verify the applied algorithm in terms of accuracy. In this test, the single heliostat was turned through 360° during the measurement. The analysis of the results shows a deviation of the measured orientation from the real orientation of about 3° in azimuth and 0.3° in elevation. After the preliminary test, the measurement was applied to the heliostat field in Jülich. Several sections of about 100 heliostats with test distance between 50 and 300 m were measured in 20 sec. The thereby obtained orientations show an average deviation of 2.36° from reference values, determined by parallel tachymeter measurements in the case that all corner reflectors are detected. But restrictions are observed, because some corner reflectors are shadowed by other heliostats and cannot be detected, which leads to a lower accuracy in determining the heliostats position.

The approach points out the capability of millimeter wave radar for controlling of heliostat fields without encoders. Further optimization steps are planned to achieve a desired maximum accuracy of the method of about 2 mrad.

4.1.3.9 Close-loop heliostat tracking using an auxiliary mirror

The German Aerospace Center developed a method for close-loop tracking of heliostats using small auxiliary mirrors [134]. The principle of the method and its evaluation are described below.

4.1.3.9.1 Principle of the tracking method

In order to control the orientation of the heliostats and thereby correct the tracking error during operation, to every heliostat of the solar field a coverable auxiliary mirror is attached (see Figure 83). The mirror area is 0.09 m^2 for a distance of 500 m and respectively 0.36 m^2 for 1000 m. The deviation between the heliostat normal and the auxiliary mirror normal is fixed, so that the heliostat reflects the sunlight onto the receiver, while the auxiliary mirror reflects it onto a lambertian target underneath. To determine the actual orientation of a particular heliostat, a camera takes images of the target: a first one with the reflected spot of the auxiliary mirror and a second one without, after having covered the mirror. The second image serves as reference, which is necessary for the detection of the faint spot on the first image. By means of the images, the position of the spot on the target is determined and thereby the actual orientation of the heliostat can be calculated. Since the spot has to be related definitely to a particular heliostat, the heliostats orientation can be determined for only one heliostat at a time, covering the other auxiliary mirrors meanwhile. However, the procedure takes only a few seconds for each heliostat, so that a high reiteration rate can be achieved.
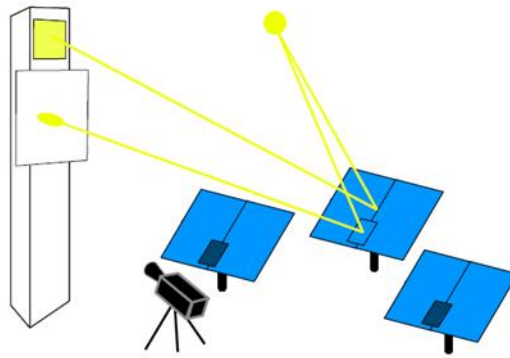
Figure 83. Basic principle of the close-loop heliostat tracking using auxiliary mirrors.

It is important for the tracking method, that once a heliostat with auxiliary mirror is erected completely, the deviation between the heliostat normal and the auxiliary mirror normal is determined. For that purpose, the heliostat has to reflect the sunlight onto the target during morning or evening hours, when the spot of the auxiliary mirror will be on the target as well. Both spots can be used to calculate the heliostat normal and the auxiliary mirror normal.

4.1.3.9.2 Testing and evaluation of the method

The described tracking method has been evaluated by simulation and the obtained results regarding the tracking accuracy have been verified in a test at the solar tower in Jülich, in order to show the applicability of the method.

In the simulation, the ray tracing software STRAL calculates the flux distribution on the target, which is then converted into a grayscale image to emulate the camera. In the calculation of the flux distribution STRAL uses a model of a single heliostat with auxiliary mirror; important error sources are included, like the azimuth axis tilt, incremental encoder inaccuracy, encoder reference errors, sun position algorithm inaccuracy and canting errors. By means of the simulated image, first of all the algorithm determines the position of the auxiliary mirrors reflection on the target. Using this information, the actual orientation of the heliostat is calculated, which is then used to correct the orientation calculation for the next tracking. In order to obtain the tracking accuracy of the method, the centroid of the flux density distribution of the heliostats reflection is compared with the actual aim point.

The analysis of the simulations shows the following results: For the heliostats in further distance to the tower, the accuracy is significantly improved by the new orientation correction method, so that these heliostats track their aim point with a mean deviation of about 0,10 to 0,15 mrad. However, the error caused by the inaccuracy of the sun position algorithm cannot be corrected, since it is smaller than the tracking accuracy achieved by the method. If an inaccuracy in the drive system exits the method improves the tracking accuracy significantly for almost all of the heliostats in the solar field. For the lateral (FL) and central (FM) heliostat in the first row, neither the inaccuracy in the drive system nor errors caused by the incremental encoders can be compensated significantly. Nevertheless, for these heliostats the method reduces the tracking error by a factor 0.8 (FL) and 0.3 (FM), if all error sources exist at once.

In the short test at the solar tower in Jülich, a heliostat and auxiliary mirror simultaneously reflect the light to the target underneath the receiver. By means of the reflection of the auxiliary mirror, the position of the centroid of the heliostat on the target is predicted and the actual position of the centroid was determined afterwards to evaluate the prediction. The results of the test verify the results gained by simulation. More tests are planned in order to evaluate the improvement of the tracking accuracy under real conditions and to compare different methods to cover the auxiliary mirror.

The results of the simulation and the short experiment indicate that the presented method of close-loop control of heliostats orientation is able to improve the tracking accuracy. However, restrictions of the method are observed due to the required target size because of the movement of the reflected spot of the auxiliary mirror on the target. Since the angle of incidence of the auxiliary mirror varies differently compared to the angle of incidence of the heliostat over the day, the reflected auxiliary mirror spot moves over the target throughout the day for a heliostat with fixed aim point. The track depends on the deviation between heliostat normal and auxiliary mirror normal, which remains fixed during operation. Nevertheless, the deviation can be optimized for each heliostat in order to maximize the time, in which the reflected spot can be detected on a target of given size. A simulation of a solar field with optimized auxiliary mirror normals shows that for the major part of the field the method can be used without or only with minor restriction, when using a big target of 30 m x 30 m underneath the receiver. For the heliostats in the back of the field, the method can be used during the whole operation time. For the heliostats close to the tower at the sides of the field there are major restrictions with this target size, so that for these heliostats the method can only be applied for a friction of operation time.

4.1.4   Conclusion

The control of a heliostat alignment needs to compare the actual alignment with a reference. The comparison algorithm was exposed and it is shared by all the systems using different techniques to detect the heliostat alignment. Several detection methods with different devices were reviewed, however most of them are only described in patent so it is difficult to obtain information about the performance and the costs: we can divide this methods in two main groups, first the methods which used viewfinders (or cameras) associated each with only one heliostat; it is possible that these methods could have a higher cost because of the number of device to buy. The second group includes the methods which use sensors and targets to optimize direction of the reflected rays. These methods should be more complex to set-up but should be less expensive.

4.2 Development of sensors and fast calibration procedures to improve heliostat tracking

4.2.1 Backward-gazing method

4.2.1.1 Introduction

A backward-gazing method has already been described by F.Henault and C. Royère in 1987 [135]. The principle relies on locating a sensor at the centre of the target plane in order to adjust the brightness distributions on the surface of the concentrators. The method was tested on the solar furnace in Odeillo and the solar power plant Thémis. However, this method did not permit to quantify accurately the mechanical errors of the heliostats due to employed photographic cameras: the detectors used were silver films. An improvement of this method was patented by the CNRS in 2015 by F. Henault and C. Caliot [136]. The idea of the new backward-gazing method is to combine the works realized thirty years ago and wavefront-sensors. Wavefront detection is widely used in adaptive optics, one of the most famous used system is the pyramidal wavefront sensor describer by Ragazzoni [137].

The purpose of the described method is to determine the heliostat's optical errors by reconstructing the slopes of the wavefront of the sun rays reflected by the concentrators. Four images of the reflected sun are taken from cameras located close to the focal volume of the heliostats, near the receiver of the power plant. The theoretical part includes the formulation of the heliostat angular errors in the camera plane. Then, the slopes of the wavefront are reconstructed using the four images and the known profile of the sun. The particularity of the method, regarding classic wavefront-sensor systems, is to use the profile of the light source in a spectral band and multiple points of view (four here) to determine the errors of the mirror.

In order to develop the method, numerical simulations have been realized to test the feasibility. Following the good results of the simulations, experiments are currently being performed at Thémis tower power plant.

4.2.1.2 Equations of the slopes of the optical errors of the heliostat

The heart of the method is to use the properties of the wavefront to reconstruct the slopes of the optical errors of the heliostat. A geometrical optics theorem, named Malus' theorem, tells that the theoretical wavefront is orthogonal to the light rays, and that this wavefront is disturbed only when the light rays are hitting surfaces (or coming through different index media, which does not happen in our case).

Let's consider the system presented in Figure 84. The only element disturbing the wavefront coming from the sun is the heliostat. It is now possible to define the two functions Δ and W: Δ is defined in every point M of the heliostat as the difference between the ideal shape of the heliostat and its actual shape, and W is defined in every point P of the wavefront as the difference between the ideal shape of the wavefront and its actual shape. Malus' theorem gives also a relationship between Δ and W:

$$W(P) = 2\cos(i)\,\Delta(M) \tag{1}$$

(in two dimensions).

A second important relationship is the Nijboer formulas [138]:

$$x' = D \, \frac{\partial W(P(x,y))}{\partial x} \qquad\qquad y' = D \, \frac{\partial W(P(x,y))}{\partial y} \qquad\qquad (2)$$

Where D is the distance between the heliostat and the receiver.
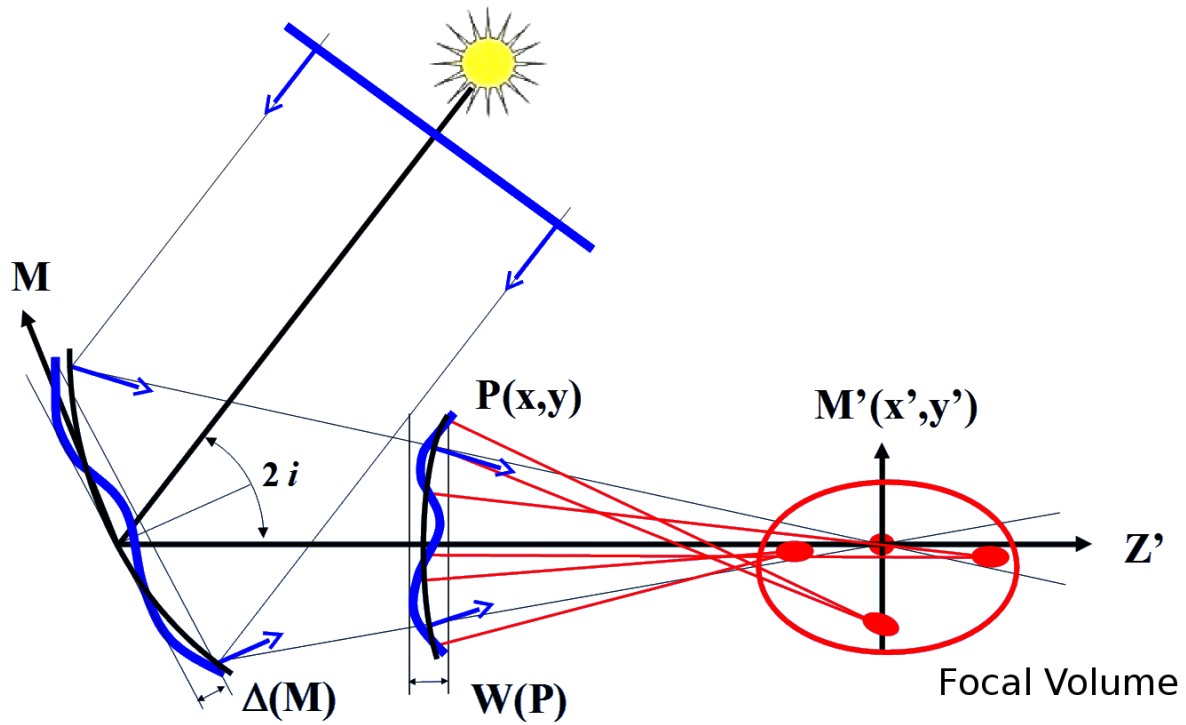
Figure 84. Wavefront and functions Δ and W.

The set-up of the backward-gazing method is presented on the Figure 85. Images of the reflection of the sun on the heliostat are taken from four different points of view. By knowing the sun profile, it is possible to reconstruct the optical errors of the mirrors Δ in every points P of the heliostat.
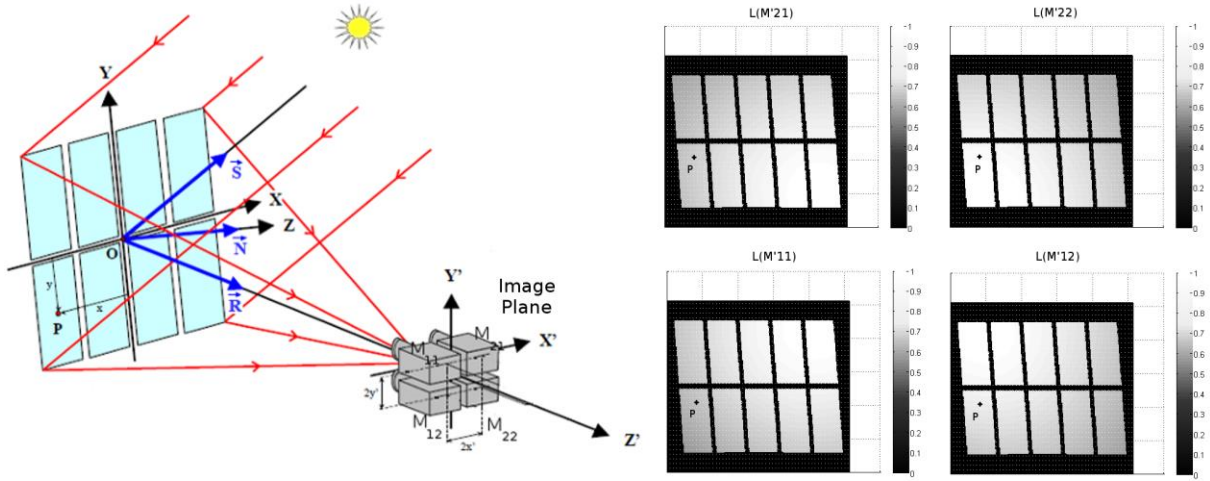
Figure 85. Set-up of the Backward-gazing method.

Using the two equations (1) and (2), and the angular profile of the sun $L(\alpha, \beta)$, the following relationship can be written:

$$\frac{\partial \Delta(P)}{\partial x} = C_x \times f\,[L(\alpha, \beta), B(M'_{22}, P), B(M'_{21}, P), B(M'_{12}, P), B(M'_{11}, P)]$$
$$\frac{\partial \Delta(P)}{\partial y} = C_y \times f\,[L(\alpha, \beta), B(M'_{22}, P), B(M'_{21}, P), B(M'_{12}, P), B(M'_{11}, P)]$$

(3)

Where $B(M'_{ij}, P)$ are the brightness at a point P of the heliostat on each of the four images, and C_x and C_y are constants depending on the distance between the heliostat and the receiver, and the distance between the cameras. For some specific configuration and sun profiles, analytic expressions can be obtained for the equations (3).

4.2.1.3 Numerical simulations

In order to validate the four-camera backward-gazing method, numerical simulations have been realized on heliostats with different configurations. In this section, the numerical model and the results are described.

The brightness profile of the sun is chosen as super-Gaussian, depending on two parameters ξ and τ:

$$L(\alpha, \beta) = L_0 \exp\left[- \left(\frac{\sqrt{\alpha^2 + \beta^2}}{\tau \varepsilon_0} \right)^\xi \right]$$

(4)

Where ε_0 is the angular radius of the sun (about 0.26°), ξ the power of the super-Gaussian law, and τ a size scale factor. This profile has been chosen for the possibility to adapt the equation to real sun profile. In the following numerical simulations, the sun radius is taken equal to $\varepsilon_0 = 16$ arcmin, and ξ and τ to 4 and 1 respectively.

The software used for the optical design of the heliostat and the ray-tracing simulation is COSAC (Calculs Optiques Simplifiés pour Analyse de Combinaisons), developed by

François Hénault in FORTRAN 77 programming language. The simulated heliostat is a spherical heliostat with ten facets (see Figure 30). The distance between the heliostat and the receiver is equal to the focal length of the heliostat (200 m). Alignment errors ranging between -2 and 2 mrad are introduced on the different facets of the heliostat. The last parameter to adjust is the distance between the cameras. This optimal value for δx' and δy' depends on the nature of searched errors. Finally, the distance is set to δx' = δy' = 20 cm.
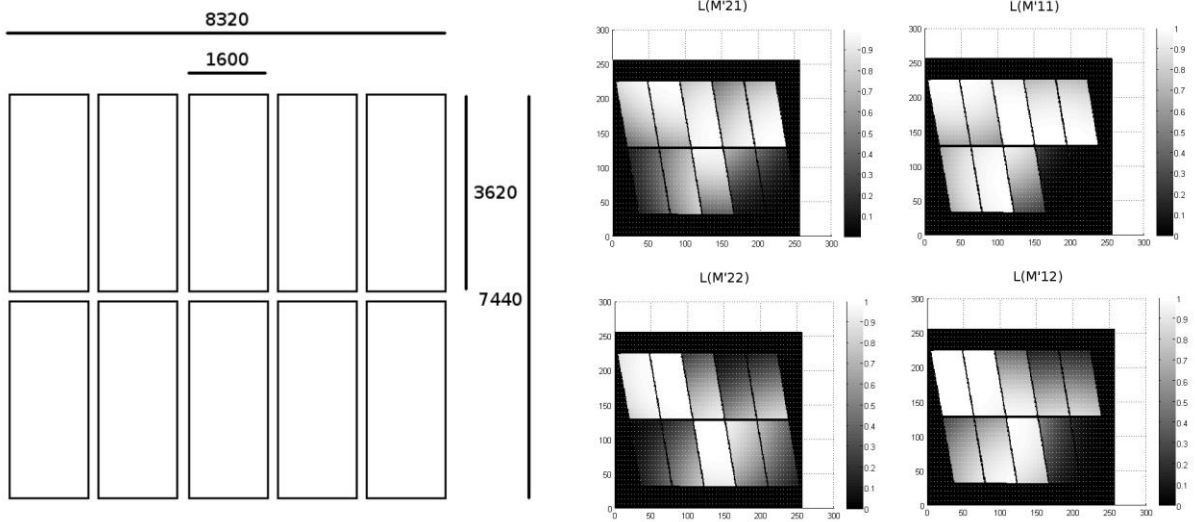
Figure 86. Dimensions of the simulated heliostat and examples of brightness images obtained with COSAC.

All the simulations presented below were realized for two different configurations of a sun-tracking heliostat:

- First case: the heliostat is tilted by azimuth and zenith angles *A* and *H* equal to 100 mrad (moderate solar incidence).
- Second case: *A* and *H* are equal to 15°.

4.2.1.3.1 Facet alignment errors

Over a first phase, the backward-gazing method had been thought for the study accurate characterization of the alignment errors of the facets of heliostats, in view of periodic readjustments of the mirrors. According to this statement, the following procedure was used:

- Azimuth and elevation alignment errors δa_k and δh_k are introduced on each facet of the heliostat.
- Analytic expressions of the equations (3) established with the sun profile (4) are used for the reconstruction.
- For each facet (k ∈ [1 ,10]), $\delta' a_k$ and $\delta' h_k$ are defined as the averaged values of $\frac{\partial \Delta(P)}{\partial x}$ and $\frac{\partial \Delta(P)}{\partial y}$.

The results of these numerical simulations are presented in the Table 6 for the less favorable second case only. The measurement accuracy obtained is around 0.04 mrad RMS, which is compatible with the typical errors observed on segmented concentrating surfaces.

Table 6. Measurement of facet alignment errors for $A = H = 15°$.

Facet n°	δa_k / δh_k (mrad)	$\delta a'_k$ / $\delta h'_k$ (mrad)	$\delta a'_k$ - δa_k / $\delta h'_k$ - δh_k (mrad)
1	-2/2	-2.05/1.92	0.05/0.08
2	-1.5/1.5	-1.52/1.46	0.02/0.04
3	-1/1	-1.00/0.99	0.00/0.01
4	1.5/-1.5	1.46/-1.48	0.04/0.02
5	2/-2	1.93/-1.98	0.07/0.02
6	2/-2	1.96/-2.03	0.04/0.03
7	1.5/-1.5	1.50/-1.53	0.00/0.03
8	1/-1	1.00/-1.04	0.00/0.04
9	-1.5/1.5	-1.52/1.45	0.02/0.05
10	-2/2	-2.07/1.95	0.07/0.05
Measurement error		PTV (mrad)	0.14/0.13
		RMS (mrad)	0.04/0.04

4.2.1.3.2 Wavefront reconstruction errors

It is also important to evaluate the performance of the backward-gazing method on the full surface of the heliostat, in terms of local errors slopes.

In the following simulations, the reconstructed slopes of the WFE (Wavefront errors, function W(P) of the precedent section) along two perpendicular axes generated with COSAC software, and the differences are estimated in PTV and RMS standard deviations computed on the whole optical surfaces. The obtained results for the previous misaligned heliostat under low and medium incidence angles (first and second cases) are presented in Table 7. The achieved RMS errors are respectively equal to 0.02 and 0.03 mrad for the two cases. The remaining measurement errors probably result from first and second order approximations when establishing analytic expressions of the equations (3) and (1).

Table 7. WFE and slopes reconstruction errors (misaligned heliostat).

| References values		Case 1	Case 2
Peak to Valley	X slopes (mrad)	4.15	5.06
	Y slopes (mrad)	4.16	4.99
	WFE (mm)	9.87	11.3
RMS	X slopes (mrad)	1.64	1.66
	Y slopes (mrad)	1.62	1.53
	WFE (mm)	4.30	4.32
Measurement errors		**Case 1**	**Case 2**
Peak to Valley	X slopes (mrad)	0.06	0.15
	Y slopes (mrad)	0.08	0.17
	WFE (mm)	0.14	0.26
RMS	X slopes (mrad)	0.02	0.03
	Y slopes (mrad)	0.02	0.03
	WFE (mm)	0.04	0.05
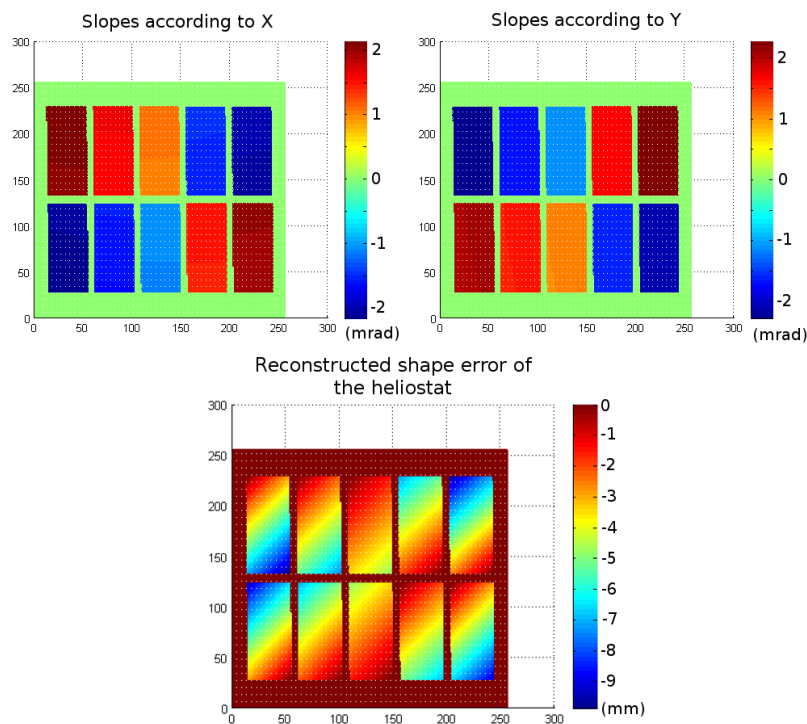
Figure 87. Reconstructed slopes and shape error of the heliostat for A = H = 100 mrad.

4.2.1.3.3 Noisy images

In experimental conditions, thermal noise can be observed on the pictures captured by the five cameras. Indeed, it is important to study the influence of this noise on the results of the method. Using the same two configurations, a white noise with 1% amplitude is added to the four images $B(M'_{ij}, P)$. As this noise could significantly damage the quality of the reconstruction on those pixels where the signal is insignificant, a threshold of 1% is applied on the four noised brightness images as a numerical filtering.

The obtained results are presented in the Table 8. These results are very satisfactory and promising. In addition, taking several acquisitions of the images with each camera instead of only one should reduce the damaging effects of the noise of the cameras.

Table 8. WFE and slopes reconstruction errors (1% white noise). same references as in Table 7.

Measurement errors		Case 1	Case 2
Peak to Valley	X slopes (mrad)	0.22	0.24
	Y slopes (mrad)	0.26	0.36
	WFE (mm)	0.70	2.70
RMS	X slopes (mrad)	0.04	0.04
	Y slopes (mrad)	0.05	0.06
	WFE (mm)	0.05	0.57

Finally, the numerical simulations demonstrate that the four-camera backward-gazing method should enable the detection of slope and shape errors, within the measurement accuracy required for solar concentrating surfaces.

4.2.1.4 Experiments

4.2.1.4.1 Presentation of the power plant, the heliostat, and the equipment

The experiments take place at the first floor of Themis power plant's tower. The geometry of the CETHEL III heliostats is particular: each heliostat is made of nine modules, eight of the nine modules are made of six parabolic-troughs facets arranged on a sphere. Then the eight modules are placed on the structure to be tangent to a parabolic shape. The ninth module is here to fill the gap left by the tracking system (see Figure 88).

In a first phase, the aim of the experiments is to test the reliability and accuracy of the method. Thus, the method will be performed on the E06 heliostat, because a photogrammetry measurement has been performed on this heliostat by CENER in 2012 (ref). These photogrammetry measures will be used as a reference to evaluate the accuracy of the backward-gazing method.

8750

7340
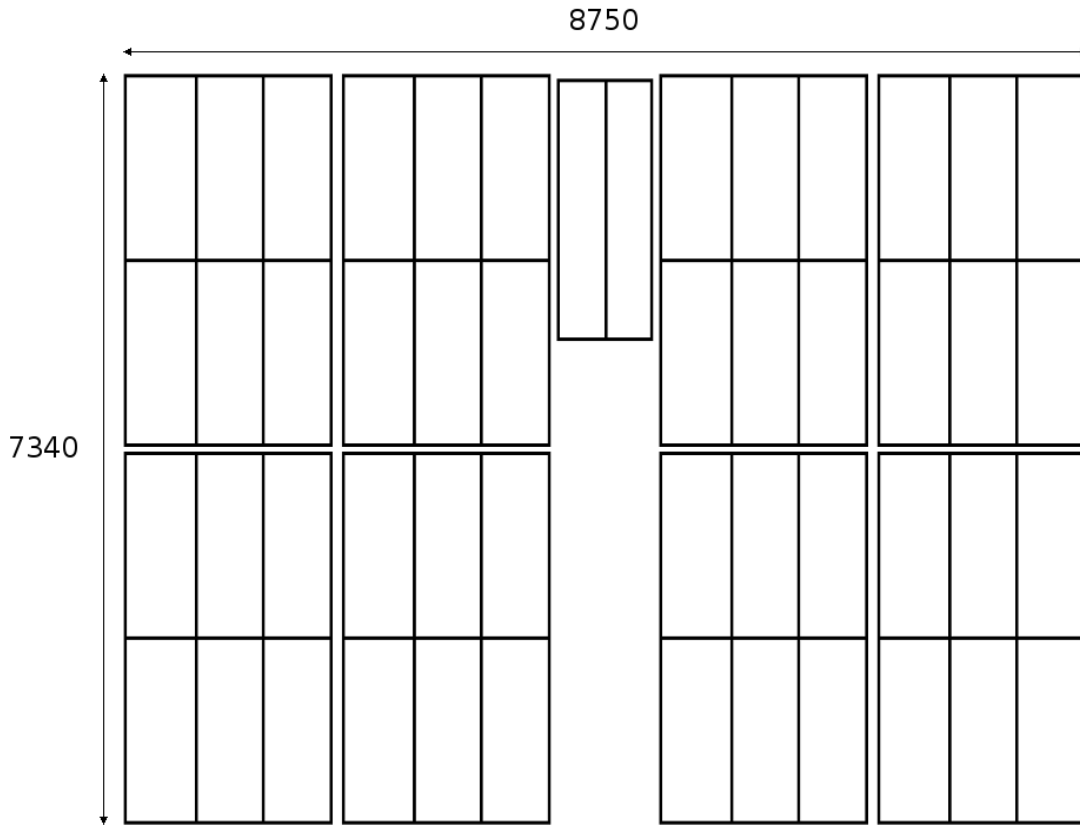
Figure 88. CETHEL III dimensions.

Heliostat CETHEL III

Themis 1st floor

Sun-tracking camera

Protecting target
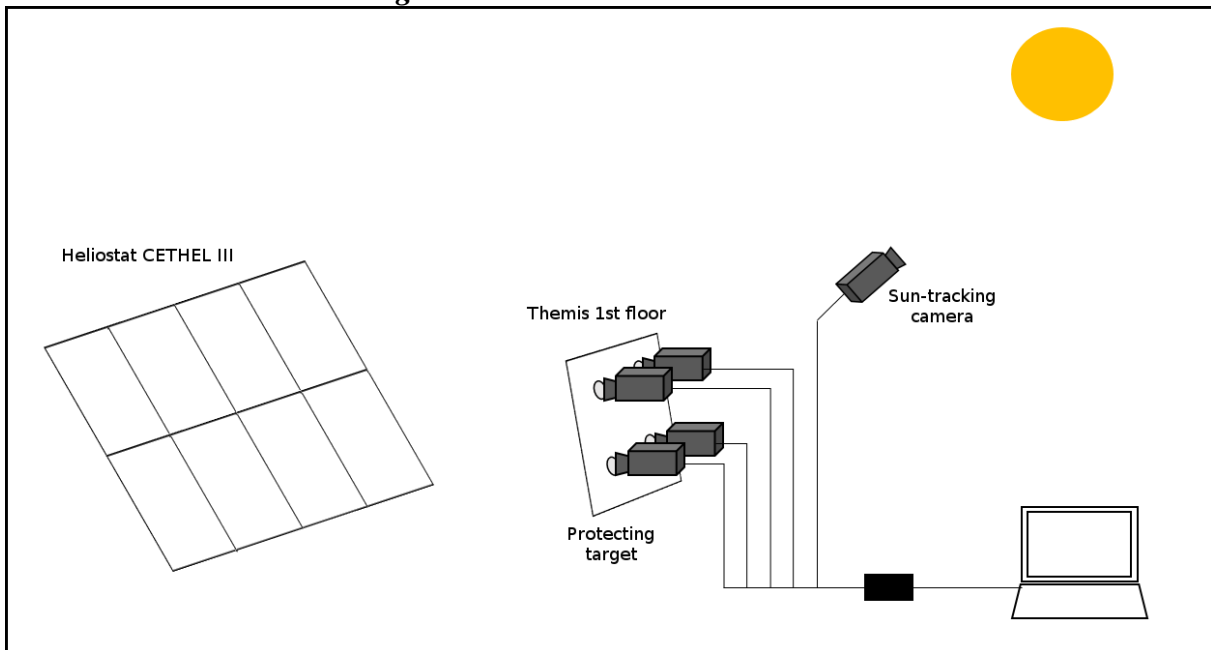
Figure 89. Set-up of the backward-gazing method.

Five cameras are used, four behind a passive target aiming at the heliostat E06, and one placed on the sun tracking device on the top of the tower.
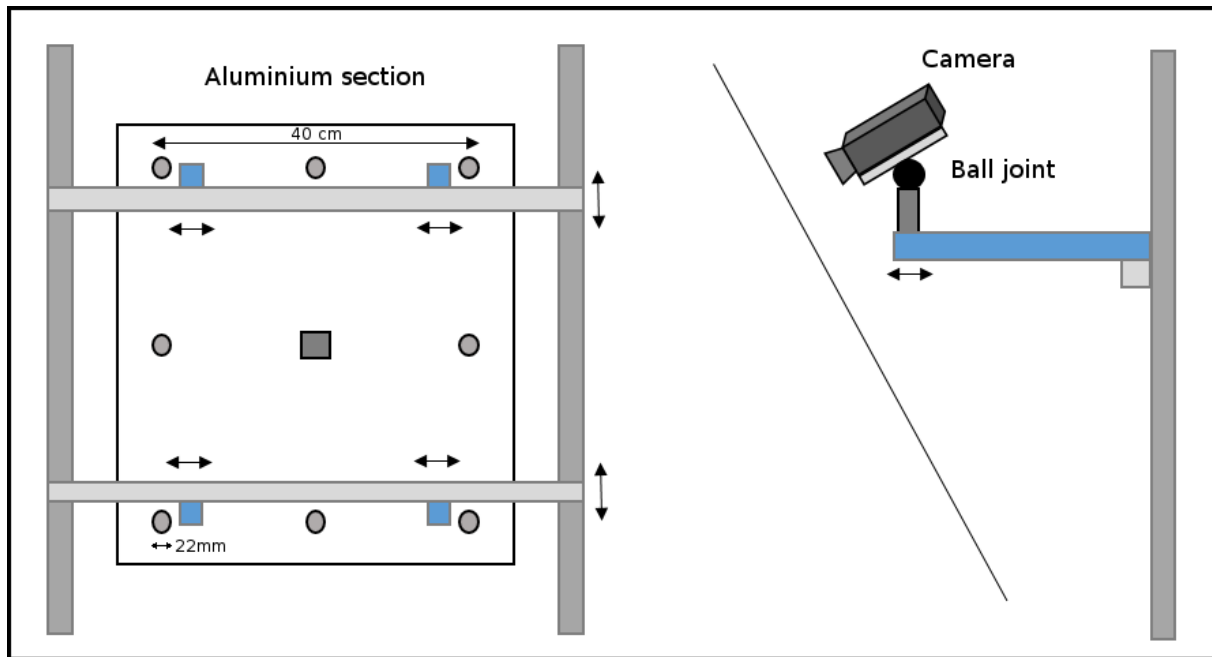
Figure 90. Fastening and orientation systems of the cameras.

An aluminum frame has been built to support the cameras. Each camera is placed on a ball joint to adjust the aiming at the heliostat.

4.2.1.4.2 Cameras

The used cameras are IDS CMOS cameras with Ethernet connections. These cameras are the same that are used at the sun-tracking system of the 1MW-CNRS solar furnace in Odeillo. Each camera is equipped with a 75 mm focal length lens with a 3.9 aperture, which permits to see a 120 m far away heliostat with about 900x900 pixels.

Figure 91. GigE IDS camera and 75 mm Tamron lens.

Several tests have been performed with these cameras in order to choose the best equipment and parameters. As results, the exposure times used during the experiments will be included between 1 and 3 ms, and two filters will be placed in front of each lens: one reflective density 3 filter and one absorptive neutral density 7 filter.
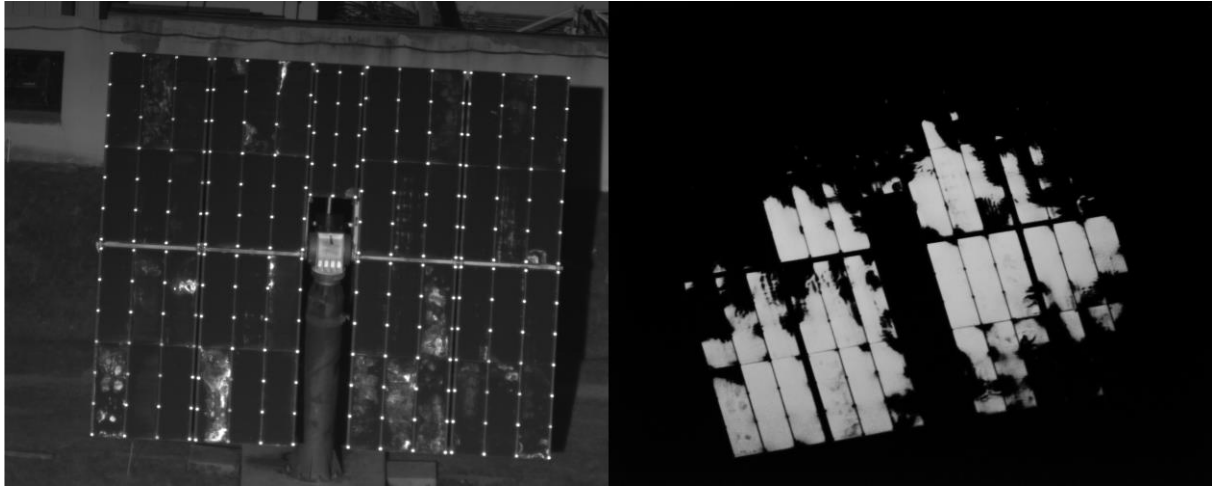
*Figure 92. Test E06 heliostat without and with the sun reflection.*

4.2.1.4.3 Calibration

The pictures taken by the five cameras could be distorted by different error sources. First of all the sensors are not perfectly uniform, each pixel has its own response which can be slightly different than others. Then, vignetting coming from the lens decreases the light on the edge of the pictures. Finally, the filters are not exactly the same, and an accurate characterization of each of them should be done.

The first and second sources of error can be corrected by flat field techniques: several images of perfectly uniform scenes are taken with the cameras, then a median is realised for each pixel, and finally a correction matrix is built for each camera.

The first step is to correct the offset: the value of the pixel when no signal is sent to the sensor. Several images are taken with the camera placed in a dark environment, with several time exposures. Hence a median is realised on these images to determine the offset of our five sensors.

In a first phase, we consider using clear dusk and dawn skies to determine the flat fields. After a few attempts, we can say that it is not a good solution for a few reasons: firstly, the sky depends on the weather, finding a uniform area on the sky is not an easy task, in addition, it is not possible to control the brightness of the sky. Indeed, another solution has to be find.

This other solution has been found in the Institut de Planétologie et d'Astrophysique in Grenoble. The tool that will be used to perform the calibration is a 30 cm diameter integrating sphere. The advantages of using such a device is the control of the brightness of sphere and the quality of the uniformity obtain (1% guaranteed). These flat fields should allow us to correct the damaging effects of the sensor and the lens.
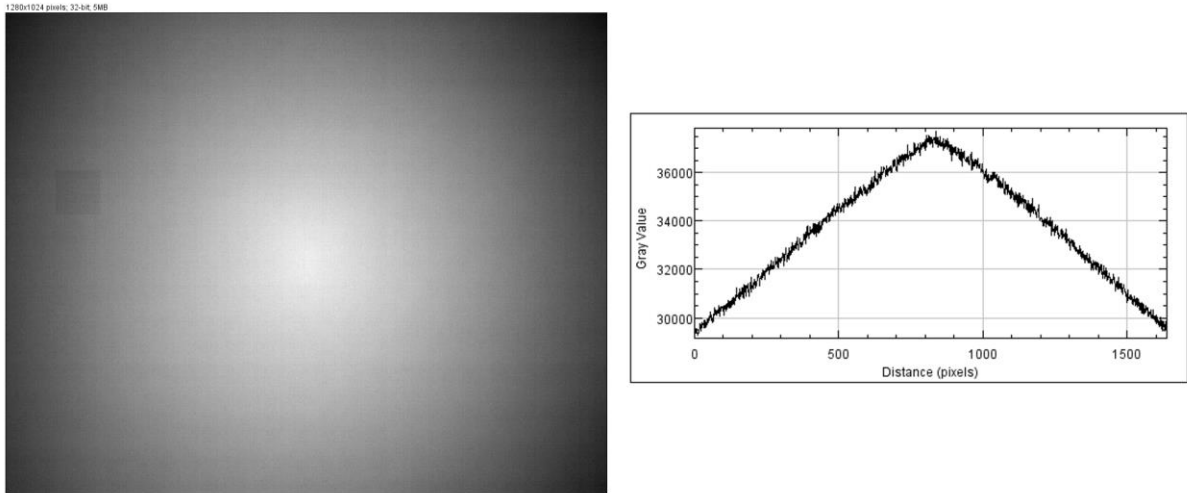
Figure 93. Flat field obtained for the first camera (median on 20 images), and a profile plot on the diagonal.

Concerning the filters, an accurate characterization of the filters is not possible with the devices available at PROMES laboratory: some filters are density 7 which is too much for the spectrometer. All we can do is performing a calibration by aiming at the sun, which is the only light source powerful enough to see with density 10 (7+3) filters. Indeed, the following set-up is used: the five cameras, with all mounted filters, are placed on a sun-tracking device, the cameras simultaneously take a picture of the sun, and a correction factor is calculated for each camera, to correct the difference between the values of the density of the filters. Unfortunately, we have to make the hypothesis that the uniformity of the different filters is negligible, given that we do not have a mean to quantify this phenomenon.

The results are presented in the Figure 94. All the images presented are corrected from the offset of the pixels and the vignetting of the lens. The Camera 5 is chosen as a reference for this camera is aiming directly at the sun. The calculated correction factors are presented in the table of the Figure 94.
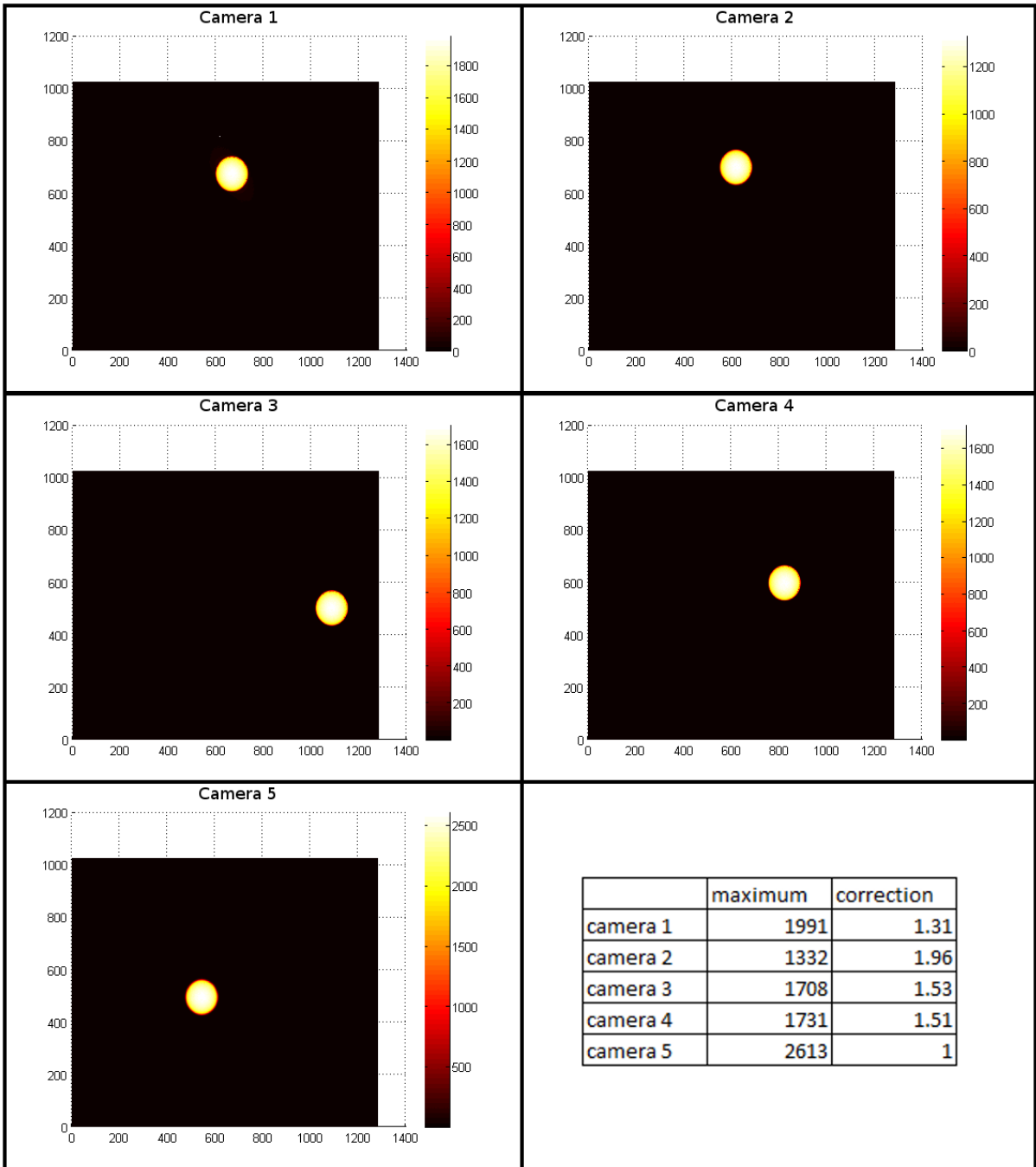
Figure 94. Images of the sun realized to correct the difference between the filters.

4.2.1.4.4 Acquisitions

The acquisition has been performed on the 8th December 2016. Once all the cameras have been adjusted to correctly aim at the sun and E06, the heliostat have been manually directed to aim at the center of the four cameras, and was then set in automatic tracking mode. Several acquisitions have been realized for different time expositions and different number of images. The set-up is presented on the picture in Figure 95: the cameras and the flux meter are placed behind a passive target at Themis first floor (75 m high). The computer is able to take about ten images per second (all cameras included), indeed, the four cameras aiming at the heliostats take the pictures first, then the fifth camera take the pictures of the sun.
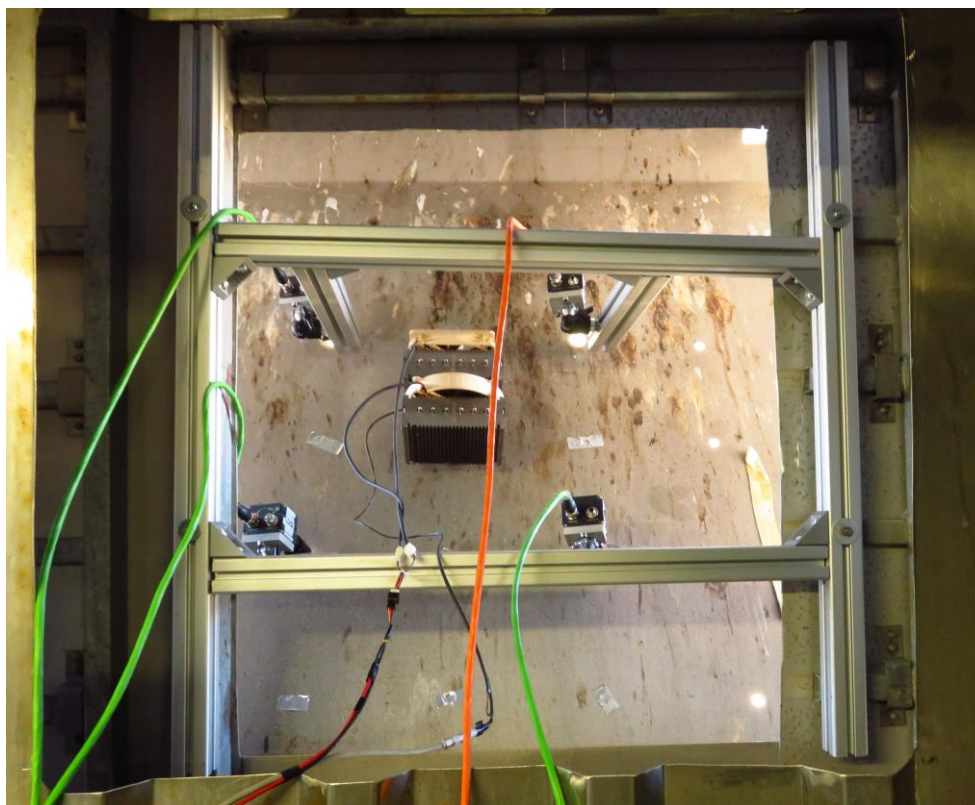
Figure 95. Set-up with the 4 cameras and the Flux meter.

One thing that has to be noted on the Figure 96 is that the areas where the sun is reflected on the heliostat don't cover the entire surface of the mirrors. It is sufficient if we only want to know the global orientation of the heliostat. However, if we want to obtain more accurate information about the local slopes and the orientation of all the facets, additional acquisitions are needed, at different moment of the day. For the E06 heliostat, the ideal time of the day is around 11. pm, when the alignment of the sun, the heliostat and the receiver is the closest to a straight line.
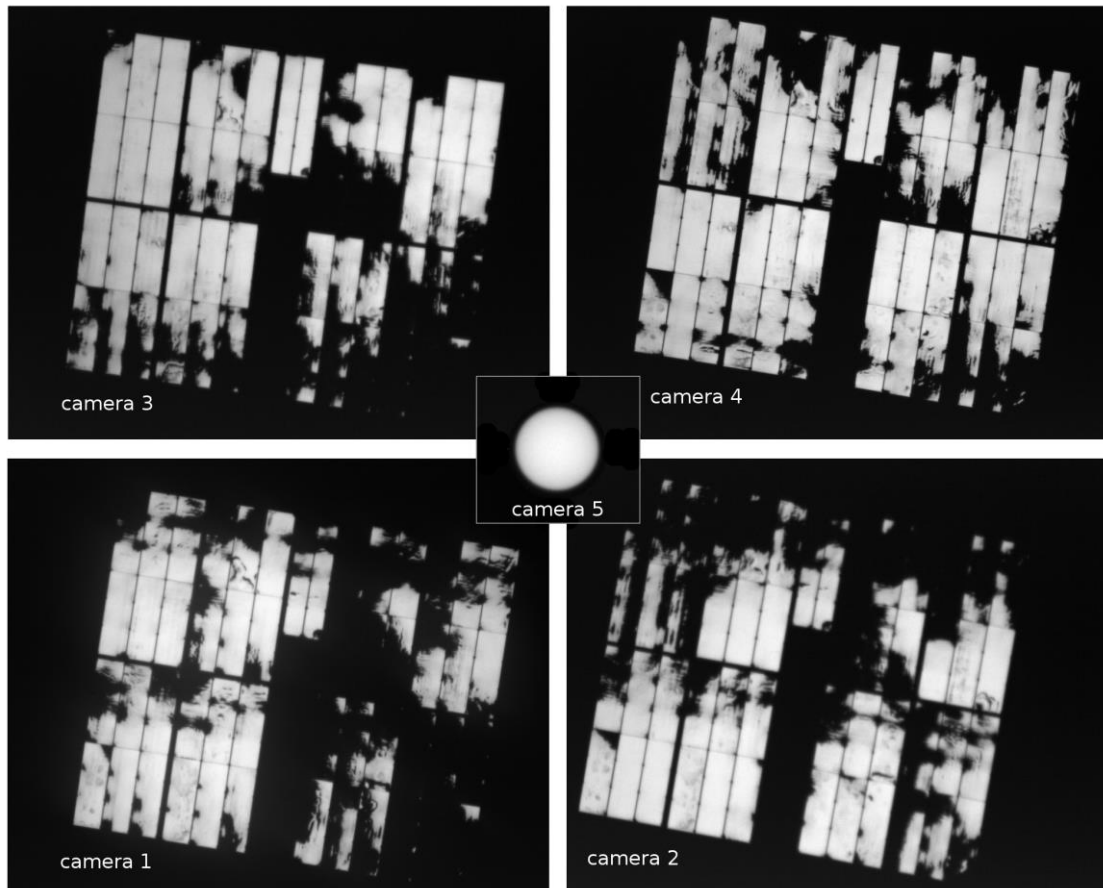
Figure 96. 5 images by the 5 cameras.

4.2.1.4.5 Image processing necessary before the slope reconstruction

The raw images taken by the cameras cannot be used without some modifications. At first, the errors due to the sensor, the vignetting of the lens and the difference between the density of the filters have to be corrected. These corrections have been explained in the calibration section.

Once the calibration has been done, geometric corrections have to be realised to overlay the four images. The superimposition is realised in two steps: first the heliostat are transformed into a rectangle whose edges are parallel to the image's edges. For this first step, affine transformations, line detections and cross correlation with horizontal and vertical lines are used. Finally for the second step, an image is chosen as a reference, then an edge detection is performed on all the images, and cross correlation is realised to superimpose the edges. The results of these operations are presented on the Figure 97.
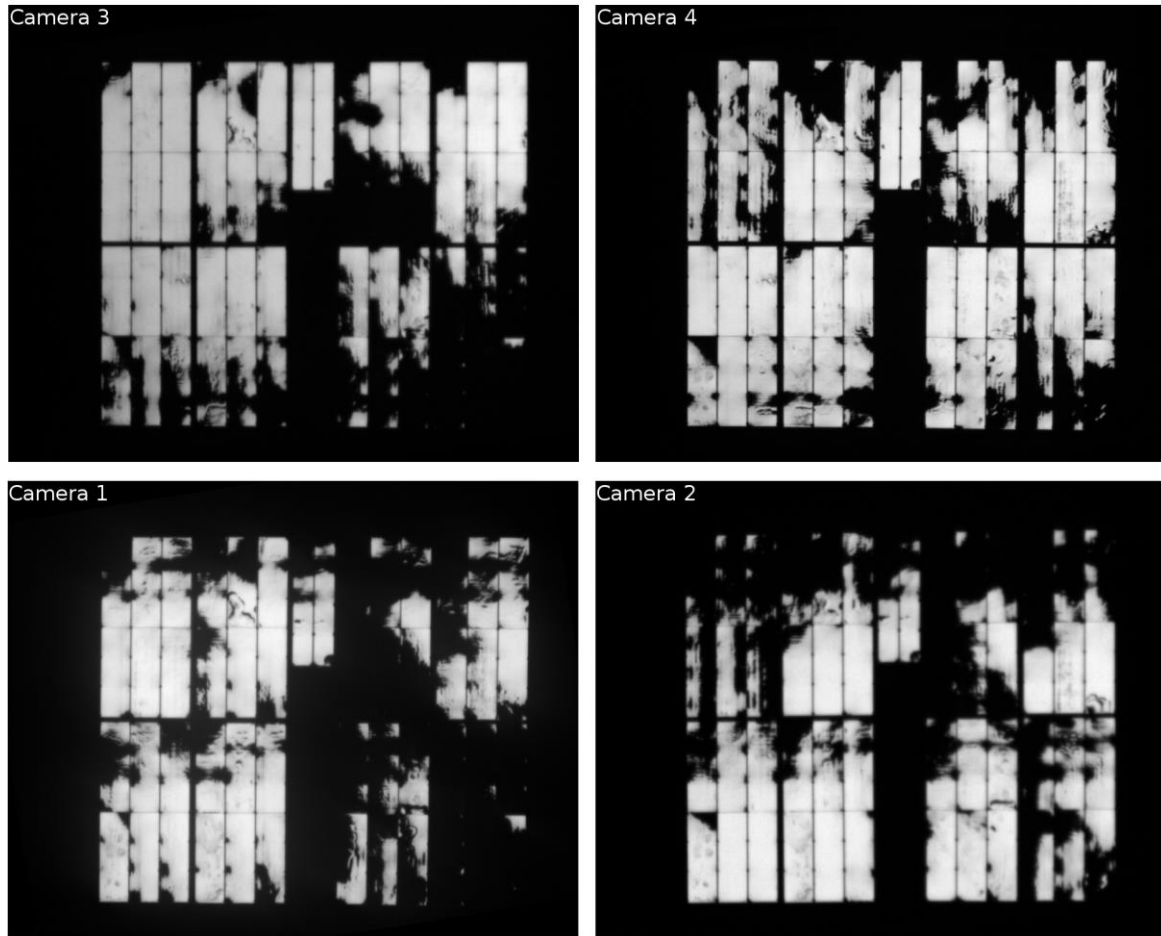
Figure 97. Superimposition of the images.

4.2.1.5 Summary and Outlook

A backward-gazing method for determining and classifying the optical errors of solar concentrating surfaces has been proposed and described. Numerical simulations applied to the focusing heliostats of a solar tower plant demonstrated that this method should enable the detection of their shape errors within the accuracy compatible with this kind of applications. The main identified errors appear to be calibration errors and sunshape knowledge.

Experiments have been performed in Themis power plant. Acquisitions have been realized on the E06 heliostat, to compare the results of the reconstruction with Photogrammetry references. Acquisitions on four or five more heliostats should be performed later.

The image processing treatments necessary to the reconstruction of the slope errors of the heliostat are on-going. The results and the methodology should be presented in the MS49.

4.2.2 Heliostat kinematic system calibration using uncalibrated cameras

4.2.2.1 *Introduction*

The operation of central receiver solar thermal power plants is greatly influenced by the efficiency of the heliostat field. For a given solar field layout this primarily depends on the ability to precisely reflect the sunlight onto the receiver and, therefore, achieve a high solar flux according to the aiming strategy. Such reflections require accurate knowledge of the kinematic system and position of each heliostat. Although this information is part of the heliostat design and solar field layout, due to fabrication, constructional variations or changes over the lifetime of each heliostat, it is only approximate and, hence, needs to be determined for each heliostat individually during the set-up process and periodically afterwards. Considering the decreasing size, and the increase of the number of heliostats in the field of a solar power plant, it is no longer viable to determine those parameters for one heliostat at a time during construction [140][141]. Moreover, being able to increase the frequency with which the heliostats are calibrated improves the efficiency of the plant. In this regard an automatic calibration procedure being able to determine all parameters in a fast and precise manner is of high interest [142][143].

In a previous study [144] a method using cameras attached to each heliostat which observe a series of targets with known position distributed around the solar field has been presented. The problem here is that, although, the initial calibration can easily be provided during assembly it is unclear whether the calibration will be valid throughout the lifetime of the heliostat, for instance due to lens degradation, causing the need for recalibration, requiring additional devices to be installed. This section is a summary of [139], presented at SOLARPACES 2016.

4.2.2.2 *Method*

In the proposed method each heliostat is equipped with a low cost camera, attached to the support structure. The cameras are aiming at targets placed at known locations within the solar plant. One of the advantage of the proposed calibration is the cameras do not need calibration, to avoid the limitation from [144]. In addition, no specific direction is required for the cameras (Figure 98). Not requiring alignment of the camera viewing direction with the heliostat surface normal avoids reduction of the reflective area of the heliostat, like the method in [145]. Another advantage in mounting the cameras on the backside of the surface is the protection from exposure to bad weather [146].

Figure 98. Camera mounted on a heliostat (a) Forward and (b) backward configuration.

The processing of the images and the estimation of the kinematic system is performed locally on each heliostat, which involves that the local control system needs to have greater computational power than what is usually required for a heliostat. Considering the increasing computational power of even very small microcontrollers, this does not cause a significant cost increase. The decision of a local processing is also influenced by the desire for autonomous heliostats and the lack of a reliable high speed transmission between each heliostat and the central control. As each heliostat is equipped with a camera and control system the calibration itself can be done independently for each heliostat and, therefore, facilitates calibrating a large amount of heliostats in parallel.

A calibrated camera allows calculating the 3D direction vector corresponding to each pixel position of the image, meaning that the vector pointing at a target, if detected, can be calculated. This constrains some of the parameters of the kinematic model. With sufficient observations this allows estimating the model parameters with high precision. However, having good knowledge of the intrinsic camera calibration is somewhat problematic: a calibration estimated during fabrication or assembly of the heliostat will eventually become inaccurate over the lifetime of the heliostat due to degradation effects in the lens system [146]. Recalibrating the cameras is not easily done as it generally requires special calibration primitives covering large parts of the camera field of view to precisely estimate the non-linear distortions. In order to avoid these problems the presented approach does not require knowledge of the intrinsic calibration parameters of the camera. To overcome the inability to simulate a projection of a spatial point into image coordinates, the targets are required to always be captured at a specific image position (u, v). In order to do so, once a target is detected anywhere in the captured image, the heliostat is moved until the target is observed at the desired image position.

4.2.2.2.1 Targets

It is not necessary that each camera can observe all the targets. Allowing each camera to see a target with a significant motion in both directions is sufficient. The targets must be placed in the field taking this into account. In order to keep the amount of required targets low, they

should be placed on top of poles slightly higher than the heliostats or the central receiver tower, in order to be visible for a large amount of heliostats without causing notable shading during plant operation. Remote controlled artificial light sources emitting light in the infrared spectrum can be used to facilitate the detection, and to enable the procedure to be performed with strong sun light. By complementing this with a band pass filter on the cameras, the targets are easily detected by simple thresholding of the captured image.

To further enhance the detection process and avoid false positives, two images of the target can be captured at each position: the first one with the light disabled and the second one with the light enabled. This way, simple subtraction of the two images and thresholding the difference gives good results with only little computational requirements. By using spherical light sources, the actual centre of the target can be determined by simply calculating the centre of gravity of the detected blobs or simple shape fitting [146]. Altogether this allows for a subpixel accurate detection of the targets in the camera image, which is essential for good calibration results.

4.2.2.2.2 Kinematic system

Limiting the optical losses of a solar field requires an accurate model of the kinematic system of each heliostat and its position within field. Such a model allows predicting the orientation of each facet as a function of the drive system values. By mean of inverse kinematic this model can be used to calculate the required encoder values for both axes for reflection of the sunlight corresponding to a given time and aiming point. Such a model should include at least the following parameters: heliostat position and orientation, axes positions and orientations, facet position and orientation. These parameters together form the kinematic chain as shown in Figure 99a) for an azimuth − elevatio configuration.
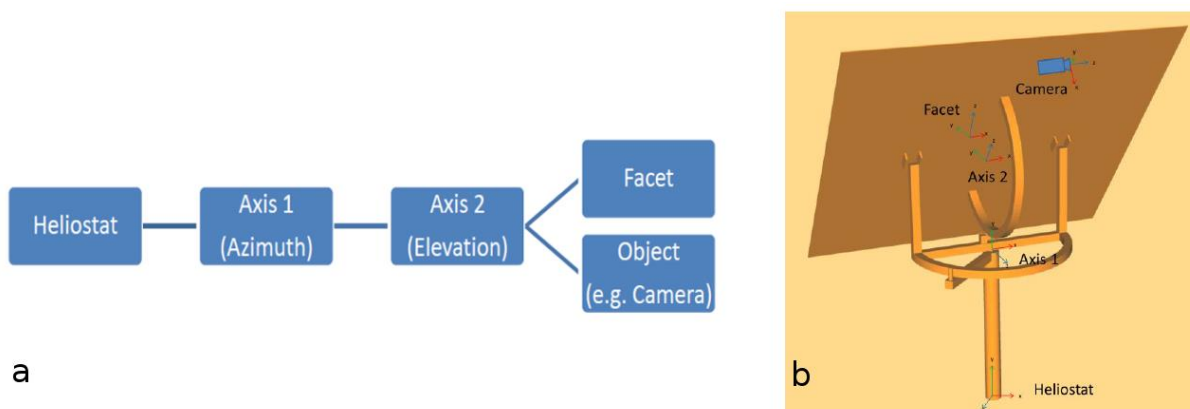
Figure 99. a) Kinematic chain of the heliostat system b) Kinematic model of the heliostat.

The calibration of the solar field is done by determining the kinematic parameters for every heliostat in the field. Some could be taken from the design or determined once during construction, like for instance the relative positions between the two axes. Also, not all parameters have the same impact onto the beam accuracy. Errors in the orientations of the axes lead to large errors, whereas the heliostat position itself has only little effect onto the reflected beam.

4.2.2.3 Results

4.2.2.3.1 Evaluation of the method

For the evaluation, the method has been applied to synthetic and real data and simulations have been done with perfect and noisy input data. The calibration is applied to a heliostat and camera with a set of predefined parameters. The heliostat and camera are then used to generate the input data, i.e. calculating the angles to observe a target at a specific pixel location (for a real scenario this process would be done in an iterative fashion, changing the orientation of the heliostat until the target is imaged at the desired location). This process is repeated for four different targets captured at five different pixel positions resulting in 20 observations used for calibration. Before calibration the position of the heliostat is shifted approximately 0.5 m and its axis orientations around 10 °. To evaluate the calibration result we do not compare the parameters of the heliostat directly as some of them are correlated with each other, meaning that a valid calibration can be reached for different combinations of parameters. Especially for noisy input data, a direct comparison can fail although the calibration might be very good. Due to this reason, the calibration results are compared based on aiming errors and their angular deviations. In order to estimate these errors, the resulting heliostat parameters are used to calculate the angles to reflect sunlight for different sun positions onto a target. Using the true heliostat parameters, the distance of the reflected ray from the aiming point and the actual angles required to reflect the sunlight onto the aiming point are calculated. The distance and angular difference between estimated and required angles serve as an indicator of calibration quality, which is also independent of the actual heliostat model.

For perfect input data, the errors are in the order of machine precision, however, in reality different effects cause errors in the input data. Considering that the targets have to be spread out over the full size of the solar field, it becomes difficult to measure their exact positions with high accuracy. For the heliostat, the axes values are not only subject to the precision of the encoder but also depend on the play of the gear and any other non-repetitive error. If the heliostat has to be moved around in different directions in order to capture the target at a specific pixel location, the play of the gear affects the reported axes values. Lastly the image quality of the image processing is also an important factor: Assuming that a target is captured at a specific pixel position requires that the image processing algorithm is capable of determining this position with very high accuracy. However, due to noise and variations in illumination this detection is subject to a slight randomness, causing an additional angular error. Assuming a camera with a few megapixels and a lens with a practical focal length, the angular error between two neighboring pixels can be estimated to around 0.2 mrad. This also shows that observing an object with known location gives rise to a very precise estimation of the orientation of the heliostat, which could be exploited for closed loop tracking. The accuracy of the target positions is assumed to be around 0.1 m. Table 1 shows the expected accuracy results for a heliostat at 1 km distance to the receiver and different uncertainties in the measurements. Each of the simulations has been repeated 100 times in order to gain a stable statistic.

Table 9. Results from simulated calibrations with different measurement uncertainties added for a heliostat at 1 km distance to target.

Input data error	Aiming RMS Error [m]	Angular RMS Error [mrad]
Target ±0.1 m	0.4	0.26
Axes ±0.1 mrad	0.4	0.2
Axes ±0.2 mrad	0.7	0.45
Axes ±0.3 mrad	1.2	0.7
Target ±0.1 m / Axes ±0.1 mrad	0.6	0.36
Target ±0.1 m / Axes ±0.2 mrad	0.7	0.4

Besides the simulation, the procedure has been applied to actual measured data. For this, a number of targets have been used and their positions measured using photogrammetry [149]. As not enough suitable light sources were available coded markers [150] as well as natural targets have been used (Figure 100). The heliostat consists of a two axis driving system equipped with a camera. The heliostat is then oriented to capture nine targets at five different pixel positions (centre, top-left, top-right, bottom-left, bottom-right), whereas each target is detected within 0.5 pixels of the desired location. The target detection has an estimated accuracy of less than 0.3 pixels. For calibration, only five of the targets are used, the rest is used for evaluation. The only initial heliostat parameter is an estimation of the heliostat position with an accuracy of around 0.5 m. During calibration the following parameters are estimated: heliostat position and orientation, both axes orientations and camera position. As mentioned before the camera orientation is not needed in this approach.
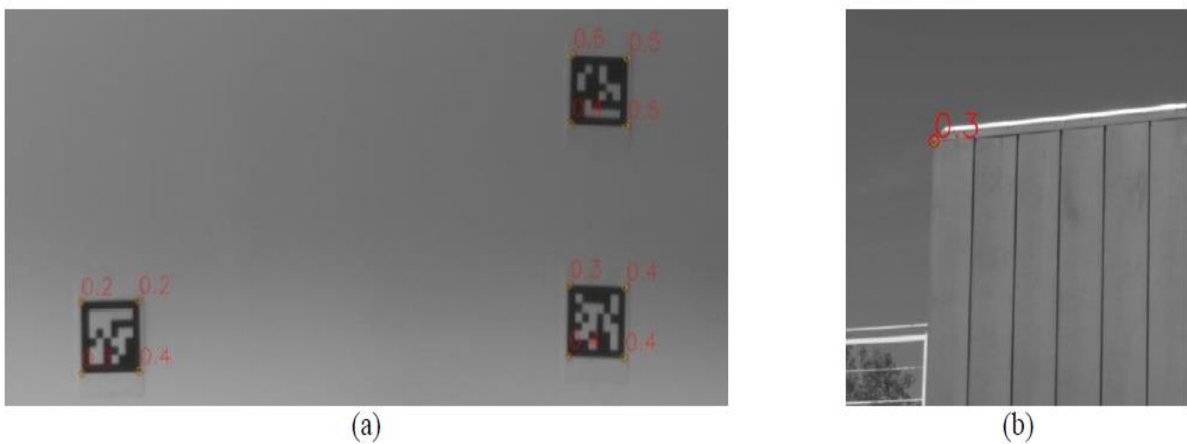

Figure 100. Overlay of detected and re-projected target positions for a) coded markers and b) natural targets with their angular error in mrad between measurement and calculation.

After performing the calibration, the resulting model is used to estimate the angles required to capture the unused targets at the five different pixel positions. These values are then compared with the actual values giving the results shown in Table 10. The results show that the method is capable of estimating the kinematic system of a heliostat with good accuracy and considering the results from Table 9 is also relatively resilient to noise.

Table 10. Calibration results for actual data.

Number of targets used	Max Error [mrad]	RMS Error [mrad]
5	0.8	0.5
9	0.5	0.3
5	0.8	0.5

4.2.2.3.2 Comparison with calibration methods based on the same principle

The results have also been compared to other calibration methods, namely the ones described in [144], which only differs from this approach in using a calibrated camera, and [142], which uses cameras to capture the reflection of targets located in field by the heliostats. In order to evaluate the stability of each method under noisy input data, similar levels of noise have been added.

The method in [144] has the same error in the target positions and a detection error for the target pixel position is added. On the other hand, as the targets do not need to be detected at specific image locations, the axes noise can be assumed slightly smaller.

For the method in [142], the target and camera position noise can be assumed to be the same. The axes error is composed of two factors: mechanical errors (e.g. encoder) and detection error. The detection error is related to the part of the reflective element which actually reflects the target. Ideally it would always be reflected at the same location, for instance the centre or the top of the mirror; however, at larger distances it becomes very difficult for an image processing to assure this and, hence, the target will be reflected from a different location. In order to see the reflection of a target at a different position on the mirror a different orientation of the mirror is required, causing an error. For a heliostat at 1 km distance, reflecting at 10 cm distance to the desired point on the mirror corresponds to a 0.1 mrad difference in the orientation of the mirror.

Performing simulations according to these errors leads to the results shown in Table 11.

Table 11. Results for a calibration according to [142] and [144] and comparison to the presented method.

Input data error	Aiming RMS Error [m]	Angular RMS Error [mrad]
[144] Target ±0.1 m	0.09	0.06
[144] Axes ±0.2 mrad	0.14	0.1
[144] Pixel ±0.5 pixel	0.21	0.16
[144] ±0.1 m / ±0.2 mrad / ±0.5 pixel	0.27	0.2
[142] Target ±0.1 m	0.2	0.1
[142] Axes ±0.2 mrad	0.9	0.7
[142] ±0.1 m / ±0.2 mrad	1.2	0.9
This: Target ±0.1 m / Axes ±0.2 mrad	0.7	0.4

The method from [144] outperforms this one, at the cost of requiring a calibrated camera, which is not easy to maintain during the lifetime of a heliostat. The method from [142] performs slightly worse but has the advantage of also estimating the orientation of the reflective surface, which requires an extra step in the presented approach. Considering, however, that if the camera is rigidly attached to the reflective surface, this step only has to be carried out once. By reflecting the sun onto a separate target, similar to the method described in [141] this relation can be estimated easily during construction.

4.2.2.4 Conclusion

The method which has been described allows the parallel determination of the individual kinematic models for a field of heliostats with high accuracy. These parameters are determined using low-cost uncalibrated cameras attached to each heliostat, which could be replaced by a strongly directional photodiode. The method has also been successfully compared to similar methods.

The advantages of the method are the low cost and the fact that the cameras do not need calibration.

In future work, the method could be extended to also determine the target. Using techniques like bundle adjustment it seems possible to estimate their position during calibration, which would allow using more targets for calibration by using readily available natural landmarks or structures in the power plant.

4.2.3 ENEA feedback sensor

The aim of this paragraph is to describe a feedback sensor to check the right pointing of each heliostat having the following features: low cost, easiness in installation and set-up, easy interfacing with tracker control system.
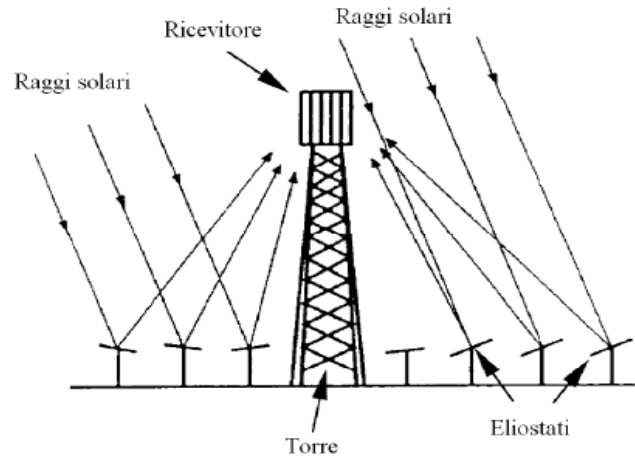

Figure 101. Scheme of a solar tower plant.

In a mirror based concentrating system it is very important that the solar tracking is as accurate as possible during the whole day: at this aim the control system has to assure that the reflected beam hits for all day the target making, if needed, the required pointing corrections. Moreover in stow conditions, the control system has to assure that the tracker goes quickly in safety position.

The most important parameter for the control system design is the acceptance angle, that is the maximum angular error in the tracker positioning that can be accepted. Normally the control systems are based on electronics: this guarantees high accuracy and reliability both in open and in closed loop. In this case, higher tracker accuracy is reached, but also system complexity and total cost is increased respect to the case of an open loop logic.

ENEA has a lot of experience in realization of heliostat control system: a low cost controller for photovoltaic concentrating plant and an optoelectronic system for the detection of tracking errors have been already developed and patented.

4.2.3.1 Feedback strategy description

The methodology for the realization of a feedback sensor for tower solar systems is based on the elaboration of the images of the receiver and of the sun acquired by a CMOS sensor installed on the tracking plane of each mirror. This solution has been already described in the US PATENT N°8651100B2, (Pfahl et al.). The component is conceptually composed (see Figure 102 and Figure 103) by an holed mask positioned above the sensor: the light emitted by the sensor and by the sun pass through the hole and hit the sensor in two separated points.
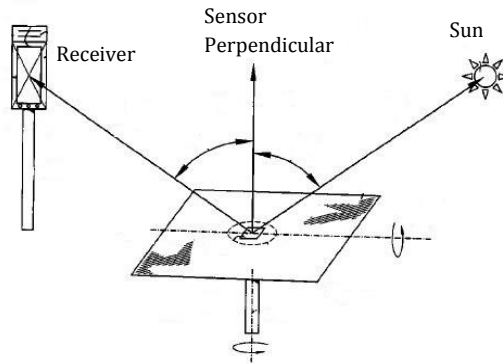
Figure 102. Conceptual scheme of the feedback sensor.

If the mirror is correctly pointed, two conditions have to be respected:

- The 3 directions of sun light, of receiver light and of the sensor perpendicular, have to lie in the same plane.
- The two angles formed by sun light direction and sensor perpendicular and by this latter and receiver light direction have to be the same.

It is easy to understand that the effects of these two conditions are respectively:

- The segment joining the target and sun images on the sensor has to pass through the sensor central point.
- The distance between the two images and the sensor center has to be the same.
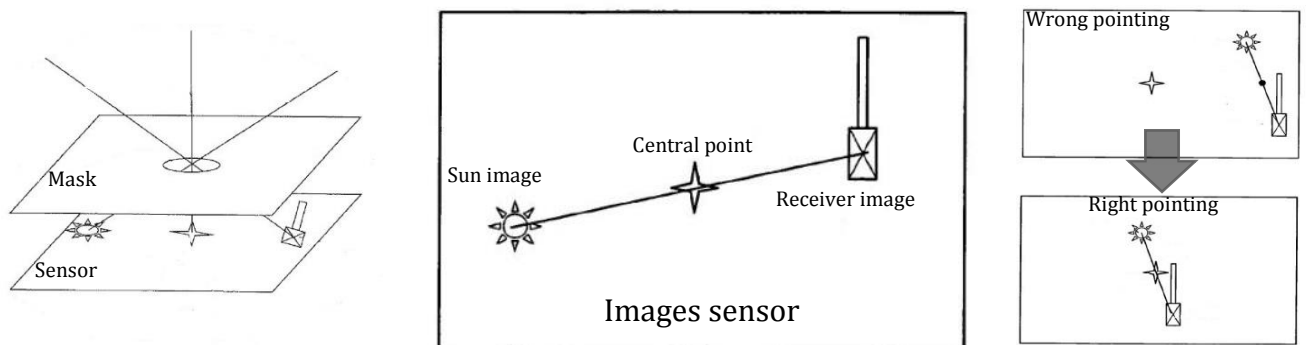
Figure 103. Working scheme of the feedback sensor.

The feedback system consists of an image sensor (e.g. a 5Mpx CMOS digital sensor) used to correctly analyse, on its surface, the two images of the sun and of the target. It is housed in a closed box able to be mounted parallel to the heliostat reflective surface. A calibrated pin hole has to be realized on the box upper surface, so that the view angle of the sensor is at least of 120°. An electronic board equipped with a commercial microcontroller is used for the elaboration of the data coming from the sensor and a RS232 interface is used for the communication of the pointing correction information to the tracker control system.
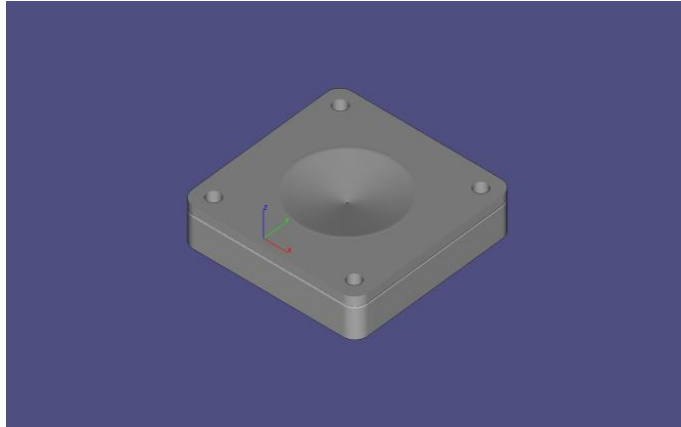
Figure 104. Feedback sensor CAD image.

The feedback system set up foresees the determination of its optical center that is the point corresponding to the intersection between the perpendicular passing through the pin hole and the sensor surface. During this operation the component is already mounted on the heliostat that is driven to direct its tracking surface perfectly perpendicular to the solar beam: in this condition the centroid of the sunlight image corresponds to the system optical center. Afterwards each tracker of the solar field is moved until the target image will hit perfectly the sensor optical center: in this condition, altitude and azimuthal coordinates of the target needed for the normal operation of the feedback, are stored.

With respect to the other control systems usable for solar towers, the described instrumentation presents the following advantages:

- Low cost.
- Easiness of operation.
- Small size.
- Easiness of set up.

Its main characteristic and advantage consists in the possibility to interface each feedback sensor only with the control logic of the tracker where it is mounted: in this way the mirror field is managed with distributed intelligence architecture. Respect to the centralized solution (with a central controller that handles hundreds or thousands of heliostats), the consequences of this choice are the reduction of the complexity of the control system and the reduction of the wires installation on the field for the communication between the master unit and the several slaves.

4.2.3.2 ENEA first prototype

The ENEA first prototype is based on a profile sensor realized from HAMAMATSU (model S9132), even if the first hypothesis was the use of a 5Mpx image sensor.

The aim of this choice is the complexity reduction of the interfacing and of the data elaboration functions, reducing, at the same time, the costs. A profile sensor is an high-performance CMOS area sensor particularly intended to acquire projection data. A projection profile in the X and Y directions has very small amounts of data compared to normal area

sensors and therefore allows high-speed position detection and moving object detection. Moreover, because it consists of a pixel matrix, it allows to detect the position of multiple light targets, as it is necessary for our application.
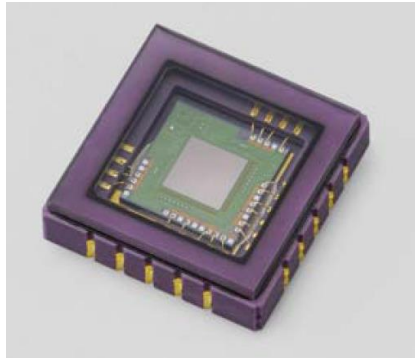

Figure 105. Profile sensor used for the realization of the prototype.

Here are reported the main sensors characteristics:

- Number of pixel: 256x256.
- Pixel pitch: 7.8μm.
- Photosensitive area: 1.9968x1.9968 mm2.
- Package material: Ceramic.
- Window material: Borosilicate glass.

From the constructive point of view, a microcontroller by STMicroelectronics model STM32F104CBT6, has been used for the interfacing with the Profile Sensor, for the consequent data elaboration and for the communication with the heliostat control logic through the RS232 interface.

A 4Mhz quartz resonator generates the clock needed both for the microcontroller and for the profile sensor working.

Two monolithic voltage regulator provide the voltage supply of 5V and 3.3V, needed for the apparatus.

A line driver converts the microcontroller output signal to the RS232 interface standard levels.

A JTAG interface allows to program the microcontroller and to make the debug, in order to test and to validate different algorithms.

An EPROM 24C02 memory is used for the permanent storage of working parameters, such as the calibration of the sensor perpendicular.

Several test points have been introduced in order to verify the hardware and software right working of the complete circuit; for this first prototype, an USB interface is available for the communications with external devices.

As you can see from the wiring diagram, the interfacing between the sensor and the microcontroller has been hardly simplified, both for cost reduction raisons and to contain the sensor dimensions. This determined a greater software complexity, without affect the system performances.
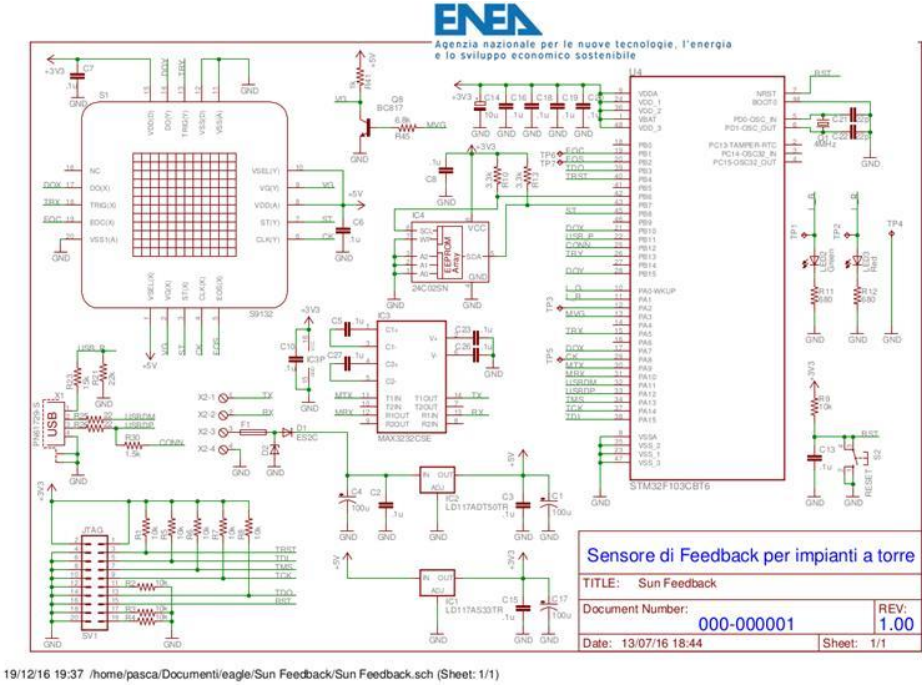
Figure 106. Wiring diagram of the Feedback sensor.

The small hole on the sensor surface has been realized attaching, using the high energy laser methodology (see https://www.newport.com/p/PH-50), the pinhole directly on the sensor, and darkening all the remaining window surface.

The pinhole is a 15μm tick circular foil made of molybdenum with a 50 μm central hole that is located at 1.1mm from the sensor active surface. Considering that the sensor dimensions are 2x2mm, the sensor field of view (FOV) is of 84,5°.

At the moment, two strategies to increase the FOV are under investigation: the integration of the pinhole at the inner surface of the sensor window and the use of a plano-convex lens at the pinhole aperture.

Actually the feedback sensor has been completely realized, and a first version of the software is used for its working. A new software release is under developing in order to improve the functions related to data elaboration and to spots light detection.

Several laboratory tests, carried out using an optical fibre lighter and an X-Y stage, revealed a sensor accuracy about of 0.05°.

Figure 107. Feedback sensor –electronic board.

Further activities regard the sensor testing on the field and the experimentation of several algorithms devoted to the elaboration of the information coming from the sensor.
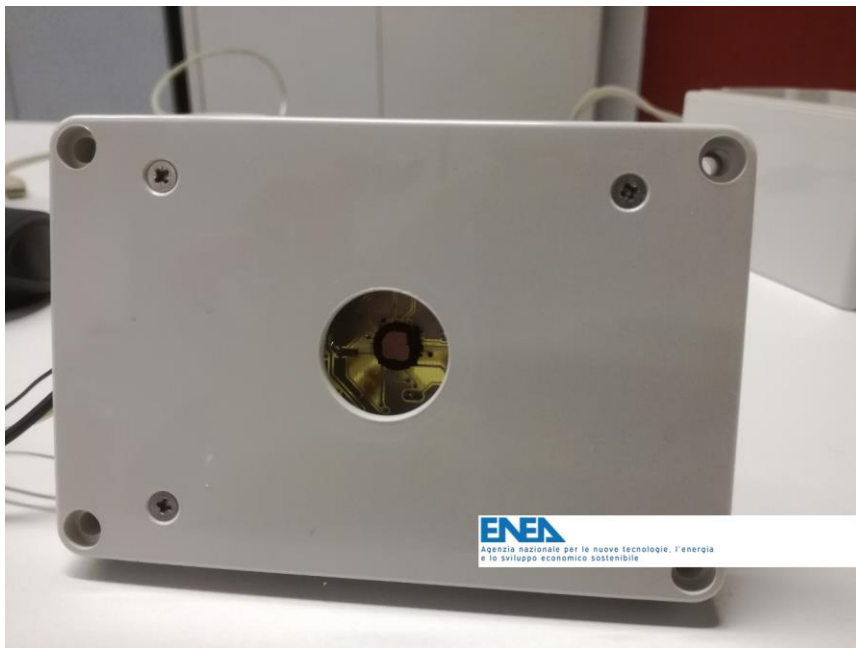

Figure 108. Feedback sensor –front view.

5 Selection and design of heliostats tracking control system

The Central Solar Field Controller is responsible for controlling the operational mode of each individual heliostat, providing aim-point off-sets to individual heliostats and periodically downloading updates to the control algorithm used to all heliostats and also downloading changes to the error matrix to individual heliostats as a result of updated calibration information. It will contain the central radio controlled clock and will from time to time ensure that all Heliostat Controller clocks are running synchronously with the central clock.

The Heliostat controller is responsible for taking the control mode instruction for the Central Solar Field Controller, and to go into that mode of operation. If it is one of the modes where it needs to aim at a particular point it would work out the position of the sun based on exact time and date and the position the actuators needed to be driven to achieve the desired aim point. Heliostat Controllers must also be able to react immediately to a "Trip" signal broadcast to all heliostats simultaneously.

Small heliostats mean much greater numbers to give the same area of reflective surface so the consequences are that it might no longer be possible to control all the heliostats from a central location; the data rate is too high. So, given that there must be a limit either in the amount and speed of computation or of the speed and data transfer rate of the communication system, then there must a point at which it is better to put the control into each heliostat so it is only necessary to instruct mode change, i.e. you don't need to tell every heliostat in the whole field where to point to every couple of seconds.

5.1 Ranking and selection of alternatives

This is where the alternative control strategies are ranked based on obvious criteria such as Pointing accuracy, the number of heliostats that can be accommodated in a single field, the speed they can be calibrated and cost, both in terms of the capital cost of the heliostat and control and the cost of installation (this is an obvious area where an autonomous heliostat is at an advantage to wired up communications and powered system).

5.1.1 Case A. Local control version (heliostats control with most desired control capabilities and autonomy)

While it may possible to have a Central Solar Field Controller calculating and communicating the 2-axis drive instructions for every heliostat in the field, it has been assumed that this is unlikely to be practical as the number of heliostats increases. This would correspond to Case A, a simplest local control with minimum control capabilities. Each heliostat would just respond to the centrally communicated instructions and moved to the position it is instructed to.

5.1.2 Case B. Central control version (heliostats control with minimum control capabilities)

Based on the argument of Section 5.1.1 it is assumed that the solar field controller (see Figure 109a) controls the overall solar field and the solar flux received by instructing each heliostat as to its mode of operation and by giving individual heliostats information on off-sets to the aim point when in operation or pre-heat mode.

5.2 Analysis of wireless/wire configuration (protocols of communications, control system architecture, layout, etc.)

Cabling costs become a more significant factor as heliostat size reduces and the number of heliostats in a field increases. Small heliostats therefore benefit more from having a local source of power (PV plus battery or super-capacitor) and of utilising wireless control. If a wired system is used then communication can be via a special communication cable that will have a high bandwidth, or, it might be possible to utilise the lower bandwidth of communication over the power cables. In practice the main cost in cabling will be in trenching and ducting and to a lesser extent the cost of larger power cables. Running thin, screened communication cables is a fairly minor cost in comparison.

As is well known wireless communication is a fast growing technology that enables networks and services to be accessed without involving cables for transmission of information. The wireless approach shows many advantages but also some disadvantages with respect to cables networks. Another advantage lies in the way wireless users can dynamically join or leave the network, create ad hoc networks for a limited time and then leave. The technological challenges involved in wireless networks are not trivial, leading to disadvantages with respect to cable networks, such as lower reliability due to interference, higher power consumption, data security threats due to the internet broadcast properties of the radio medium.

Table 12. Comparison of wired and wireless networks.

Characteristics	Wired Networks	Wireless Networks
Installation	Difficult to moderate – require cables during installation of computers, etc.	Easy installation – neat and clean
Visibility of node to node on the same network	All of the nodes on a wired network can hear other nodes	Many nodes on a wireless network cannot hear all the other nodes on the same network
Time to installation	More due to connection to each node (heliostat)	Less and cable connections can be tidy
Reliability	High	Reasonable

Speed and bandwidth	High Up to 100 mbps	Low
Transmission medium	Copper wires, Ethernet	EM waves, radiowaves or IR
Applications	LAN (Ethernet)	WLAN, WPAN, Zigbee
Channel interference	Interference is less as on wired network will not affect the other	Interference is higher due to obstacles between wireless transmitter and receiver e.g. weather conditions
Quality of Service	Better	Poor due to high value of jitter and delay in connection setup
Reliability	High	Reasonably high

A wireless network is seldom free of wires. The distribution system often includes wiring which is necessary to tie together the access points, access controllers, and servers. In most cases, the common Ethernet comprises the distribution system.

Protocols: during the last few years, many communication protocols (standards) for wireless mesh networks have been developed including Zigbee, 6LoWPAN, IEEE 802.11s, WiFi and Wireless Hart.


a)   b)
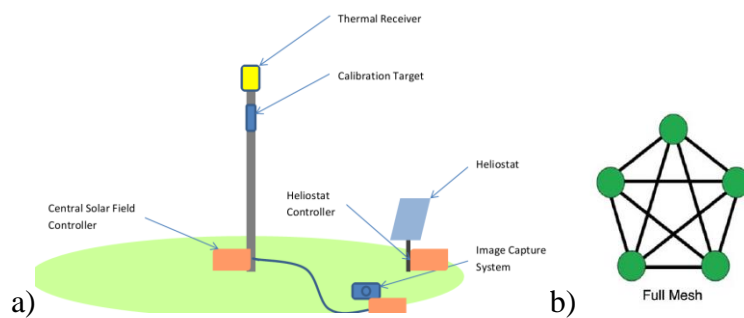
*Figure 109. a) Architecture b) Mesh topology.*
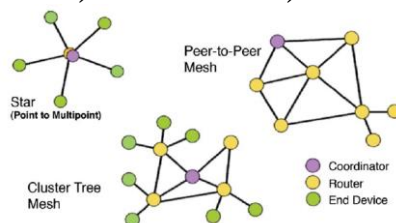
Figure 110. Cluster formation of backbone.

Topology can be understood as a map of the network, describing the layout of cables and the location of all network components.

5.2.1 Case A. Local control version (heliostats control with most desired control capabilities and autonomous)

A current heliostat design, especially if it is wireless, will feature a local control with enough processing to perform all calculations locally. If a local control system is accepted the communication between the central control and the heliostat is limited to commands like:

- Focus on point
- Move to stow/cleaning
- Etc.

These are rarely sent. For instance for Focus on Point the heliostat (on its own) will autonomously update its position to keep reflecting to the set position. In case the heliostat does not feature a real local control, it will continuously receive every 30 seconds or whatever is required for accurate operation and update its position accordingly.

5.2.2 Case B. Central control version (heliostats control with minimum control capabilities)

Some Control version must remain as it will be sometimes necessary to move group – or possibly the whole group.

A **wired network** connects devices to the Internet or other **network** using cables. The most common **wired networks** use cables connected to Ethernet ports on the **network** router on one end and to a computer or other device on the cable's opposite end.

Communications network architecture and protocols

Each heliostat in the field needs a separate address. Some form of error detection is desirable so that any corrupted messages can be ignored and potentially requests back for re-transmittal made. This can be achieved by the addition of parity checks but it is normal to use some redundant verification code added to each message that is derived by the sender and then checked by the receiver based on a common verification code algorithm.

The thesis by Malan suggests that the network protocol can be based on a proprietary system such as MODBUS. Also that a typical data packet may be 13 bytes and this needs to be transmitted to each heliostat in the field every control period, then this dictates the theoretical bandwidth. In practice the network needs to have about x10 this capacity to avoid clashes.

Recently the direction of heliostat technology has been towards smaller heliostats and therefore to larger numbers of heliostats. It follows that the density of heliostats will also increase giving a practically unique situation of dense nodes positioned over very large areas.

It is clear that to access wireless technology for Heliostats there are many challenges to be overcome but being one where the change to wireless systems promises one of the largest component of future cost reduction.

6 References

[1] C.E. Andraka, S. Sadlon, B. Myer, K. Trapeznikov and C. Liebner, "Rapid reflective facet characterization using fringe reflection techniques", ASME Journal of Solar Energy Engineering, Vol 136(1), pp 011002, 2013.

[2] S.A. Jones, D.R. Neal, J.K. Gruetzner, R.M. Houser and R.M. Edgar, "VSHOT: A tool for characterizing large, imprecise reflectors", Sandia National Laboratories Technical Report SAND96-2272, 1996.

[3] D. Kearney, "Utility-scale power tower solar systems: Performance Acceptance Test Guidelines," National Renewable Energy Laboratory Report NREL/SR-5500-5727, 2013.

[4] C.E. Kennedy and K. Terwilliger, "Optical Durability of Candidate Solar Reflectors," Journal of Solar Energy Engineering, Vol. 127, pp. 262-269, 2005.

[5] G.J. Kolb, S.A. Jones, M.W. Donnelly, D. Gorman, R. Thomas, R. Davenport, R. Lumia, "Helisotat cost reduction study" Sandia Technical Report SAND2007-3293, Albuquerque NM, 2007.

[6] A. Lewandowski and A. Gray, "Video Scanning Hartmann Optical Tester (VSHOT) Uncertainty analysis", National Renewable Energy Laboratory Technical Report NREL/CP-5500-49305, 2010.

[7] E. Lupfert and S. Ulmer, "Solar trough mirror shape specifications", Proceedings of the 2009 SolarPACES Conference, 2009.

[8] T. Marz, C. Prahl, S. Ulmer, S. Wilbert and C. Weber, "Validation of two optical measurement methods for qualification of the shape accuracy of mirror panels for concentrating solar systems", ASME Journal of Solar Energy Engineering, Vol 133(3), pp 031022, 2011.

[9] S. Meiser, "Analysis of parabolic trough concentrator mirror shape accuracy in laboratory and collector," PhD Thesis, RWTH Aachen, Germany, 2013.

[10] J.A. Peterka and R.G. Derickson, "Wind load design methods for ground-based helisotats and parabolic dish collectors", Sandia Technical Report SAND1992-7009, Albuquerque NM, 1992.

[11] K. Pottler, E. Lupfert, G.H.G. Johnston and M.R. Shortis, "Photogrammetry: A Powerful Tool for Geometric Analysis of Solar Concentrators and Their Components", ASME Journal of Solar Energy Engineering, Vol 127(1), pp 94-101, 2005.

[12] F. vonReeken, D. Nicodemo, T. Keck, G. Weinrebe, M. Balz, "Key aspects of cost effective collector and solar field design", Proceedings of the 2015 SolarPACES Conference, 2015.

[13] SFERA Project, Report 12.4, "Guidelines for Testing of CSP Components," 2013.

[14] M.R. Shortis and G.H.G. Johnston, "Photogrammetry: an available surface characterization tool for solar concentrators, Part I: Measurements of Surfaces", ASME Journal of Solar Energy Engineering, Vol 118(3), pp 146-150, 1996.

[15] M.R. Shortis and G.H.G. Johnston, "Photogrammetry: an available surface characterization tool for solar concentrators, Part II: Assessment of the Surfaces", ASME Journal of Solar Energy Engineering, Vol 119(4), pp 286-290, 1997.

[16] SolarPACES Guidelines, "Parameters and method to evaluate the solar reflectance properties of reflector materials for concentrating solar power technology", v.2.5, 2013.

[17] S. Ulmer, B. Heinz, K. Pottler and E. Lupfert, "Slope error measurements of parabolic troughs using the reflected image of the absorber tube", ASME Journal of Solar Energy Engineering, Vol 131(1), pp 011014, 2009.

[18] S. Ulmer, T. Marz, C. Prahl, W. Reinalter, and B. Belhomme. "Automated high resolution measurement of heliostat slope errors" Solar Energy, Vol. 85(4), pp. 681-687, 2011.

[19] B.A. Harper, J.D. Kepert, J.D. Ginger, "Guidelines for converting between various wind averaging periods in tropical cyclone conditions", World Meteorological Organization, 2008.

[20] A.B. Zavoico, "Solar Power Tower, Design Basis Document", Sandia Technical Report SAND2001-2100, Albuquerque NM, 2001.

[21] R. Monterreal, A. Neumann, "Advanced Flux Measurement System for Solar Tower Plants", Proceedings of the Seventh International Symposium on Solar Thermal Concentrating Technologies (1994).

[22] R. Monterreal, "A new computer code for solar concentrating optics simulation", Proceedings of the 9th SolarPACES International Symposium on Solar Thermal Concentrating, J. Phys. IV France, 9 (1999), pp. 77–82.

[23] Burisch, M., Sanchez, M., Olarra, A., & Villasante, C. (2016, May). Heliostat calibration using attached cameras and artificial targets. In V. Rajpaul, & C. Richter (Eds.), AIP Conference Proceedings (Vol. 1734, No. 1, p. 130005). AIP Publishing.

[24] Wendelin, T., G. Jorgensen, and R. Wood, (1991). "SHOT: A method for characterizing the surface figure and optical performance of point focus solar concentrators." Proceedings 13th Annual ASME Solar Energy Conference, Reno, Nevada.

[25] Wendelin, Tim, Ken May, and Randy Gee. "Video scanning hartmann optical testing of state-of-the-art parabolic trough concentrators." ASME 2006 International Solar Energy Conference. American Society of Mechanical Engineers, 2006.

[26] Gray, A., A. Lewandowski, and T. Wendelin. "Visual Scanning Hartmann Optical Tester (VSHOT) Uncertainty Analysis." Contract 303 (2010): 275-3000.

[27] Nikon MV330 / 350 Laser Radar http://www.nikonmetrology.com/Products/Large-Volume-Applications/Laser-Radar/MV330-MV350-Laser-Radar/(specifications) (December 2014).

[28] Scott A. Jones, James K. Gruetzner, Richard M. Houser, Robert M. Edgar: "VSHOT Measurement uncertainty and sensitivity study" (1997).

[29] Baltsavias, E. P. (1999). A comparison between photogrammetry and laser scanning. ISPRS Journal of photogrammetry and Remote Sensing, 54(2), 83-94.

[30]   *Fraser, C. S., & Brown, D. C. (1986). Industrial photogrammetry: New developments and recent applications. The Photogrammetric Record, 12(68), 197-217.*

[31]   *Beyer, H. A. (1992, June). Accurate calibration of CCD-cameras. In Computer Vision and Pattern Recognition, 1992. Proceedings CVPR'92., 1992 IEEE Computer Society Conference on (pp. 96-101). IEEE.*

[32]   *Brown, J., & Dold, J. (1995). V-STARS-A system for digital industrial photogrammetry. Optical 3-D Measurement Techniques III, 12-21.*

[33]   *Fraser, C. S., Shortis, M. R., & Ganci, G. (1995, September). Multisensor system self-calibration. In Photonics East'95 (pp. 2-18). International Society for Optics and Photonics.*

[34]   *Ganci, G., & Shortis, M. R. (1995). The use of digital photogrammetry for large scale metrology. In Proceedings, 36th Australian Surveyors Congress (pp. 247-261).*

[35]   *Shortis, M. R., & Fraser, C. S. (1991). Current trends in close-range optical 3D measurement for industrial and engineering applications. Survey Review, 31(242), 188-200.*

[36]   *Gustafson and Handley, 1992. A Video-Based Industrial Measurement System. International Archives of Photogrammetry and Remote. Sensing, Volume XXIX, Part B5, Commission V, pp. 501-506.*

[37]   *Ganci, G., & Shortis, M. R. (1996). A comparison of the utility and efficiency of digital photogrammetry and industrial theodolite systems. International Archives of Photogrammetry and Remote Sensing, 31, 182-187.*

[38]   *Fraser, C. S., Woods, A., & Brizzi, D. (2005). Hyper redundancy for accuracy enhancement in automated close range photogrammetry. The Photogrammetric Record, 20(111), 205-217.*

[39]   *Rieke-Zapp, D. H., & Nearing, M. A. (2005). Digital close range photogrammetry for measurement of soil erosion. The Photogrammetric Record, 20(109), 69-87.*

[40]   *Broers, H., & Jansing, N. (2007). How precise is navigation for minimally invasive surgery?. International orthopaedics, 31(1), 39-42.*

[41]   *Luhmann, T. (2004). A historical review on panorama photogrammetry. International Archives of the Photogrammetry, Remote Sensing and Spatial Information Sciences, 34(5/W16), 8.*

[42]   *Luhmann, T., & Robson, S. (2008). Industrial photogrammetry. In Advances in Photogrammetry, Remote Sensing and Spatial Information Sciences, ISPRS Congress Book, Taylor & Francis Group, London, ISBN (pp. 978-0).*

[43]   *Luhmann, T., Robson, S., Kyle, S. A., & Harley, I. A. (2006). Close range photogrammetry: principles, techniques and applications. Whittles.*

[44]   *Shortis, M. R., & Harvey, E. S. (1998). Design and calibration of an underwater stereo-video system for the monitoring of marine fauna populations. International Archives of Photogrammetry and Remote Sensing, 32, 792-799.*

[45]   Bösemann, W., & Sinnreich, K. (1994). Vollautomatische Punktsuche und Punkterkennung im Digitalen Bild. Publikationen der Deutschen Gesellschaft für Photogrammetrie und Fernerkundung, 2, 215-219.

[46]   Conrady, A. E. (1919). Lens-systems, Decentered. Monthly notices of the royal astronomical society, 79, 384-390.

[47]   Brown, D. (1966). Decentering Distortion of lenses, D. Brown Associates. Inc, Eau Gallie, Florida, Tech. Rep.

[48]   Hartley, R., & Kang, S. B. (2007). Parameter-free radial distortion correction with center of distortion estimation. IEEE Transactions on Pattern Analysis and Machine Intelligence, 29(8), 1309-1321.

[49]   Duane, C. B. (1971). Close-range camera calibration. Photogramm. Eng, 37(8), 855-866.

[50]   Faig, W. (1975). Calibration of close-range photogrammetric systems: Mathematical formulation. Photogrammetric engineering and remote sensing, 41(12).

[51]   Weng, J., Cohen, P., & Herniou, M. (1992). Camera calibration with distortion models and accuracy evaluation. IEEE Transactions on pattern analysis and machine intelligence, 14(10), 965-980.

[52]   Wei, G. Q., & Ma, S. D. (1993, May). A complete two-plane camera calibration method and experimental comparisons. In Computer Vision, 1993. Proceedings., Fourth International Conference on (pp. 439-446). IEEE.

[53]   Zhang, Z. (2000). A flexible new technique for camera calibration. IEEE Transactions on pattern analysis and machine intelligence, 22(11), 1330-1334.

[54]   Zhang, Z. (2004). Camera calibration with one-dimensional objects. IEEE transactions on pattern analysis and machine intelligence, 26(7), 892-899.

[55]   Stein, G. P. (1995, June). Accurate internal camera calibration using rotation, with analysis of sources of error. In Computer Vision, 1995. Proceedings., Fifth International Conference on (pp. 230-236). IEEE.

[56]   Hartley, R. I. (1994, May). Self-calibration from multiple views with a rotating camera. In European Conference on Computer Vision (pp. 471-478). Springer Berlin Heidelberg.

[57]   Becker, S. C., & Bove Jr, V. M. (1995, April). Semiautomatic 3D-model extraction from uncalibrated 2D-camera views. In IS&T/SPIE's Symposium on Electronic Imaging: Science & Technology (pp. 447-461). International Society for Optics and Photonics.

[58]   Maas, H. G. (1999). Image sequence based automatic multi-camera system calibration techniques. ISPRS Journal of Photogrammetry and Remote Sensing, 54(5), 352-359.

[59]   Tecklenburg, W., Luhmann, T., & Hastedt, H. (2001). Camera modelling with image-variant parameters and finite elements. Optical, 328-335.

[60]   VDI/VDE 2634: Optical 3D measuring systems. VDI/VDE guide line, part 1-3, Beuth, Berlin.

[61]   Rieke-Zapp, D. H., & Nearing, M. A. (2005). Digital close range photogrammetry for measurement of soil erosion. The Photogrammetric Record, 20(109), 69-87.

[62]   Luhmann, T., Bethmann, F., Herd, B., & Ohm, J. EXPERIENCES WITH 3D REFERENCE BODIES FOR QUALITY ASSESMENT OF FREEFORM SURFACE MEASUREMENTS. International Archives of Photogrammetry, Remote Sensing and Spatial Information Sciences, 38(Part 5), 405-410.

[63]   García-Cortés, S., Bello-García, A., & Ordóñez, C. (2012). Estimating intercept factor of a parabolic solar trough collector with new supporting structure using off-the-shelf photogrammetric equipment. Applied energy, 92, 815-821.

[64]   Fernández-Reche, J., & Valenzuela, L. (2012). Geometrical assessment of solar concentrators using close-range photogrammetry. Energy Procedia, 30, 84-90.

[65]   Bian, X., Su, X., Chen, W., & Zhang, Q. (2012). 3D coordinate measurement based on inverse photogrammetry and fringe analysis. Optik-International Journal for Light and Electron Optics, 123(9), 841-845.

[66]   Bösemann, W. (2005). Advances in photogrammetric measurement solutions.Computers in Industry, 56(8), 886-893.

[67]   Brown, J. (1998). V-STARS/SA cceptance T est R esults. In Boeing Large Scale Optical Metrology Seminar.

[68]   Brown, J. D., Ganci, G., & Handley, H. B. (2006). U.S. Patent No. 6,990,215. Washington, DC: U.S. Patent and Trademark Office.

[69]   Cuypers, W., Van Gestel, N., Voet, A., Kruth, J. P., Mingneau, J., & Bleys, P. (2009). Optical measurement techniques for mobile and large-scale dimensional metrology. Optics and Lasers in Engineering, 47(3), 292-300.

[70]   Delara, R., Mitishita, E., & Habib, A. (2004, July). Bundle adjustment of images from non-metric CCD camera using LIDAR data as control points. InInternational Archives of XXth ISPRS Congress (pp. 13-19).

[71]   Esmaeili, F., Varshosaz, M., & Ebadi, H. (2013). Displacement measurement of the soil nail walls by using close range photogrammetry and introduction of CPDA method. Measurement, 46(9), 3449-3459.

[72]   Farnood Ahmadi, F., & Layegh, N. F. (2014). Integration of close range photogrammetry and expert system capabilities in order to design and implement optical image based measurement systems for intelligent diagnosing disease. Measurement, 51, 9-17.

[73]   Fraser, C. S., & Edmundson, K. L. (2000). Design and implementation of a computational processing system for off-line digital close-range photogrammetry. ISPRS Journal of Photogrammetry and Remote Sensing,55(2), 94-104.

[74]   Fraštia, M. (2005). Possibilities of using inexpensive digital cameras in applications of close-range photogrammetry. Slovak Journal of Civil Engineering, 8(2), 20-28.

[75]   Ganci, G., & Clement, R. (2000). The use of self-identifying targeting for feature based measurement. Coordinate Measuring System Committee, July.

[76]   Ganci, G., & Handley, H. (1998). Automation in videogrammetry. International Archives of Photogrammetry and Remote Sensing, 32, 53-58.

[77]   Ganci, G., & Shortis, M. R. (1996). A comparison of the utility and efficiency of digital photogrammetry and industrial theodolite systems. International Archives of Photogrammetry and Remote Sensing, 31, 182-187.

[78]   Gerbino, S., Martorelli, M., Renno, F., & Speranza, D. (2004). CHEAP PHOTOGRAMMETRY VERSUS EXPENSIVE REVERSE ENGINEERING TECHINQUES IN 3D MODEL ACQUISITION AND SHAPE RECONSTRUCTION. In DS 32: Proceedings of DESIGN 2004, the 8th International Design Conference, Dubrovnik, Croatia.

[79]   Jiandong, Z., Liyan, Z., & Xiaoyu, D. (2009). Accurate 3D target positioning in close range photogrammetry with implicit image correction. Chinese Journal of Aeronautics, 22(6), 649-657.

[80]   Khalil, A. M. (2011). Two-dimensional displacement measurement using static close range photogrammetry and a single fixed camera. Alexandria Engineering Journal, 50(3), 219-227.

[81]   Koch, M., & Kaehler, M. (2009, March). Combining 3D laser-Scanning and close-range Photogrammetry-An approach to Exploit the Strength of Both methods. In Making History Interactive. Computer Applications and Quantitative Methods in Archeology Conference (pp. 22-26).

[82]   Koelman, H. J. (2010). Application of a photogrammetry-based system to measure and re-engineer ship hulls and ship parts: An industrial practices-based report. Computer-Aided Design, 42(8), 731-743.

[83]   Lee, H., & Rhee, H. (2013). 3-D measurement of structural vibration using digital close-range photogrammetry. Sensors and Actuators A: Physical, 196, 63-69.

[84]   Luhmann, T. (2010). Close range photogrammetry for industrial applications.ISPRS Journal of Photogrammetry and Remote Sensing, 65(6), 558-569.

[85]   März, T., Prahl, C., Ulmer, S., Wilbert, S., & Weber, C. (2011). Validation of two optical measurement methods for the qualification of the shape accuracy of mirror panels for concentrating solar systems. Journal of Solar Energy Engineering, 133(3), 031022.

[86]   McLauchlan, P. F., & Jaenicke, A. (2002). Image mosaicing using sequential bundle adjustment. Image and Vision Computing, 20(9), 751-759.

[87]   Ricolfe-Viala, C., & Sánchez-Salmerón, A. J. (2010). Robust metric calibration of non-linear camera lens distortion. Pattern Recognition, 43(4), 1688-1699.

[88]   Pottler, K., Lüpfert, E., Johnston, G. H., & Shortis, M. R. (2004, January). Photogrammetry: A powerful tool for geometric analysis of solar concentrators and their components. In ASME 2004 International Solar Energy Conference(pp. 719-726). American Society of Mechanical Engineers.

[89]   Trier, W., Drews, P., & Reibiger, J. (1997). Strategies for using robots in high-precision 3D measurement. Mechatronics, 7(4), 385-411.

[90]   Triggs, B., McLauchlan, P. F., Hartley, R. I., & Fitzgibbon, A. W. (2000). Bundle adjustment—a modern synthesis. In Vision algorithms: theory and practice (pp. 298-372). Springer Berlin Heidelberg.

[91]   Wang, X., & Clarke, T. A. (1998). Separate adjustment of close range photogrammetric measurements (Doctoral dissertation, City University).

[92]   Wang, W. T., & Liu, H. B. (2013). Research on a Digital Close-Range Photogrammetric Bridge Deflection Measurement System. Applied Mechanics and Materials, 392, 734-737.

[93]   Weckenmann, A., Jiang, X., Sommer, K. D., Neuschaefer-Rube, U., Seewig, J., Shaw, L., & Estler, T. (2009). Multisensor data fusion in dimensional metrology. CIRP Annals-Manufacturing Technology, 58(2), 701-721.

[94]   Xiao, Z., Jin, L., Yu, D., & Tang, Z. (2010). A cross-target-based accurate calibration method of binocular stereo systems with large-scale field-of-view.Measurement, 43(6), 747-754.

[95]   Xiao, Z., Liang, J., Yu, D., & Asundi, A. (2011). Large field-of-view deformation measurement for transmission tower based on close-range photogrammetry.Measurement, 44(9), 1705-1712.

[96]   Yianmin, W. (1993). A Rigorous Photogrammetric Adjustment Algorithm Based on Co-angularity. Condition. INTERNATIONAL ARCHIVES OF PHOTOGRAMMETRY AND REMOTE SENSING, 29, 195-195.

[97]   Geckeler R. D., A. Just, M. Krause. 2008. Angle Metrology for Highly Accurate Topography Measurement: New Developments & Applications. Dimensional metrology club, AIST/NMIJ Tokyo.

[98]   Hume , K . J ., 1965, Metrology with Autocollimators , Hilger and Watts , London.

[99]   Evans, C., Estler, T., Hocken, R. 1996. Self-Calibration: Reversal, Redundancy, Error Separation, and "Absolute Testing", CIRP Annals – Manufacturing technology, Volume 45(Issue 2), pages 617–634.

[100]   CSP Services. Deflectometric measurement system QDEC. http://www.cspservices.eu/index.php?hp=35

[101]   [Finch, N.S., Andraka, C.E., 2011. Uncertainty analysis and characterization of the SOFAST mirror facet characterization system. In Proceedings of the ASME 2011 5th International Conference on Energy Sustainability. Washington DC.

[102]   http://www.nrel.gov/csp/solarpaces/project_detail.cfm/projectID=40

[103]   http://www.nrel.gov/csp/solarpaces/project_detail.cfm/projectID=60

[104]   http://www.nrel.gov/csp/solarpaces/project_detail.cfm/projectID=62

[105]   Procedimiento para la calibración de autocolimadores. 2004. CEM.

[106]   *Evaluación de datos de medición. Guía para la Expresión de la Incertidumbre de Medida. Edición digital. NIPO: 706-10-001-0. CEM.*

[107]   *Tarantola, A. 2005. Inverse Problem Theory. SIAM.*

[108]   *Olarra, A., Kortaberria, G., Rodriguez, E., Gomez-Acedo E., & Villasante, C. "Fast, compact and precise mirror facet measurement based on autocollimation principle", Energy Procedia 12/2014; 49(2014):2162–2169.*

[109]   *Olarra, A., Villasante, C., Kortaberria, G., Gomez-Acedo, E., & Rodriguez, E. (Dec. 2013) "Celda para la verificación de espejos en línea de fabricación", Journal, e-medida Revista Española de Metrología, Nº 5 (December 2013).*

[110]   *Sebastian Höffer, Michael Heizmann " Deflectometry for the inspection of specular surfaces " (2011).*

[111]   *.Mitsuo Takeda, Hideki Ina, Seij Kabayashi " Fourier Transform method of fringe pattern analysis for computer-based topography and interferometry " (1981).*

[112]   *Charles E. Andraka, Julius Yellowhair " AIMFAST: An alignment tool based on fringe reflection methods applied to dish concentrators " (2011).*

[113]   *Charles E. Andraka, Scott Sadlon " Rapid reflective facet characterization using fringe reflection technique " (2014).*

[114]   *Nolan S. Finch Charles E. Andraka " Unscertainty Analysis and Characterization of the SOFAST mirror facet characterization system " (2014).*

[115]   *Christoph Prahl, Badrudin Stanicki " Airborne shape measurement of parabolic trough collector fields " (2012).*

[116]   *Steffen Ulmer, Boris Heinz " Slope error measurements of parabolic troughs using the reflected image of the absorbed tube " (2009).*

[117]   *Steffen Ulmer, Tobias März " Automated high resolution measurement of heliostat slope errors " (2011).*

[118]   *Richard B. Diver, Timothy A. Moss "Practical Field Alignment of Parabolic Trough Solar Concentrators" (2007).*

[119]   *Richard B. Diver, "Alignment method for parabolic trough solar concentrators" [p]. US7667833 B1 (23 Feb, 2010).*

[120]   *TOPHAT for the alignment and focus of heliostat mirror facets. Sandia National Laboratories (2010).*

[121]   *Test results and status of the TOP alignment system for parabolic trough solar collectors (2010).*

[122]   *A. Kribus et al, "Closed loop control of heliostats", Energy 29 (2004) 905-913*

[123]   *Kenneth W. Stone, "Automatic Heliostat Track Alignment Method" (Patent US 4,564,275) (1986)*

[124]   *Litwin et al., "Feedback Control Method for a Heliostat" (Patent US 7,207,327 B2) (2007)*

[125] *Hickerson et al., "Heliostat With Integrated Image-based Tracking Controller" (Patent US 7,906,750 B2) (2011)*

[126] *Convery, "System and Method for Aligning Heliostats of a Solar Power Tower" (Patent US 8,344,305 B2) (2013)*

[127] *Fitch et al., "Heliostat Control Scheme Using Cameras" (Patent US 2011/0120448 A1) (2011)*

[128] *RAUSCHER: Prosilica GC750 Solar Power Plant uses GigE Cameras for Mirror Alignment*

[129] *Zavodny et al., "Camera-Based Heliostat Calibration With Artificial Light Sources" (Patent US 7,994,459 B2) (2011)*

[130] *Reznik et al. "Calibration and Tracking Control of Heliostats in a Central Tower Receiver Solar Power Plant" (Patent US 8,104,893 B2) (2012)*

[131] *Pfahl et al. "Method for Controlling the Alignment of a Heliostat with Respect to a Receiver, Heliostat Device and Solar Power Plant" (Patent US 8,651,100 B2) (2014)*

[132] *Schwarzbach et al. "Heliostat Calibration" (Patent US 2010/0139644 A1) (2010)*

[133] *Klimek, Jasmin; Sauerborn, Markus; Hoffschmidt, Bernhard; Sieger, Stefan; Biegel, Gregor; Essen, Helmut; Göttsche, Joachim; Hilger, Patrick (2012): Radar Technology For Heliostat Position Control. Solar Paces Conference 2012, 11.-14. Sept. 2012, Marrakech, Marokko.*

[134] *Flesch, Robert; Ahlbrink, Nils; Pitz-Paal, Robert; Belhomme, Boris (2012): Automatic determination of heliostat orientation using an auxiliary mirror. Solarpaces 2012, 11.-14. September 2012, Marrakesch, Marokko.*

[135] *F.Hénault, C.Royère, J. Optics vol.20, n°5 (1989).*

[136] *F.Hénault, C.Caliot, Installation Concentratrice de Rayonnement Cosmique Équipée 'un Système de Contrôle de Surface Optique Réfléchissante, (patent accepted 2015).*

[137] *R.Ragazzoni, J. of Modern Optics 13 n°2, pp.289-293 (1996).*

[138] *M.Born, E.Wolf, Principles of Optics, chap 5.*

[139] *M.Burisch, L.Gomez, D.Olasolo, C.Villasante, "Heliostat kinematic system calibration using uncalibrated cameras" SOLARPACES 2016.*

[140] *K.W. Stone, "Automatic heliostat track alignment method" U.S. Patent No. 4,564,275, (14 January 1986).*

[141] *M. Berenguel et al., "An artificial vision-based control system for automatic heliostat positioning offset correction in a central receiver solar power plant," in Solar Energy 76.5 (2004), pp. 563-575.*

[142] *M. Zavodny et al., "Tower-based CSP Artificial Light Calibration System," in Energy Procedia 69 (2015), pp. 1488-1497.*

[143] *A. Kribus et al., "Closed loop control of heliostats," in Energy 29.5 (2004), pp. 905-913.*

[144]   *M. Burisch et al., "Heliostat calibration using attached cameras and artificial targets," in AIP Conference Proceedings, 1734, 130005 (2016).*

[145]   *K. Hickerson and D. Reznik, "Heliostat with integrated image-based tracking controller" U.S. Patent No. 7,906,750. (15 March 2011).*

[146]   *M. Schaub, et al., Molded Optics: Design and Manufacture, (CRC press 2011).*

[147]   *R. Gonzalez and R. Woods, Digital Image Processing (3rd Edition), (Prentice-Hall, Inc., 2006).*

[148]   *C. Broyden, "The convergence of a class of double-rank minimization algorithms 1. general considerations," in IMA Journal of Applied Mathematics 6.1 (1970), pp. 76-90.*

[149]   *B. Triggs, et al., "Bundle adjustment—a modern synthesis," Vision algorithms: theory and practice. (Springer Berlin Heidelberg, 1999).*

[150]   *S. Garrido-Jurado, et al., "Automatic generation and detection of highly reliable fiducial markers under occlusion," Pattern Recognition 47.6 (2014), pp. 2280-2292.*

[151]   *K J Malan, "A Heliostat Field Control System", Dissertation presented for the degree of Master of Engineering in the Faculty of Engineering at Stellenbosch University.*